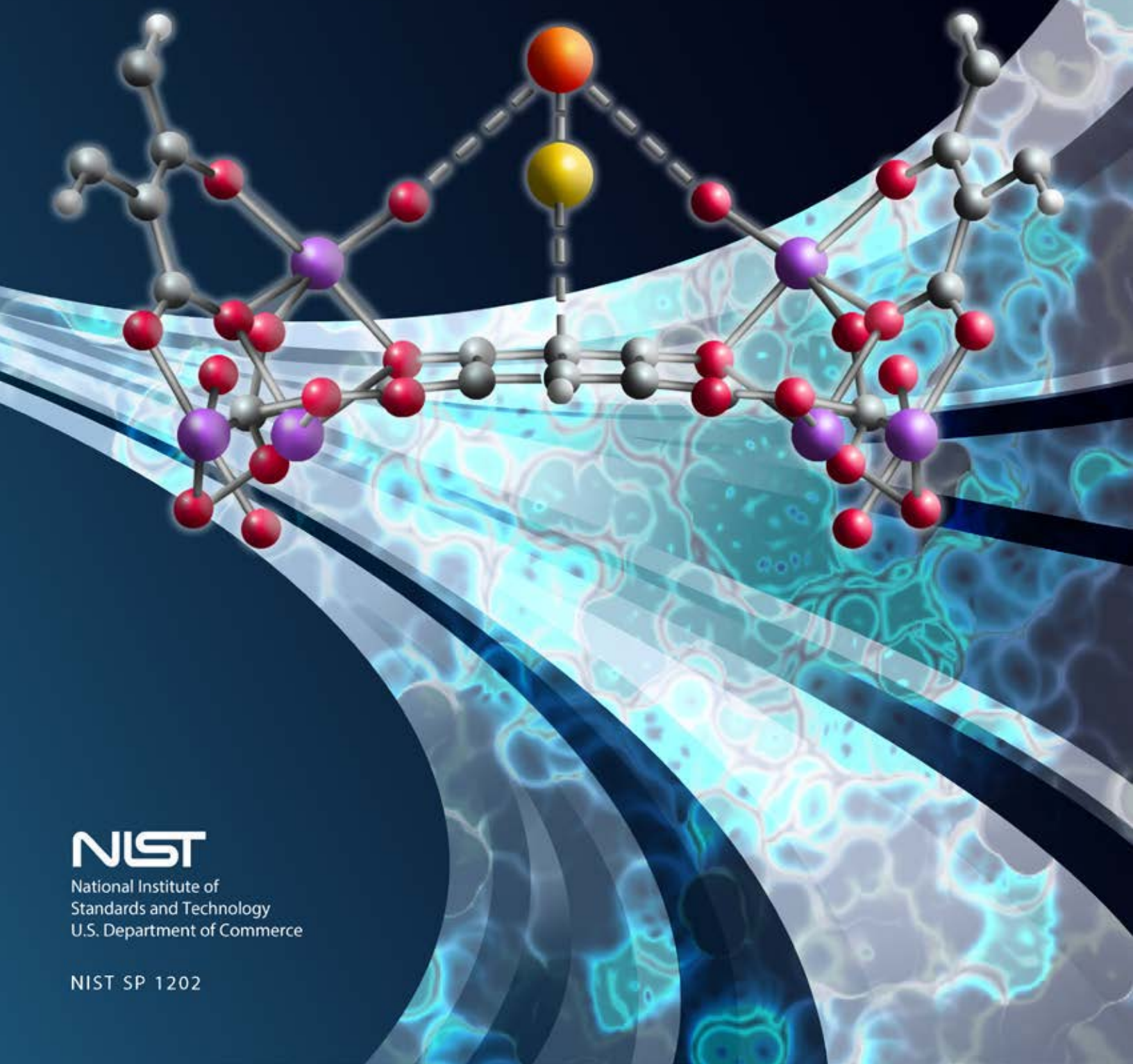


NIST CENTER FOR NEUTRON RESEARCH

2015

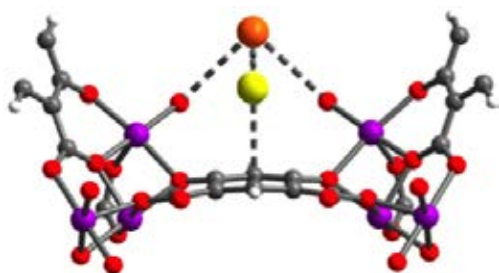
ACCOMPLISHMENTS *and* OPPORTUNITIES



NIST

National Institute of
Standards and Technology
U.S. Department of Commerce

NIST SP 1202



ON THE COVER

Metal-organic frameworks (MOFs) are suited for potential use in separation and storage of gases for fuel and industrial applications. Presented here is a partial crystal structure of a new family of MOFs with potentially improved separation and at lower cost. Details of its properties are described in the highlight article by Hudson *et al.* on p.18.

2015 NIST Center for Neutron Research ACCOMPLISHMENTS *and* OPPORTUNITIES

NIST Special Publication 1202

Robert M. Dimeo, Director

Steven R. Kline, Editor

December 2015

U.S. Department of Commerce

Penny Pritzker, Secretary

National Institute of Standards and Technology

*Willie May, Under Secretary of Commerce
for Standards and Technology and Director*



DISCLAIMER

Certain commercial entities, equipment, or materials may be identified in this document in order to describe an experimental procedure or concept adequately. Such identification is not intended to imply recommendation or endorsement by the National Institute of Standards and Technology, nor is it intended to imply that the entities, materials, or equipment are necessarily the best available for the purpose. Error bars in figures represent one standard deviation unless otherwise stated.

National Institute of Standards and Technology Special
Publication 1202
Natl. Inst. Stand. Technol. Spec. Publ. 1202, 88 pages
(December 2015)
CODEN: NSPUE2

This publication is available free of charge from:
<http://dx.doi.org/10.6028/NIST.SP.1202>

Table of Contents

ii FOREWORD

1 THE NIST CENTER FOR NEUTRON RESEARCH

2 NIST CENTER FOR NEUTRON RESEARCH INSTRUMENTS

4 NCNR IMAGES 2015

HIGHLIGHTS

BIOLOGY

- 6 Probing the structure of CENP-A derived nucleosomes using small-angle neutron scattering with contrast variation, K. Gupta, *et al.* (CHRNS)
- 8 Targeting bacteria within the mammalian cell: endolysin PlyC entry point revealed, M. Barros, *et al.*
- 10 Structural interactions of a voltage sensor toxin with lipid membranes, M. Mihailescu, *et al.*

CHEMICAL PHYSICS

- 12 Molecular understanding of high CO₂ adsorption capacity in chabazite zeolites, M. R. Hudson, *et al.*
- 14 Predicting long-time material behavior with neutrons, M. T. Cicerone, *et al.* (CHRNS)
- 16 Exploring new mixed-valence manganese oxides with neutron diffraction, A. M. Larson, *et al.*
- 18 New metal–organic framework exhibiting increased charge density and enhanced H₂ binding, M. R. Hudson, *et al.*
- 20 Structural behavior, dynamics, and superionic conduction in Na₂B₁₀H₁₀, T. J. Udovic, *et al.* (CHRNS)

CONDENSED MATTER

- 22 Magnetic scattering and vortex lattice in an iron-based ferromagnetic superconductor, J. W. Lynn, *et al.* (CHRNS)
- 24 Static and dynamic short-range order in a frustrated magnet with exchange disorder, K. A. Ross, *et al.* (CHRNS)
- 26 Electric field control of interfacial ferromagnetism in oxide heterostructures, A. J. Grutter, *et al.*
- 28 A tale of two spin-ladders in SrHo₂O₄, J.-J. Wen, *et al.* (CHRNS)
- 30 Magnetism and superconductivity in non-centrosymmetric topological RPdBi half-Heusler semimetals, Y. Nakajima, *et al.*

ENGINEERING PHYSICS

- 32 Stresses in aluminum sheet joined by the flow drill screwing process, T. Gnäupel-Herold, *et al.*

NEUTRON PHYSICS

- 34 Twisting neutron waves, D. A. Pushin, *et al.*

GEOLOGY

- 36 Combining SANS and USANS to characterize porosity evolution during hydrothermal alteration of mantle rocks, B. M. Tutolo, *et al.* (CHRNS)
- 38 Foamy porosity in gas shale, H. E. King, Jr., *et al.* (CHRNS)

SOFT MATTER

- 40 A tight situation: polymer arrest in carbon nanotube networks, R. Ashkar, *et al.* (CHRNS)
- 42 Architectural paints: from hierarchical structure to rheology, A. K. Van Dyk, *et al.* (CHRNS, nSoft)
- 44 Enhanced vertical ordering of block copolymer films by tuning temperature and molecular mass, A. Modi, *et al.*

ADVANCES IN MEASUREMENT

- 46 Wide-angle neutron collection using a defocusing Rowland geometry, L. Harriger, *et al.*
- 47 Measurement and modeling of polarized specular neutron reflectivity in large magnetic fields, B. B. Maranville, *et al.*
- 48 A far-ultraviolet neutron observatory, M. A. Coplan, *et al.*
- 49 Extensional-flow SANS of wormlike micelles, R. McAllister, *et al.* (nSoft)
- 50 Design and installation of a new instrument for prompt gamma-ray activation analysis, R. L. Paul, *et al.*

51 NEUTRON SOURCE OPERATIONS

52 FACILITY DEVELOPMENT

55 SERVING THE SCIENCE AND TECHNOLOGY COMMUNITY

58 THE CENTER FOR HIGH RESOLUTION NEUTRON SCATTERING (CHRNS)

61 2015 AWARDS

63 PUBLICATIONS: AUGUST 1, 2014 TO JULY 31, 2015

82 INSTRUMENTS AND CONTACTS

83 NIST CENTER FOR NEUTRON RESEARCH CONTACTS

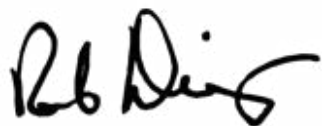
Foreword

Once again it is a pleasure to present to you this year's Accomplishments and Opportunities for the NIST Center for Neutron Research. It was another excellent year for facility operations: The reactor operated for 198 days with 98 % reliability. Both cold sources operated with nearly 100 % reliability.

We continued with a number of major developments in neutron instrumentation this year in response to the needs of the user community. The Cold Neutron Imaging (CNI) instrument was built on the end position of NG-6 and commissioning began on August 25th. You can see the inaugural radiograph of an important NIST artifact on page 53 of this report. The vSANS instrument's pre-sample optics were installed on NG-3 beamline and site preparation took place in the north end of the guide hall in anticipation of the arrival of the large vacuum vessel in 2016. Detailed design continued for the CANDoR white beam reflectometer and tests of the prototype energy dispersive detector were successful. In fact the detector development team far exceeded expectations when the new CANDoR detectors achieved 95 % of the detection efficiency of a ³He gas tube (the gold standard for neutron detection). A multi-year upgrade to the BT-8 engineering diffractometer continued with development of enhancements that will improve throughput as well as adding new sample loading capabilities. A robust program of reactor reliability and facility improvements continued this year, including the installation of the new cold source refrigerator. You can read more details about these improvements in the section on facility developments in this report.

In addition to these important facility developments, the Center for High Resolution Neutron Scattering (CHRNS) partnership with the National Science Foundation was renewed for another five years. This important interagency partnership provides robust user support for five neutron scattering instruments (currently MACS, USANS, NG-B 30m SANS, HFBS, and NSE), it is responsible for a significant fraction of the NCNR's scientific productivity, and has provided training for hundreds of scientists on neutron scattering techniques. With the renewal of this partnership, we can look forward to another five years of producing high-quality science on the CHRNS instruments and educating new scientists.

As always, the reason for the NCNR is to provide the scientific community with the best tools to perform research using neutrons. Over the last year the community produced an outstanding body of research from measurements performed here. I am excited to share with you a selection of these highlights from our users (including Summer Undergraduate Research Fellow, Koty McAllister). I hope that you enjoy reading through this report as much as I did. I believe that it gives you a taste of the exciting developments here at the NCNR over the last year.



The NIST Center for Neutron Research

Neutrons provide a uniquely effective probe of the structure and dynamics of materials ranging from water moving near the surface of proteins to magnetic domains in memory storage materials.

The properties of neutrons (outlined below) can be exploited using a variety of measurement techniques to provide information not otherwise available. The positions of atomic nuclei in crystals, especially of those of light atoms, can be determined precisely. Atomic motion can be directly measured and monitored as a function of temperature or pressure. Neutrons are especially sensitive to hydrogen, so that hydrogen motion can be followed in H-storage materials and water flow in fuel cells can be imaged. Residual stresses such as those deep within oil pipelines or in highway trusses can be mapped. Neutron-based measurements contribute to a broad spectrum of activities including engineering, materials development, polymer dynamics, chemical technology, medicine, and physics.

The NCNR's neutron source provides the intense, conditioned beams of neutrons required for these types of measurements. In addition to the thermal neutron beams from heavy water or graphite moderators, the NCNR has two liquid hydrogen moderators, or cold sources. One is a large area moderator and the other is smaller, but with high brightness. These moderators provide long wavelength guided neutron beams for industrial, government, and academic researchers.

There are currently 28 experiment stations: 12 provide high neutron flux positions for neutron physics, analytical chemistry, or imaging, and 16 are beam facilities for neutron scattering research. The subsequent pages provide a schematic description of our instruments. More complete descriptions can be found at www.ncnr.nist.gov/instruments/. The second guide hall is currently populated with seven instruments. Three new cold neutron instruments are under development, including a very small angle neutron scattering instrument, a quasi-white beam neutron reflectometer and a cold neutron imaging station.

The Center supports important NIST measurement needs, but is also operated as a major national user facility with merit-based access made available to the entire U.S. technological community. Each year, more than 2000 research participants from government, industry, and academia from all areas of the country are served by the facility (see pp. 55). Beam time for research to be published in the open literature is without cost to the user, but full

operating costs are recovered for proprietary research. Access is gained mainly through a web-based, peer-reviewed proposal system with user time allotted by a beamtime allocation committee twice a year. For details see www.ncnr.nist.gov/beamtime.html. The National Science Foundation and NIST co-fund the Center for High Resolution Neutron Scattering (CHRNS) that currently operates five of the world's most advanced instruments (see pp. 58). Time on CHRNS instruments is made available through the proposal system. Some access to beam time for collaborative measurements with the NIST science staff can also be arranged on other instruments.

WHY NEUTRONS?

Neutrons reveal properties not readily probed by photons or electrons. They are electrically neutral and therefore easily penetrate ordinary matter. They behave like microscopic magnets, propagate as waves, can set particles into motion, losing or gaining energy and momentum in the process, and they can be absorbed with subsequent emission of radiation to uniquely fingerprint chemical elements.

WAVELENGTHS – in practice range from ≈ 0.01 nm (thermal) to ≈ 1.5 nm (cold) ($1 \text{ nm} = 10 \text{ \AA}$), allowing the formation of observable interference patterns when scattered from structures as small as atoms to as large as biological cells.

ENERGIES – of millielectronvolts, the same magnitude as atomic motions. Exchanges of energy as small as nanoelectronvolts and as large as tenths of electronvolts can be detected between samples and neutrons, allowing motions in folding proteins, melting glasses and diffusing hydrogen to be measured.

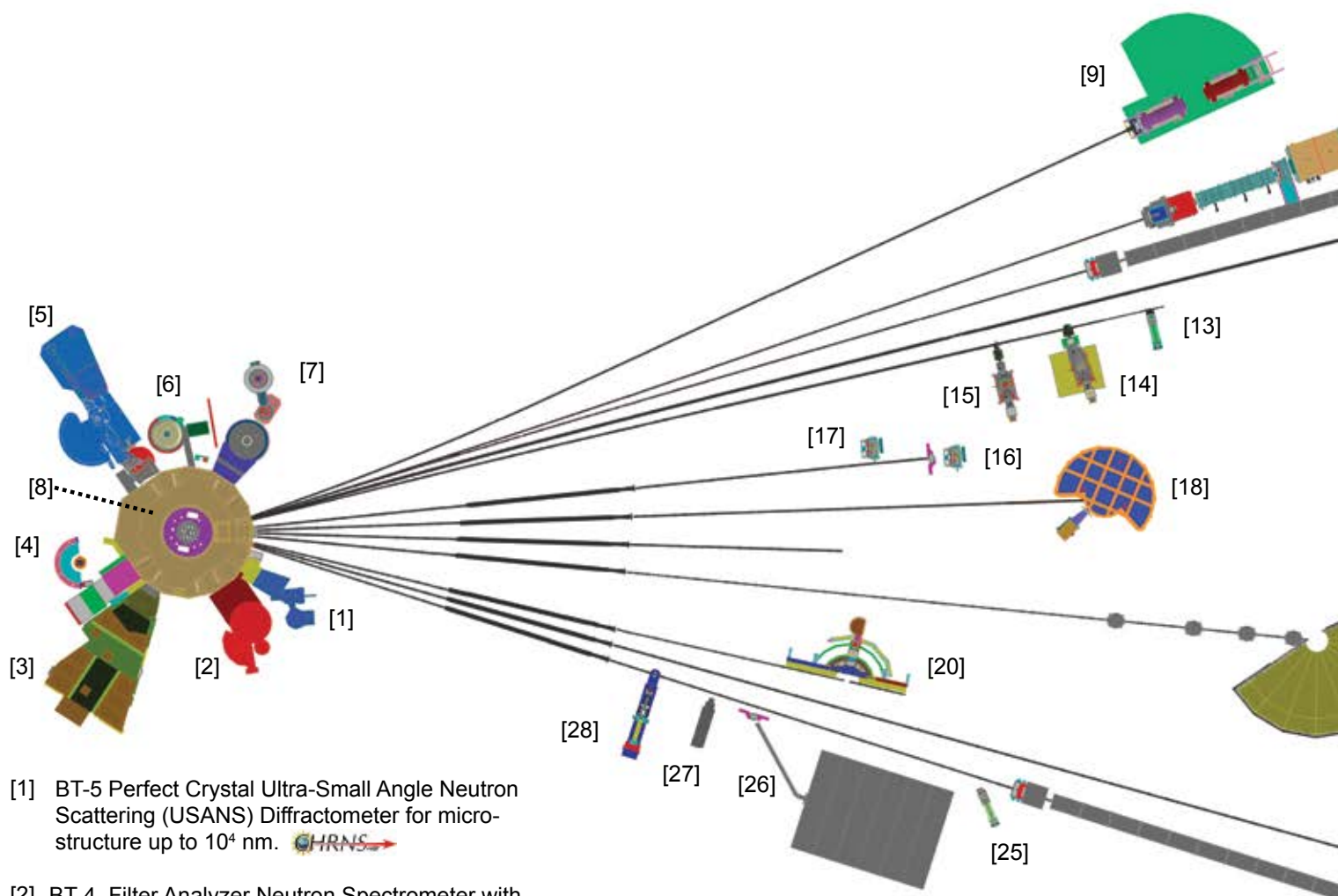
SELECTIVITY – in scattering power varies from nucleus to nucleus somewhat randomly. Specific isotopes can stand out from other isotopes of the same kind of atom. Specific light atoms, difficult to observe with x-rays, are revealed by neutrons. Hydrogen, especially, can be distinguished from chemically equivalent deuterium, allowing a variety of powerful contrast techniques.

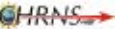
MAGNETISM – makes the neutron sensitive to the magnetic moments of both nuclei and electrons, allowing the structure and behavior of ordinary and exotic magnetic materials to be detailed precisely.

NEUTRALITY – of the uncharged neutrons allows them to penetrate deeply without destroying samples, passing through walls that condition a sample's environment, permitting measurements under extreme conditions of temperature and pressure.

CAPTURE – characteristic radiation emanating from specific nuclei capturing incident neutrons can be used to identify and quantify minute amounts of elements in samples as diverse as ancient pottery shards and lake water pollutants.

NIST Center for Neutron Research Instruments (as of Dec 2015)




[1] BT-5 Perfect Crystal Ultra-Small Angle Neutron Scattering (USANS) Diffractometer for micro-structure up to 10^4 nm. 

[2] BT-4 Filter Analyzer Neutron Spectrometer with cooled Be/Graphite filter analyzer for chemical spectroscopy and thermal triple axis spectrometer.

[3] BT-2 Neutron Imaging Facility for imaging hydrogenous matter in large components such as water in fuel cells and lubricants in engines, in partnership with General Motors and DOE.


[4] BT-1 Powder Diffractometer with 32 detectors; incident wavelengths of 0.208 nm, 0.154 nm, and 0.159 nm, with resolution up to $\Delta d/d \approx 8 \times 10^{-4}$.

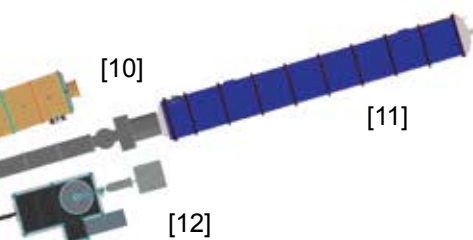
[5] BT-9 Multi Axis Crystal Spectrometer (MACS II), a cold neutron spectrometer for ultra high sensitivity access to dynamic correlations in condensed matter on length scales from 0.1 nm to 50 nm and energy scales from 2.2 meV to 20 meV. 

[6] BT-8 Residual Stress Diffractometer optimized for depth profiling of residual stresses in large components.

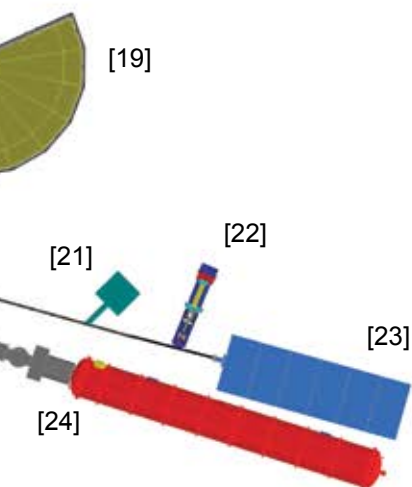
[7] BT-7 Thermal Triple Axis Spectrometer with large double focusing monochromator and interchangeable analyzer/detectors systems.


[8] VT-5 Thermal Neutron Capture Prompt Gamma-ray Activation Analysis Instrument used for quantitative elemental analysis of bulk materials. Generally used for the analysis of highly hydrogenous materials ($\approx 1\%$ H) such as foods, oils, and biological materials.


[9] NG-A Neutron Spin-Echo Spectrometer (NSE) for measuring dynamics from 5 ps to 100 ns. 



The Center for High Resolution Neutron Scattering (CHRNS) is a partnership between NIST and the National Science Foundation that develops and operates neutron scattering instrumentation for use by the scientific community. The following instruments are part of the Center: 1 (USANS), 5 (MACS II), 9 (NSE), 11 (NG-B SANS), and 18 (HFBS).



[10] NG-B 10 m SANS for macromolecular structure measurements. 

[11] NG-B 30 m SANS for microstructure measurements. 

[12] NG-C aCORN Neutron physics station for measurement of the correlation parameter between the electron and anti-neutrino in neutron beta decay.


[13] NG-D Cold neutron capture Prompt Gamma Activation Analysis, for quantitative elemental analysis of bulk materials, especially of hydrogenous ones.

[14] NG-D MAGIK off-specular reflectometer for studies of thin-film samples with in-plane structure.

[15] NG-D Polarized Beam Reflectometer (PBR) for measuring reflectivities as low as 10^{-8} to determine subsurface structure.

[16] NG-1 Cold Neutron Depth Profiling for profiling of subsurface elemental composition.

[17] NG-1 Detector development station.

[18] NG-2 Backscattering Spectrometer (HFBS) high intensity inelastic scattering instrument with energy resolution $< 1 \mu\text{eV}$, for studies of motion in molecular and biological systems. 

[19] NG-4 Disk Chopper Time-of-Flight Spectrometer for diffusive motions and low energy dynamics. Wavelengths from $\approx 0.18 \text{ nm}$ to 2.0 nm and energy resolutions from $\approx 2 \text{ meV}$ to $< 10 \mu\text{eV}$.

[20] NG-5 Spin-Polarized Triple Axis Spectrometer (SPINS) using cold neutrons with position sensitive detector capability for high-resolution studies.

[21] NG-6 Precision measurement of the magnetic dipole moment of the neutron.

[22] NG-6 Precision measurement of neutron flux.

[23] NG-6 Cold Neutron Imaging Facility for imaging hydrogenous matter in large components such as water in fuel cells and lubricants in engines.

[24] NG-7 30 m SANS for microstructure measurements, in partnership with ExxonMobil and University of Minnesota's IPrime.

[25] NG-7 Cold neutron test station.

[26] NG-7 Neutron Interferometry and Optics Station with perfect crystal silicon interferometer. A vibration isolation system provides exceptional phase stability and fringe visibility.

[27] NG-7 Neutron Physics Interferometry Test Bed for developing novel interferometry techniques.

[28] NG-7 Horizontal Sample Reflectometer allows reflectivity measurements of free surfaces, liquid/vapor interfaces, as well as polymer coatings.

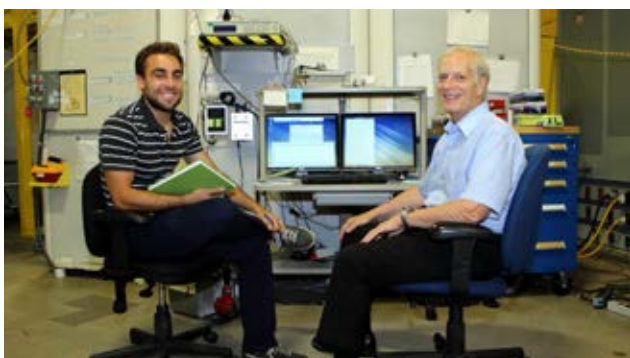
NCNR Images 2015



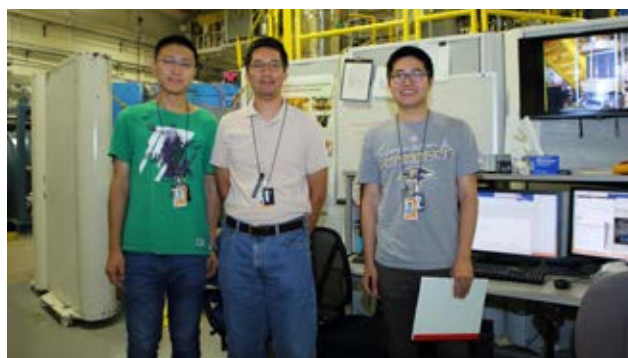
Kevin Martz from Richard Montgomery High School and Boualem Hammouda (NCNR) preparing for a high-pressure experiment at NGB 30m SANS.



The next generation of researchers learns about neutrons from the NCNR's Juscelino Leão during "Take Our Daughters and Sons To Work Day".



Chris Borg from the University of Maryland and Jeff Lynn (NCNR) at BT1 collecting highlight-worthy data from iron superconductors.



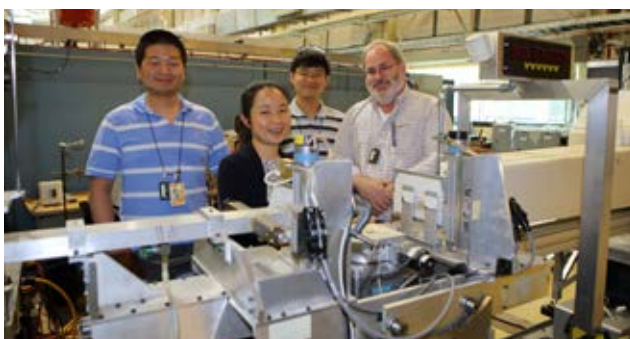
Wei He, Young Lee, and Jiajia Wen from Stanford University get ready to collect data on quantum spin liquids at MACS.



The NCNR's John Copley helps summer school students understand how neutron detectors work.



Michelle Calabrese from the University of Delaware conducts a rheo-SANS experiment at the NG7 30m SANS.



Jun Mao (U of Chicago), Guangcui Yuan (NCNR), Jing Yu (Argonne National Laboratory), and Thomas Seery (U of Connecticut) measure polymer brushes using the NG7 reflectometer.



Summer school students get pointers from the NCNR's Nick Butch on how to set up a successful experiment at DCS.



Summer school students anxiously await their first neutron data from BT7 under the guidance of Yang Zhao of the NCNR.



Abel Chuang from the University of California, Merced prepares a fuel cell for imaging at the BT2 Neutron Imaging Facility.



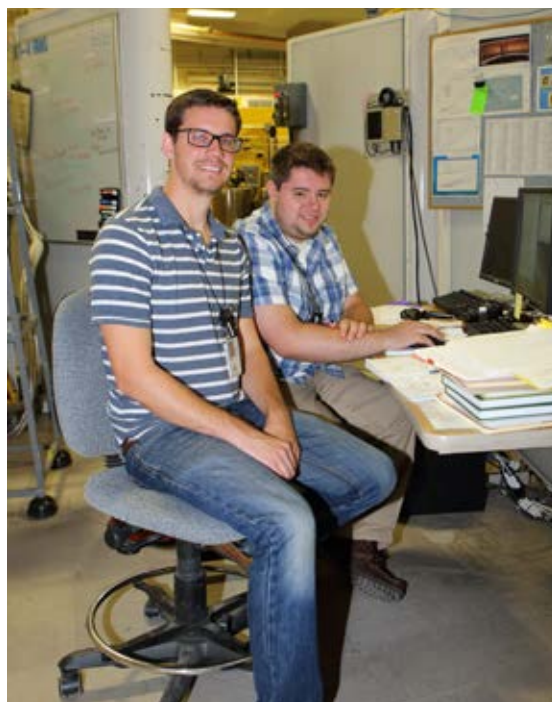
Adrian Rennie, Anders Olsson (Uppsala U, Sweden), and Majority Kwaambwa (Polytechnic of Namibia, Namibia) at BT5 USANS, carefully loading their samples.



Michael Huber (NCNR), Taisiya Mineeva (U of Waterloo, Canada), Chandra Shahi (Tulane U), Ke Li (Indiana U), and Ben Heacock (North Carolina State U) at the NG7 Neutron Interferometry and Optics Facility.



Yimin Wang from the University of Southern California collects data on the dynamics of ribonuclease at the NGA Neutron Spin Echo spectrometer.



At BT4 FANS, NIST SURF student John Collini from Rochester Institute of Technology experiences research first-hand with the help of the NCNR's Steve Disseler.

Probing the structure of CENP-A derived nucleosomes using small-angle neutron scattering with contrast variation

K. Gupta, N. Sekulic, G. D. Van Duyne, and B. E. Black



Chromatin is an amalgamated assembly of protein and DNA found within all eukaryotes that carries the cell's genetic instructions. The fundamental subunit of chromatin is the nucleosome, where just less than two turns of DNA (≈ 147 base pairs) wrap around an octamer of proteins called histones (H3, H4, H2A, and H2B) in a left-handed fashion (Fig. 1). Over 40 years ago, (SANS) measurements of chromatin leveraging contrast variation by isotopic exchange correctly determined the structural arrangement of the protein and DNA in this assembly [1-3], almost two decades before the first crystallographic structures became available from the Richmond group [4]. Today, over eighty such atomic structures of the nucleosome are available in the Protein Data Bank, revealing nearly identical structures within the context of the crystallographic lattice.

The faithful segregation of chromosomes to each daughter cell during cellular division underlies the basis for life. The centromere is a chromosomal locus necessary for accurate segregation during cell division. Errors in mitotic centromere function result in chromosome imbalances which are associated with cancer. Centromeres are defined by the presence of nucleosomes containing a histone H3 variant called CENP-A (Centromere Protein A) (for a review, see [5], Figure 1). A pressing question in this field of research is how the presence of this variant histone distinguishes the centromeric nucleosome and confers distinctive functional properties.

An important structural advance in the understanding of this histone variant arrived with the determination of an atomic structure of the heterotetramer of CENP-A in complex with histone H4 [6], a core component of a centromeric nucleosome and the experimental structure of the whole CENP-A nucleosome [7]. These data suggest that CENP-A-containing nucleosomes have the same protein/DNA stoichiometry and wind DNA in a left-handed manner similar to canonical nucleosomes, but still fall short of identifying specific features in CENP-A nucleosomes that recruit a number of proteins that direct kinetochore assembly and microtubule binding in mitosis. However, partially unwrapped DNA in CENP-A nucleosome [7] and altered angle between two heterodimers of CENP-A/H4 in tetrameric structure [6] indicate that structural identity of CENP-A nucleosome may be dynamic, requiring solution-based approaches to meaningfully interrogate these properties. The accessory protein called CENP-C binds to CENP-A derived nucleosomes and affects their structure and stability. Given its long history in the field of chromatin research, the SANS approach is ideally suited to approach many of these pressing structural questions, including how variant nucleosomes differ in structure and how binding of proteins like CENP-C modulates these properties.

The scattering facilities available at the NIST Center for Neutron Research have proven to be ideal for scattering of biological samples. While complementary small-angle x-ray scattering (SAXS) data is highly useful and provides additional

resolution to such an analysis, contrast variation by SANS is the only way to examine the distribution of the protein and DNA components in these macromolecular assemblies in solution.

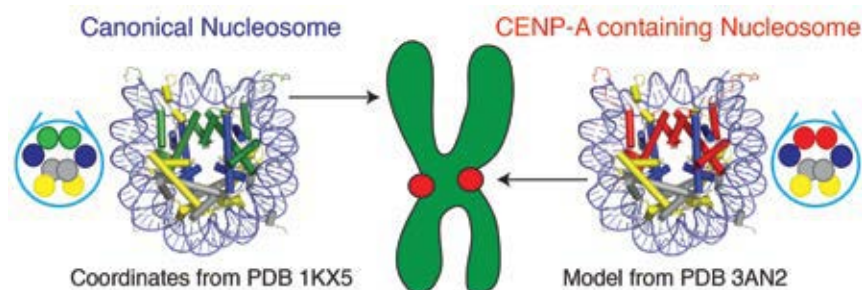


FIGURE 1: The atomic structure of the canonical nucleosome is shown (PDB 1KX5). Two turns of DNA (≈ 147 base pairs) wrap around an octamer of proteins called histones (H3 (green), H4 (blue), H2A (grey), and H2B (yellow)) in a left-handed fashion. Centromeric nucleosomes found at the centromere (red circle) are distinguished from canonical nucleosomes by the substitution of CENP-A (red) for H3.

In a recently published study in the journal *Science* [8], we applied a battery of biophysical approaches, including H-D exchange mass spectrometry and FRET experiments that demonstrated that CENP-A nucleosomes had properties distinct from those of canonical nucleosomes, and that these properties returned to a conventional form with increased rigidity when bound by a C-terminal fragment of CENP-C. To determine whether CENP-C binding leads to a steady-state structural change of nucleosomal DNA, we employed small-angle neutron scattering (SANS) with contrast variation, using NIST beam line NGB30. When CENP-C binds to reconstituted CENP-A nucleosome core particles, the pairwise distance distribution profiles (reflecting the shape of the particle in solution) substantially redistribute at contrast points strongly biased towards either the protein or DNA components (Fig. 2). The increase in larger interatomic vectors at the protein-dominated contrast point (D_2O volume fraction of 80 %) was expected to accompany an additional protein component (CENP-C). The pronounced redistribution of vectors to both smaller and larger distances in DNA-dominated contrast point (D_2O volume fraction of 20 %) when CENP-C is bound is attributed to compaction of the nucleosome core (smaller interatomic vectors) and opening of the nucleosome terminal DNA when CENP-C is bound (larger interatomic vectors); this interpretation is supported by our fluorescence and hydrogen-deuterium exchange experiments.

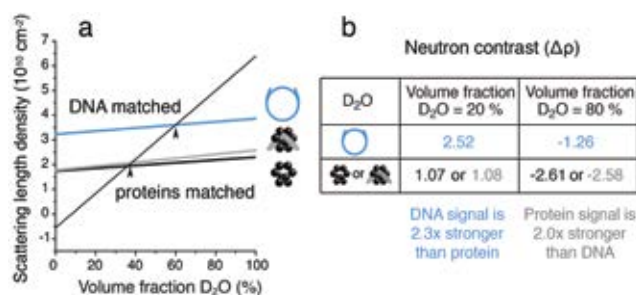


FIGURE 2: (a) Scattering length density of a CENP-A derived nucleosome with and without CENP-C (grey) bound. (b) Calculated contrast ($\Delta\rho$) of the protein and DNA components in neutrons.

Our study has revealed that CENP-C affects nucleosome shape and dynamics in a manner comparable to allosteric regulation of enzymes. And, we show that CENP-C depletion leads to rapid removal of CENP-A from centromeres, indicating their collaboration in maintaining centromere identity. These data suggest a model of epigenetic biology very distinct from the traditional view of nucleosomes as static scaffolds on which key functional molecules assemble. Instead, our data suggest

that histone variants can change the biological properties of nucleosomes through changes in shape, thus making nucleosomes active participants in cellular processes. This mode of nucleosome regulation and stabilization may well be common to other epigenetic processes. Indeed, the results reveal the possibility that other histone variants and histone post-translational modifications may operate in a similar fashion, for instance in the regulation of gene expression. Our study also demonstrates the utility and impact of the unique experimental resources available at the NCNR and their application to driving biomedical questions in the field of chromatin research.

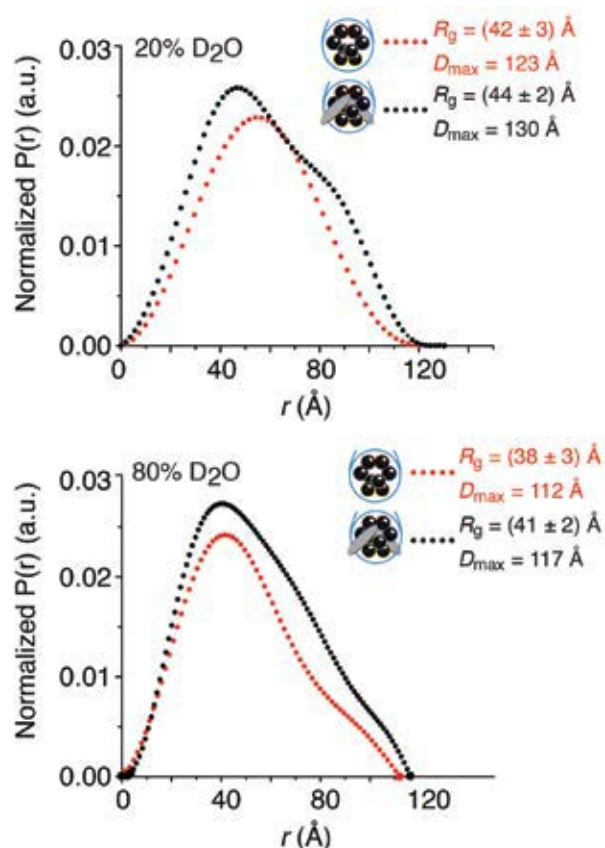


FIGURE 3: Shape distribution functions for CENP-A nucleosomes with (red) and without (black) CENP-C bound, at two different contrast points. DNA scattering dominates the upper plot (D_2O volume fraction = 20 %) while protein scattering dominates the lower plot (D_2O volume fraction = 80 %). The shape distribution profiles were derived from the primary data by Inverse Fourier Transform. Uncertainties reported are one standard deviation.

References

- [1] J. F. Pardon, *et al.*, *Nucleic Acids Res.* **2**, 2163 (1975).
- [2] P. Suau, *et al.*, *Nucleic Acids Res.* **4**, 3769 (1977).
- [3] R. P. Hjelm, *et al.*, *Cell* **10**, 139 (1977).
- [4] K. Luger, *et al.*, *Nature* **389**, 251 (1997).
- [5] N. Sekulic, *et al.*, *Trends Biochem. Sci.* **37**, 220 (2012).
- [6] N. Sekulic, *et al.*, *Nature* **467**, 347 (2010).
- [7] H. Tachiwana, *et al.*, *Nature* **476**, 232 (2011).
- [8] S. J. Falk, *et al.*, *Science* **348**, 699 (2015).

Targeting bacteria within the mammalian cell: endolysin PlyC entry point revealed

M. Barros¹, T. Vennermann², F. Heinrich^{1,2}, D. Nelson^{3,4}, and M. Lösche^{1,2}

Bacteriophage-encoded endolysins are a novel alternative to antibiotics that rapidly and specifically kill bacteria. These proteins are enzymes that facilitate the egress of new phages by degrading the bacterial peptidoglycan, provoking bacterial death from the inside. However, they can also lyse bacteria when externally administered. As a result, they offer a unique antimicrobial alternative, referred to as enzybiotics [1].

Opportunistic human pathogens such as *Streptococcus pyogenes*, cause a broad spectrum of diseases, ranging from pharyngitis to pneumonia, by colonizing the skin and mucosal surface. In the never-ending evolutionary tug-of-war between pathogens and their hosts, these bacteria have developed methods to invade human cells where they avoid surveillance by the immune system or, in modern times, antibiotic clearance. Thus, there is an urgent need for endolysins with the ability to penetrate cells so that they can target bacteria residing in intracellular and extracellular habitats.

The streptococcal C1 bacteriophage endolysin PlyC has a unique inherent ability to enter mammalian cells, without inflicting damage, while maintaining its bacteriolytic activity in the intracellular environment. To further evaluate its therapeutic potential, ex vivo studies were carried out which showed that PlyC gains cellular entry and clears intracellular streptococci at very small doses without compromising cell viability, implying that an unknown mechanism provides entry to the streptococci-specific endolysin into mammalian cells.

Research at the Institute for Bioscience and Biotechnology Research revealed that the PlyC binding domain, termed PlyCB, is sufficient to mediate entry into epithelial cells. PlyCB's highly positively charged binding surface contains a pocket-like structure [2] that interacts with phospholipids on the plasma membrane (Fig. 1). At CMU and the NCNR, we further investigated the molecular basis of PlyCB's ability to bind and cross the mammalian plasma membrane using synthetic model membranes known as tethered bilayer lipid membranes [3]. Complementary surface-sensitive techniques confirmed membrane integrity during PlyCB exposure and quantified membrane-binding affinity [4]. PlyCB interaction with neutral membranes is negligible, but the protein interacts strongly with membranes that contain

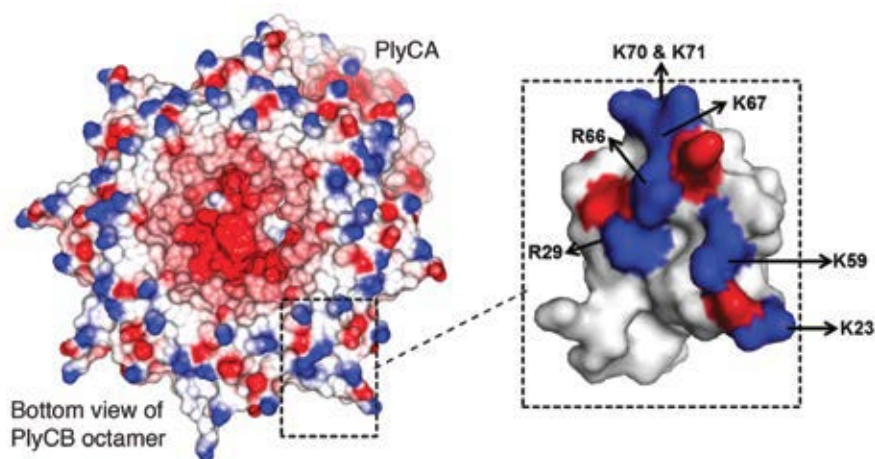


FIGURE 1: Electrostatic surface potential of the PlyCB binding domain. The protein surface is color-coded according to electrostatic potential: positive and negative charges are shown in blue and red, respectively. The enlarged view at the right shows a pocket-like structure that is composed of several cationic residues. These appear to be crucial for specific phospholipid binding and initiating PlyC internalization into mammalian cells.

phosphatidylserine (PS) above a concentration threshold, while its interaction is much weaker with other anionic lipids, demonstrating specificity for PS (Fig. 2). Neutron reflection showed that PlyCB binding to the membrane surface is followed by penetration into the hydrophobic

¹Department of Physics, Carnegie Mellon University, Pittsburgh, PA 15213

²NIST Center for Neutron Research, National Institute of Standards and Technology, Gaithersburg, MD 20899

³Institute for Bioscience and Biotechnology Research, University of Maryland, Rockville, MD 20850

⁴Department of Veterinary Medicine, University of Maryland, College Park, MD 20742

membrane core (Fig. 3), while impedance spectroscopy confirms that the membrane integrity is not negatively affected by PlyCB binding.

Those findings provide a mechanistic understanding of how PlyCB binds to cell membranes and a lead for further research on the biological translocation process. After the initial plasma membrane interaction and translocation, PlyC is transported inside the cell where it eventually encounters the streptococci that it beneficially clears within the host. PlyC's entry point into the cell, PS, is primarily located in the inner leaflet of the plasma membrane where it would not be available for binding external endolysin. However, in cells stressed by bacteria assault and inflammation, lipid asymmetry is compromised [5]: PS may be over proportionally exposed on the outer plasma membrane, thus attracting the therapeutic agent whenever it is needed most. Future cell biological studies will investigate this possibility further.

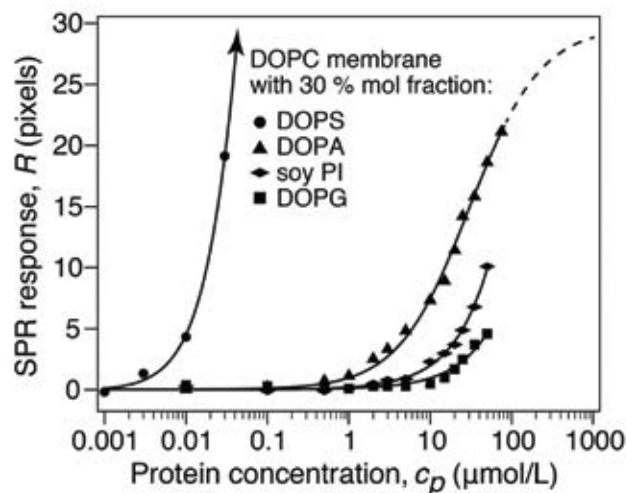


FIGURE 2: Affinity of PlyCB to negatively charged tethered lipid bilayer membranes containing neutral DOPC and anionic lipids at a mole fraction of 30 % under physiologically relevant conditions. PlyCB binds poorly to PA, PG and PI (phosphatidic acid, phosphatidylglycerol and phosphatidylinositol – membrane lipids that bear the same charge as phosphatidylserine but have slightly different molecular structures). The much stronger protein adsorption to PS shows clearly the specificity of PlyCB to this plasma membrane lipid.

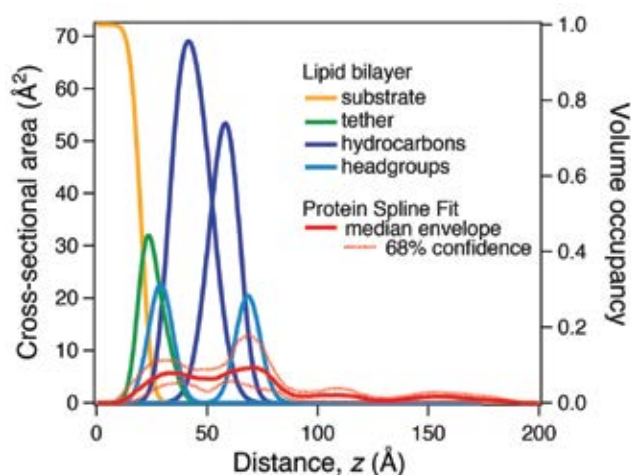


FIGURE 3: Structural envelope of membrane-bound PlyCB at a solution concentration of 600 nmol/L on a tethered bilayer lipid membrane composed of DOPC:DOPS 70:30. The composition-space model used to interpret the neutron reflection of the protein-membrane complex describes the spatial distribution of the membrane components as a sum of two error functions while the protein envelope was modeled by free-form splines [6]. Monte-Carlo resampling was used to determine the 68 % confidence limits of the profiles. This result shows that PlyCB inserts deeply into the membrane and spans its entire thickness.

References

- [1] D. Nelson, L. Loomis, V. A. Fischetti, *Proc. Natl. Acad. Sci. USA* **98**, 4107 (2001).
- [2] S. McGowan, A. M. Buckle, M. S. Mitchell, J. T. Hoopes, D. T. Gallagher, R. D. Heselpoth, Y. Shen, C. F. Reboul, R. H. Law, V. A. Fischetti, J. C. Whisstock, D. Nelson, *Proc. Natl. Acad. Sci. USA*, **109**, 12752 (2012).
- [3] R. Budvytyte, G. Valinicius, G. Niaura, V. Voiciuk, M. Mickevicius, H. Champman, H. Z. Goh, P. Shekar, F. Heinrich, S. Shenoy, M. Lösche, D. J. Vanderah, *Langmuir* **29**, 8645 (2013).
- [4] Y. Shen, M. Barros, T. Vennemann, D. T. Gallagher, Y. Yin, S. B. Linden, R. D. Heselpoth, D. J. Spencer, D. M. Donovan, J. Moutl, V. A. Fischetti, F. Heinrich, M. Lösche, D. Nelson, Manuscript in preparation (2015).
- [5] B. Fadeel, D. Xue, *Crit. Rev. Biochem. and Mol. Biol.* **44**, 264 (2009).
- [6] F. Heinrich, M. Lösche, *Biochim. Biophys. Acta* **1838** (9), 2341 (2014).

Structural interactions of a voltage sensor toxin with lipid membranes

M. Mihailescu^{1,2}, D. Krepiy³, M. Milescu^{3,4}, K. Gawrisch⁵, K. J. Swartz³, and S. H. White⁶

A variety of toxins from venomous animals are known to alter the activity of diverse ion channel proteins including voltage, stretch, and ligand-activated cation channels. Medical conditions that affect the central and peripheral nervous systems are caused by dysfunction of ion channel proteins, in particular voltage-gated ion channels. Understanding how channel activities are altered by their interactions with toxins found in nature has significant implications for the treatment of cardiac and neuronal disorders.

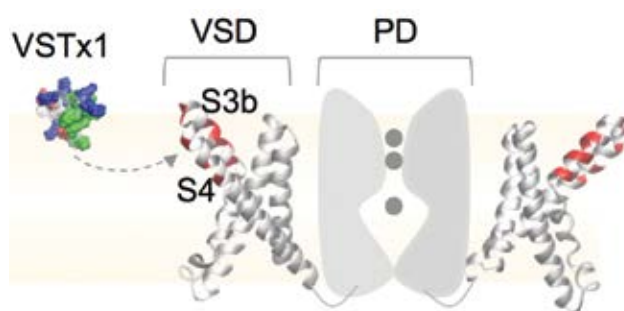


FIGURE 1: Representations of the molecular structures of VSTx1 toxin [2] and a voltage-gated potassium channel [1]. Only two opposing units of the tetramer are shown. Segments of the Voltage-Sensor Domains (VSD) that are targeted by VSTx1 are highlighted in red [3]. The pore domain (PD) is shown schematically.

Voltage-gated (VG) ion channels are key players in the electrical signaling in the nervous system. In vivo, their opening and closing permits ion conduction across cellular membranes (channel gating), and is regulated by the membrane polarity and interactions between the channels and small molecules. They assemble in cellular membranes as tetramers that delineate two loosely connected domains: a pore domain that houses the ion conduction pathway and voltage-sensing domains that

are sensitive to the cellular membrane potential [1] (Fig.1). Electromechanical coupling between those two types of domains make the channels open or close in response to variations in transmembrane potential.

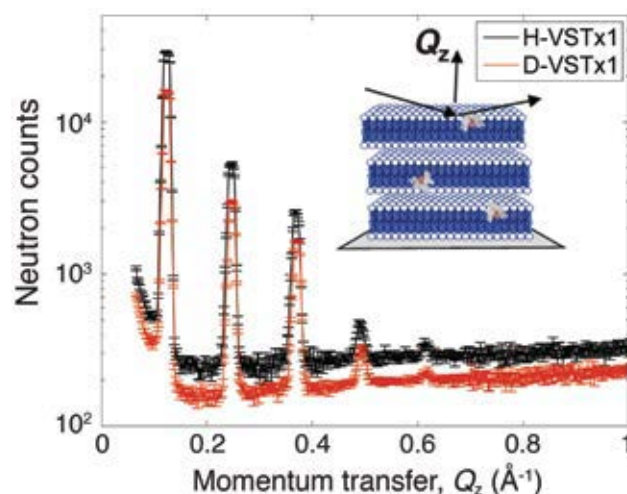


FIGURE 2: Diffraction data for VSTx1 (in either protonated or deuterated forms) incorporated in membrane systems for neutron diffraction. Diffraction data was collected at MAGIK at NCNR.

Many toxins inhibit VG channels by targeting the external vestibule of the ion conduction pore and blocking the flow of ions. In other cases, the toxins modify gating by interacting with the voltage-sensing domains. The voltage-sensor toxin VSTx1 from tarantula venom is a small protein known to bind to voltage-sensitive domains of potassium VG channels and to modify their gating mechanism. Although tarantula toxins have been shown to have low affinity for the voltage-sensors outside the lipid membrane environment [4], and the membrane is thought to play an important role in their activity, the structural interactions between these toxins and lipid membranes are poorly understood.

¹Institute for Bioscience and Biotechnology Research, University of Maryland, Rockville, MD 20850

²NIST Center for Neutron Research, National Institute of Standards and Technology, Gaithersburg, MD 20899

³Porter Neuroscience Research Center, National Institute of Neurological Disorders and Stroke, National Institutes of Health, Bethesda, MD 20892

⁴University of Missouri, Columbia, MO 65211

⁵National Institute on Alcohol Abuse and Alcoholism, National Institutes of Health, Bethesda, MD 20892

⁶University of California, Irvine, Irvine, CA 92697

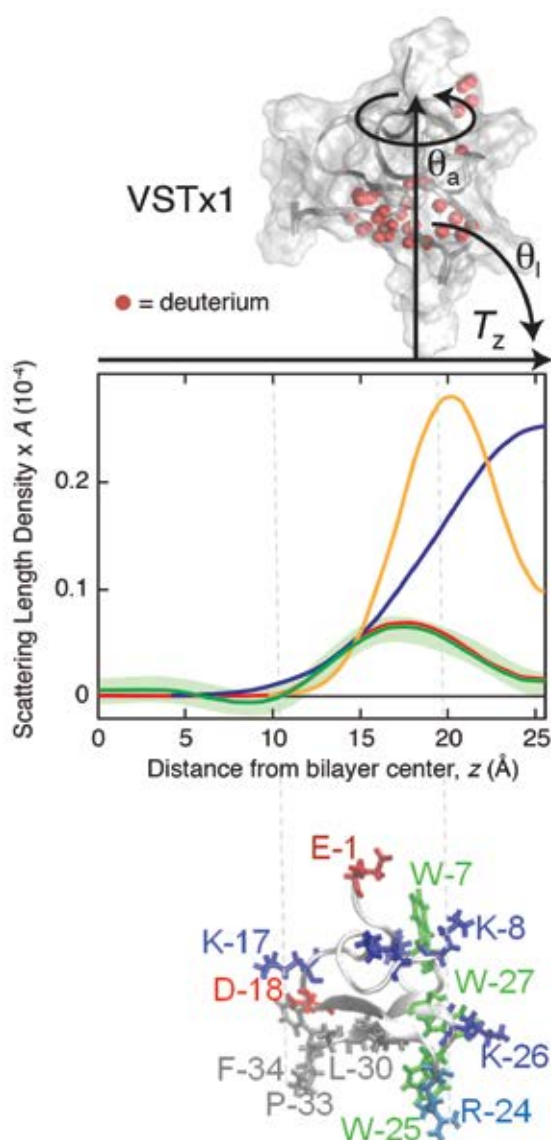


FIGURE 3: Scattering length density distributions (middle graph) for the lipid phosphocholine group (yellow), water (blue), and the deuterated patch of VSTx1 (green). The distributions were determined by deuterium difference analysis. Upper inset: representation of VSTx1 structure with deuterated sites highlighted in red. Lower inset: structure of VSTx1 in the preferred orientation, showing a brush of basic residues (blue) pointing toward the aqueous phase and the hydrophobic C-terminal tail (gray) pointing toward the membrane interior.

Here, we examined the molecular details of the interactions of the VSTx1 toxin with lipid membranes [5]. We produced active forms of the VSTx1 carrying stable deuterium isotopes, from its synthetic, linear form, and tested its inhibitory function against voltage-gated potassium channels expressed in oocyte membranes using voltage-clamp techniques [5]. The toxin was then incorporated in model lipid membranes (Fig. 2) for neutron diffraction

studies performed at the NCNR. Deuteration schemes of the toxin, lipid, and water, in conjunction with neutron diffraction methods, were used to show the relative distributions of these components in the membrane (Fig. 3). Specific deuterium labeling was applied to a group of amino acids of VSTx1 to highlight a particular region on the surface of the toxin that is thought to be implicated in binding to the voltage sensors [6]. It was found that upon VSTx1 partitioning in the phospholipid membrane, the deuterated patch of amino acids positions itself close to the surface of the membrane, just below the phosphate lipid head group region. This is the region of the membrane that is also explored by certain segments of the voltage sensors during VG channel activation (Fig. 1). Furthermore, the deuterium profiles found by specific deuteration enabled calculations of the orientation of the toxin in membranes by molecular modeling, starting from existing NMR structures of VSTx1 [2]. It was thus found that VSTx1 adopts a preferred orientation in the membrane, exposing the binding surface laterally in the membrane so as to facilitate formation of the toxin-channel complexes. The more flexible C-terminus of VSTx1 was found to point toward the membrane interior, possibly enabling fast lateral propulsion of the toxin in the membrane, in search for its target on the channel.

Other measurements from this study revealed that the toxin distorts the membrane to produce thinning and increased disorder of the hydrocarbon core [5]. Because the conformation of voltage sensors in membrane is thought to be strongly dependent on the lipid membrane environment [7], structural perturbations of the membranes under the action of voltage-sensor toxins may indirectly affect ion channel activities.

Our studies by neutron diffraction were the first to clearly describe the structural interactions of a voltage-sensor toxin with the lipid membrane and set the ground for understanding how the pharmacology of these toxins interacting with voltage sensors can be modulated by membrane properties.

References

- [1] S. B. Long *et al.*, *Nature* **450**, 376 (2007).
- [2] H. J. Jung *et al.*, *Biochemistry* **44**, 6015 (2005).
- [3] A. A. Alabi *et al.*, *Nature* **450**, 370 (2007).
- [4] V. Ruta *et al.*, *Nature* **422**, 180 (2003).
- [5] M. Mihailescu *et al.*, *PNAS* **111**, E5463 (2015).
- [6] K. J. Swartz *et al.*, *Toxicon* **49**, 213 (2007).
- [7] M. Milescu *et al.*, *Nature Struct Mol Biol* **16**, 1080 (2009).

Molecular understanding of high CO₂ adsorption capacity in chabazite zeolites

M. R. Hudson¹, C. M. Brown^{1,2}, T. D. Pham², and R. F. Lobo²

The large-scale capture and sequestration of carbon dioxide (CO₂) from pre-combustion, post-combustion, and natural gas mixtures have become important technological and environmental targets to mitigate the effect of greenhouse gases on global climate change. Conventional CO₂ capture using primary alkanolamine scrubbers consumes large amounts of energy for regeneration. Nanoporous materials such as carbon molecular sieves, zeolites, and MOFs have been studied for CO₂ separations and capture because of their high internal surface area, high micropore volume, chemical tunability, fast adsorption/desorption kinetics, and low heats of adsorption [1].

Chabazite (CHA) is a small pore zeolite consisting of a double 6-membered ring (D6R) as the basic building unit with one large ellipsoidal cavity accessed by six 8-membered ring windows (8MR). CHA-type zeolites provide improved hydrothermal stability over other zeolites, an important property in the selective catalytic reduction of NO_x and moist flue-gas applications. CHA has also been shown to have high selectivity for light olefins in the conversion of methanol to olefins process and demonstrated potential in gas separations, such as CO₂ from N₂ in flue gas mixtures. Extra-framework cations present in Al-exchanged zeolite frameworks play important roles in determining the adsorption properties. Adsorption measurements reveal that the CHA samples with higher aluminum content have higher adsorption capacity. We considered the adsorption properties and site-specific adsorption properties of CO₂ in pure, high, and medium silica CHAs (Si/Al = ∞, = 12, = 6, respectively) with varied cation-exchange (Li⁺, K⁺, Na⁺). These insights were obtained by combining in-situ X-ray (XRPD) and neutron powder diffraction (NPD) methods using Fourier difference

mapping to locate the adsorbed CO₂ and correlating the results with adsorption measurements. This allows us to elucidate the atomic origin of the adsorption properties across a series of cationexchanged zeolites, which aids in the engineering of improved CO₂ adsorbents [2].

Figure 1 depicts the locations of alkali metal cations typically observed in highsilica CHAs. From Rietveld refinement of powder diffraction data, we observed Li and Na at the 6MR window, as expected as this coordination environment is the most favorable in CHA for small cations. In this position, each Li⁺ or Na⁺ is effectively coordinated with 3 oxygen atoms of the framework. Due to ionic radii difference ($r_{\text{Na}^+} = 1.16 \text{ \AA}$, $r_{\text{Li}^+} = 0.73 \text{ \AA}$), Na⁺ lies higher above the plane of the 6MR ($\approx 22^\circ$) measured from the Si in the ring compared to Li-CHA-6 ($\approx 9.6^\circ$). These angles are slightly larger in Li- and Na-CHA-12. On the other hand, the larger K⁺ cation sits preferentially in the middle of the 8MR where it is coordinated with 4 oxygen atoms of the zeolite framework. In addition, K⁺ is observed on a position above the 6MR where it is only coordinated with 3 oxygen atoms of the zeolite framework.

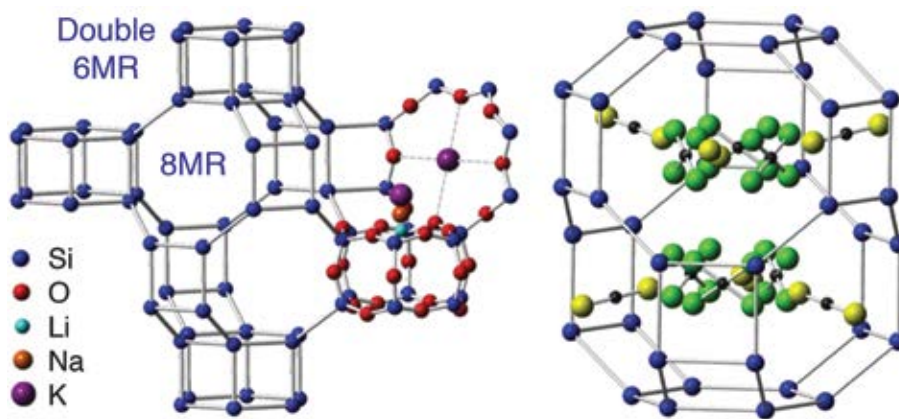


FIGURE 1: (Left) Illustration of the CHA structure and typical cation locations in the zeolites. (Right) CO₂ adsorption sites in Si-CHA with framework oxygen atoms omitted for clarity. Site A: 8MR, yellow CO₂ oxygen atoms; Site B: cage, green CO₂ oxygen atoms.

Dispersive interactions are the primary contributors to the adsorption energy in CHA and are determined by the distances between the carbon and oxygen atoms of

¹NIST Center for Neutron Research, National Institute of Standards and Technology, Gaithersburg, MD 20899

²University of Delaware, Newark, DE 19716

CO₂ molecule to the surrounding oxygen atoms of the framework. The refinement of XRPD and NPD patterns of CO₂ on pure silica CHA resulted in the identification of two adsorption sites for CO₂: (1) locating in the 8MR and (2) in the ellipsoid cages of CHA framework (Fig. 1). In the CHA 8MR, the preferred adsorption site (A) is the center of the CHA window in which each carbon atom in CO₂ molecule has maximal close contacts with the 8 oxygen atoms of the 8MR such that two O_{8MR} across the ring from each other give an angle O_{8MR}-C_{CO2}-O_{8MR} = 180°. From XRPD refinement of CO₂ in Si-CHA, the CO₂ – 8MR oxygen atom distances were determined to be from 3.129(6) Å to 3.410(4) Å, and with $d(\text{O}_{\text{CO2}}-\text{O}_{\text{CHA}})$ between ca. 3.18 Å to 3.98 Å. Another CO₂ adsorption site (B) in pure silica CHA is inside the ellipsoidal cage where the carbon atom has the most effective contact distances with 4 framework oxygen atoms and the CO₂ oxygen atoms also have effective contact distances with 4 to 5 framework oxygen atoms each. Overall, these considerations explain the high occupancy of CO₂ at site A in CHA zeolites, or indeed in 8MR zeolites in general.

Two CO₂ adsorption sites were determined in Li-CHA and Na-CHA zeolites by Fourier analysis (Fig. 2). The distance between Na⁺ and O_{CO2} in site A (3.605(0) Å) is much shorter than that for the Li⁺ (4.307(0) Å) leading to a more effective electrostatic interaction. The CO₂ second site in these zeolites is end-on coordination with the cation, M⁺...O=C=O, at distances of 2.68(7) Å (Na⁺) and 2.3(2) Å (Li⁺). The linear CO₂ molecule is tilted toward the 4MR window to achieve closer contact with framework oxygen atoms. This adsorption site can be viewed as B' being a rotation and translation of the all-silica site (B). Since the Li⁺...O=C=O distance is shorter than that in Na⁺-CHA, the CO₂ contact angle is more acute, $\angle \text{Li}^+ \cdots \text{O}=\text{C}=\text{O} \approx 144^\circ$ vs. $\angle \text{Na}^+ \cdots \text{O}=\text{C}=\text{O} \approx 163^\circ$, having more effective dispersive interaction with the framework. Because the interaction energy of the large quadrupole moment of CO₂ ($14.3 \times 10^{-40} \text{ C m}^2$) with an inhomogeneous electric field of zeolite is highest in 8MR zeolites, site A (8MR) is still a major adsorption site in alkali-exchanged CHA even though open metal cations provide an additional strong binding site in the cage (B') through enhanced electrostatic interaction.

In solid CO₂, molecules of CO₂ are arranged in their lowest energy configuration where an O atom of one CO₂ molecule is in close contact with more than 10 oxygen atoms and C atom also has close contact with 6 oxygen atoms of other CO₂ ($d_{\text{C-O}} \approx 3.11 \text{ Å}$), which is the distance we found in the 8MR. Further, in the cases of Li- and Na-CHA-12 at low CO₂ doses, there is an overall similarity of

the positions and occupancies of the two CO₂ sites (A, B') with $\angle \text{Li}^+ \cdots \text{O}=\text{C}=\text{O} \approx 142^\circ$ and $\angle \text{Na}^+ \cdots \text{O}=\text{C}=\text{O} \approx 166^\circ$ and the cation-CO₂ distance are identical to those in CHA-6 at 2.302(5) Å (Li⁺) and 2.59(8) Å (Na⁺).

Refinement of the K-CHA-12 data show that K⁺ behaves quite similarly to Cu²⁺ in which the majority of the CO₂ is found in the 8MR and only a small fraction of the adsorbate is found with an end-on CO₂ coordination with the cations. Interestingly, in K-CHA-6 with the higher concentration of K⁺ partially blocking more of the 8MR window, the occupancy of the second CO₂ site (C) in the cage is significantly increased. The increase in interaction energy is due to the CO₂ coordination to two K⁺ cations (across 6MR-6MR or 6MR-8MR) being more efficient in lower silica K-CHA-6 with a K⁺...O=C=O distance approx. 3 Å. In this configuration, the oxygen and carbon atoms also have a number of attractive interactions with framework oxygen atoms.

Structural properties of Chabazite zeolites dosed with CO₂ were determined from in-situ powder X-ray and neutron diffraction measurements. The 8MR (A) was identified as the major CO₂ adsorption site in pure silica CHA due to the high number of close contacts to the framework oxygen atoms to the CO₂. The exchanged cations in charged CHA frameworks are open metal ions providing strong binding sites through induced polarizability of CO₂. CO₂ is coordinated end-on to cations with the molecular axis tilted to the framework to maximize its dispersion interaction. The population of the direct coordinated adsorption sites of CO₂ with these metal cations decreases with the hardness of cation, except for K-CHA-6, where the bridged complexes of CO₂ and two K⁺ cation sites were formed with higher interaction energy than a single cation adsorption site. Additionally, a major CO₂ adsorption site in the 8MR, previously determined in Cu-CHA [3], was still observed in these cation-exchanged CHAs due to high van der Waals and quadrupole interactions. The type of structural determination completed here is essential in the understanding and design of better adsorbent materials for CO₂ capture and separation technologies.

References

- [1] T.-H. Bae, M. R. Hudson, J. A. Mason, W. L. Queen, J. J. Dutton, K. Sumida, K. J. Micklash, S. S. Kaye, C. M. Brown, J. R. Long, *Energy Environ. Sci.* **6**, 138 (2013).
- [2] M. R. Hudson, T. D. Pham, C. M. Brown, R. F. Lobo, *ChemSusChem* **7**, 2959 (2014).
- [3] M. R. Hudson, W. L. Queen, J. A. Mason, D. W. Fickel, R. F. Lobo, C. M. Brown, *J. Am. Chem. Soc.* **134**, 1970 (2012).

Predicting long-time material behavior with neutrons

M. T. Cicerone^{1,2}, Q. Zhong¹, and M. Tyagi^{1,3}



Over the past 10 years there have been many reports of correlations between picosecond (ps) or nanosecond (ns) dynamic processes in liquids or glasses, and long-time properties of these systems such as diffusion or viscous flow. Our recent work [1] uses neutron scattering data to build a framework that explains these curious correlations. In providing that framework, the work also presents a surprising picture of relaxation in liquids. It shows that dynamics in liquids are spatially heterogeneous, where some nanometer-sized regions of liquids exhibit dynamic processes that are distinct from those in nearby regions, but that these distinctions typically last less than 10 ps. With this picture of heterogeneous dynamics in mind, we were able to predict self-diffusion rates, and for the first time provide a clear molecular picture for an enigmatic process known as Johari-Goldstein (JG) relaxation.

Sugar-based glasses have been used for decades to encapsulate and stabilize therapeutic proteins, vaccines, and other biological structures and materials. Although this approach has been used widely in biopharmaceutics and other fields, the fundamental mechanisms by which these glasses stabilize biological molecules are not understood. Ten years ago, we showed that a signature in neutron backscattering correlated with protein stability in these glasses [2], and that this correlation was a candidate for a rapid and reliable stability prediction method. The correlation was somewhat surprising since the characteristic time for the neutron-material interaction is on the order of ns, whereas the characteristic time for protein degradation is on the order of months. Nonetheless, the correlation proved to be very robust for protein aggregation and chemical degradation processes [3].

We proposed that diffusive processes might provide a mechanistic link between the ns-ps dynamics and protein degradation processes, since the degradation processes should be transport-limited. There had been a number of studies linking viscous flow and short-time dynamics; however, translational diffusion and viscous flow do not track one another in general. In an effort to test our hypothesis we performed incoherent quasielastic neutron

scattering (QENS) on five common liquids at temperatures ranging from 4 K to well above the melting temperature using the Disk Chopper Spectrometer at the NCNR.

The most surprising feature of the data was that it clearly showed two dynamic states for molecules. Below the melting temperature (in the non-crystallized, supercooled state) most molecules are tightly caged (TC) by their neighbors and are unable to move more than 1 % of their diameter on a picosecond timescale. On the other hand, a small fraction of molecules are more loosely caged (LC) and can move by more than 10 % of their diameter on the same timescale. As temperatures are lowered, an increasingly large fraction of molecules are tightly caged, and the distance that these molecules can move becomes increasingly small. On the other hand, the molecules that remain mobile (loosely caged) can move the same distance, independent of temperature! Particularly surprising was that this two-state dynamic picture appeared to persist even above the melting temperature (see Fig. 1).

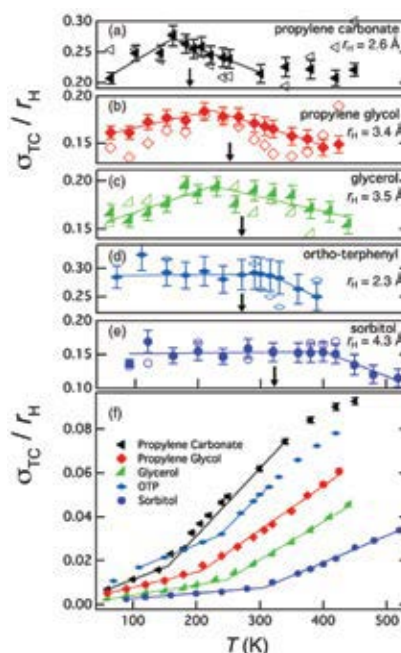


FIGURE 1: Confinement length scale (σ) for LC (a)-(e) and TC (f) molecules in the two-state model at 1 ps (solid symbols) and 10 ps (hollow symbols). Arrow indicates T_g for each material and r_H is the hydrodynamic radius.

¹NIST Center for Neutron Research, National Institute of Standards and Technology, Gaithersburg, MD 20899

²Institute for Physical Science and Technology, University of Maryland, College Park, MD 20742

³Department of Materials Science and Engineering, University of Maryland, College Park, MD 20742

We usually think of liquids as being dynamically homogeneous – that molecules in one region of the liquid should jostle about just like molecules in another region of the liquid. While this is certainly true on the timescales we usually experience or measure (nanoseconds and longer), it appears not to be true on timescales of less than 10 ps. Hints of such a two-state dynamic picture have surfaced occasionally over the past century. In 1923, C.V. Raman was the first to suggest the idea that molecules in liquids are found in two distinct dynamic populations at short times. Since then, other researchers have proposed similar two-state dynamic models. In 1970, Johari and Goldstein identified a weak, but apparently ubiquitous relaxation processes in liquids that occurs on a timescale faster than the slowest (α) process associated with viscous flow, but faster than the ps timescale dynamics associated with rattling of molecules in a cage of its neighbors. Since the 70s, this Johari-Goldstein β relaxation (β_{JG}) has been studied extensively, but no clear molecular picture has emerged.

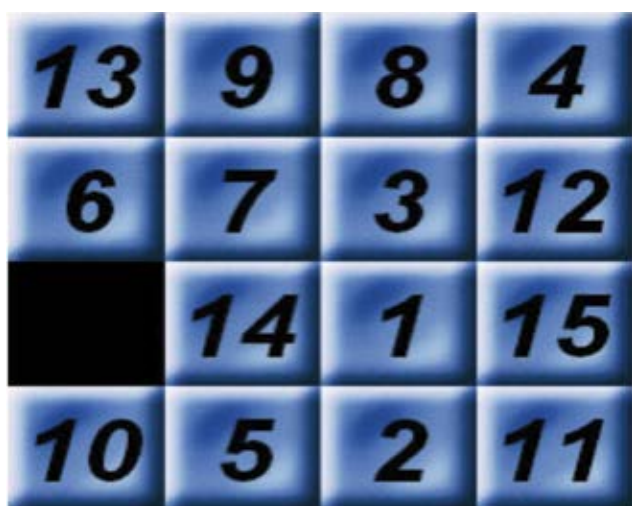


FIGURE 2: Dynamics in liquids on a sub-ps timescale resemble a game of 15. Molecules can move substantially only when molecules in their vicinity are in rare configurations that allow large steps. Otherwise, molecules move only very little.

Through the temperature dependence of the two-state behavior observed, we were able to formulate a mechanism for molecular motion that provides a simple picture of the β_{JG} process and also uncovers details of a so-called “hopping” diffusion mechanism. The proposed mechanism resembles a game of 15 (see Fig. 2). Here, each molecule is either tightly caged by its neighbors (TC) and essentially immobile, or loosely caged (LC) and able to move about. LC molecules explore their available volume quickly, within a few picoseconds, so their positions quickly randomize within their available volume. Substantial motion of TC

molecules occurs only when an exchange occurs between TC and LC states. In addition to allowing us to calculate translational diffusion that occurs one molecule at a time as molecules become loosely caged, we were able to correctly calculate the β_{JG} relaxation times as the timescale for molecules becoming loosely caged from a previously TC state (Fig. 3).

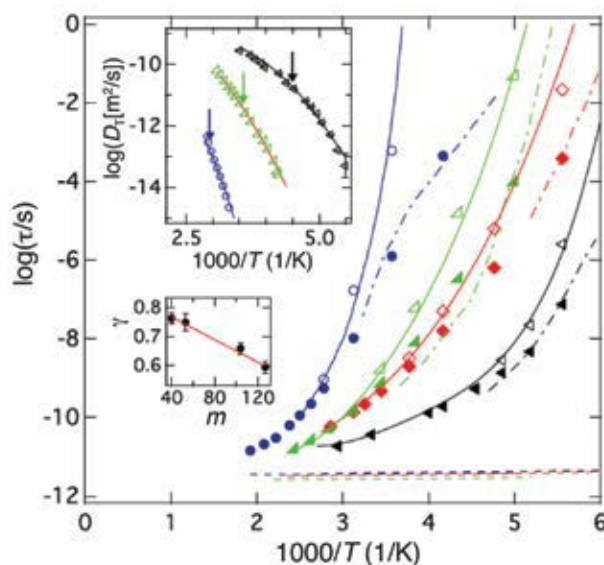


FIGURE 3: Calculated relaxation times based on two-state model: JG times as solid symbols, α -relaxation as hollow symbols, fast- β process as dashed lines. Measured relaxation times are shown as solid lines. Upper inset shows predicted and experimental diffusion constants. Lower inset shows the correlation between γ (spatial correlation parameter) and fragility.

This work provides a coherent molecular picture that explains key aspects of molecular transport and relaxation in liquids and glasses, and sets the groundwork for quantitatively predicting degradation rates of therapeutic proteins in sugar-based dried (glassy) formulations.

References

- [1] M. T. Cicerone, Q. Zhong, M. Tyagi, *Physical Review Letters* **113**, 117801 (2014).
- [2] M. T. Cicerone, J. F. Douglas, *Soft Matter* **8**, 2983 (2012).
- [3] M. T. Cicerone, C. L. Soles, *Biophysical Journal* **86**, 3836 (2004).

Exploring new mixed-valence manganese oxides with neutron diffraction

A. M. Larson¹, P. Moetakef¹, K. Gaskell¹, G. King², C. Brown^{3,4}, and E. E. Rodriguez¹

Manganese oxides are relevant not only for practical applications such as cathode materials in rechargeable batteries [1], but also for their fundamental properties such as complex magnetism. The mixed-valence Mn (i.e., Mn^{3+} and Mn^{4+}) oxides with the perovskite crystal structure display remarkable properties such as colossal magnetoresistance [2], whereby the resistance of the oxide changes orders of magnitude upon the application of an external magnetic field. This interesting response arises from the mixed-valence states of the manganese in the crystal lattice, and from the so-called Goodenough-Kanomori rules [3]. Our search for other manganese oxides with similar properties led to a diverse array of $A_x\text{MnO}_2$ compounds with mixed Mn^{3+} and Mn^{4+} states. We have recently explored [4] one particular crystal structure type known as hollandite that is part of the $A_x\text{MnO}_2$ family. We found that the magnetic properties of hollandites can be manipulated through substitution of other magnetic cations onto the Mn framework. Using powder neutron diffraction, we solved magnetic structures both in the pristine $\text{Ba}_{1.2}\text{Mn}_8\text{O}_{16}$ sample and metal-substituted $\text{Ba}_{1.2}\text{CoMn}_7\text{O}_{16}$, to explain their vastly different magnetic properties.

The hollandite structure of $\text{Ba}_{1.2}\text{Mn}_8\text{O}_{16}$ can be described as a pseudo one-dimensional oxide, with the walls of the channels composed of edge-sharing MnO_6 octahedra (Fig. 1a). The Ba^{2+} cations are located and disordered within the channels of the hollandite, with their charge causing the mixed valence state of the Mn cations. One of the interesting crystal geometries within hollandite is that each wall of the square channel is made of a triangular ladder as shown in Figure 1b. A consequence of this topology is that magnetic frustration is likely as in the case of the infinite sheets of edge-sharing MnO_6 octahedra in the related compound $\alpha\text{-NaMnO}_2$.

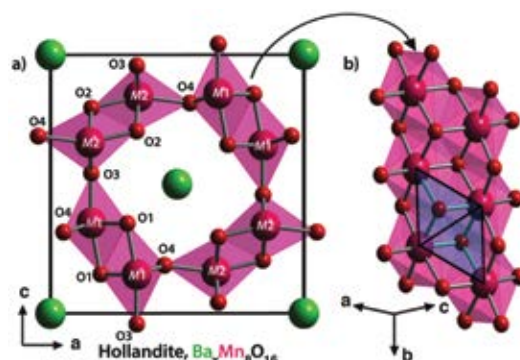


FIGURE 1: a) Unit cell of the hollandite and b) a different perspective down one of the walls of the Mn oxide framework demonstrating the triangular connectivity of the Mn centers.

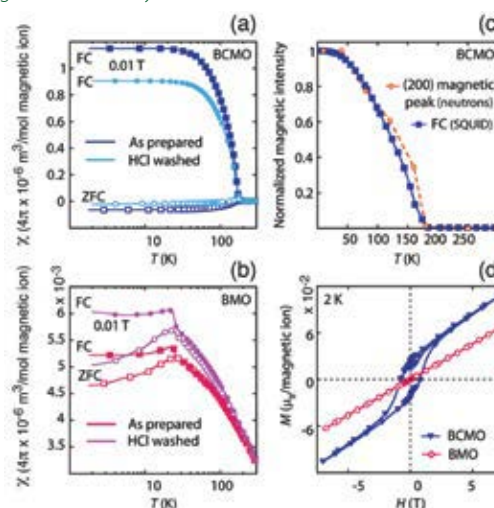


FIGURE 2: The magnetization versus temperature for a) $\text{Ba}_{1.2}\text{CoMn}_7\text{O}_{16}$ (BCMO) and b) $\text{Ba}_{1.2}\text{CoMn}_8\text{O}_{16}$ (BMO) c) Integrated intensity of the (200) reflection from neutron powder diffraction versus the magnetization from SQUID magnetometry d) Magnetization versus field in both oxides.

We prepared powder samples of $\text{Ba}_{1.2}\text{Mn}_8\text{O}_{16}$ and $\text{Ba}_{1.2}\text{Mn}_7\text{O}_{16}$ through a salt flux technique that led to phase pure materials, and we measured the magnetization versus temperature of both oxides. We noticed a remarkable difference in their behavior. While $\text{Ba}_{1.2}\text{Mn}_8\text{O}_{16}$ appears to be an antiferromagnet with a Néel temperature (T_N) of 25 K, the Co-substituted analogue displays a magnetization that diverges upon lowering the temperature below

¹University of Maryland, College Park, MD 20742

²Lujan Neutron Scattering Center, Los Alamos National Laboratory, Los Alamos, NM 87545

³NIST Center for Neutron Research, National Institute of Standards and Technology, Gaithersburg, MD 20899

⁴University of Delaware, Newark, DE 19716

180 K (T_C) (Fig. 2a, 2b); therefore, $\text{Ba}_{1.2}\text{Mn}_7\text{O}_{16}$ appears to be ferromagnetic. The magnetization vs. field of both compounds confirms that the compound $\text{Ba}_{1.2}\text{Mn}_7\text{O}_{16}$ displays hysteresis while $\text{Ba}_{1.2}\text{Mn}_8\text{O}_{16}$ remains antiferromagnetic up to 7 T (Fig. 2d). Curie-Weiss fits to the high temperature data of the magnetic susceptibilities also reveal an interesting dynamic. In $\text{Ba}_{1.2}\text{Mn}_8\text{O}_{16}$, the Curie-Weiss temperature θ_{CW} was found to be -430 K, while that in $\text{Ba}_{1.2}\text{Mn}_7\text{O}_{16}$ was -630 K. The much higher ordering temperature in $\text{Ba}_{1.2}\text{Mn}_7\text{O}_{16}$ indicates that the frustration index ($\theta_{CW}/T_{\text{transition}}$) is higher in $\text{Ba}_{1.2}\text{Mn}_8\text{O}_{16}$ (≈ 17) than in $\text{Ba}_{1.2}\text{Mn}_7\text{O}_{16}$ (≈ 3.5).

While magnetization studies with the SQUID magnetometer gave us a picture of the overall bulk properties, neutron diffraction was necessary to elucidate the distribution and orientation of the magnetic moments. The temperature dependent experiments were carried out on the BT-1 high-resolution powder diffractometer to determine the nuclear and magnetic structures of both compounds. In $\text{Ba}_{1.2}\text{Mn}_8\text{O}_{16}$, it is obvious that a complex antiferromagnetic structure develops as evidenced by the low angle superlattice peaks (Fig. 3). Through the method of representational analysis, we were able to fit the Bragg peaks with a complex structure that can be described as a helix with a large magnetic unit cell.

Upon inserting Co into the Mn oxide framework, the low-angle satellite peaks in the neutron powder pattern disappear. Instead, a new intensity is found at the (200) reflection, and the temperature dependence of this peak follows the SQUID magnetization data (Fig. 2c). Solving the structure utilizing the method of representational analysis indicates that the magnetic moment points mostly along the c -direction of the crystal, and slight canting of the moments off the (200) planes are what lead to the ferrimagnetism in this material.

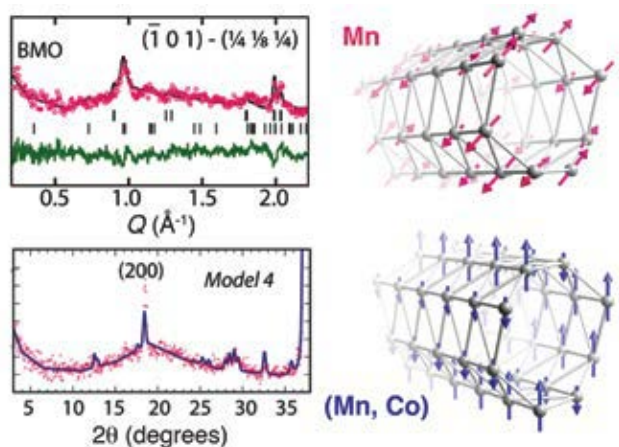


FIGURE 3: The magnetic Bragg peaks and resulting magnetic structure for (top) $\text{Ba}_{1.2}\text{CoMn}_8\text{O}_{16}$, and (bottom) $\text{Ba}_{1.2}\text{CoMn}_7\text{O}_{16}$.

The crystallographic information from neutron diffraction data provided us with some clues as to why this dramatic change in the magnetic properties occurs. The nature of many exchange interactions in metal oxides is mediated through the 2p orbitals of O, and such interactions should be highly antiferromagnetic when the Mn–O–Mn bond angle reaches 180° . For a bond angle of 90° , the exchange interaction is expected to be weakly ferromagnetic. The bond angles in our hollandite compounds range from 92.028° and 128.088° , which implies that both kinds of interactions may be present in the hollandites. We anticipate three exchange constants (J_1 , J_2 , and J_3) to be the dominating parameters controlling the overall magnetic behavior based on the connectivity of the Mn cations (Fig. 1a, 1b). Indeed, the recent theory work of Mandal *et al.* found that a J_1 , J_2 , and J_3 model predicts a rich phase diagram for the hollandite-type $\alpha\text{-MnO}_2$, including ferromagnetism and helical antiferromagnetism [5].

In summary, we have found a new functional Mn oxide system where we can control the overall magnetic behavior through chemical substitution. In $\text{Ba}_{1.2}\text{Mn}_8\text{O}_{16}$ the complex helical antiferromagnetism gives way to a ferrimagnetic oxide upon substitution of Mn sites with Co cations. The high level of magnetic frustration in $\text{Ba}_{1.2}\text{Mn}_8\text{O}_{16}$ is relieved in $\text{Ba}_{1.2}\text{Mn}_7\text{O}_{16}$ by having Co^{2+} substitute in the framework enough so that all the $\text{Mn}^{3.8+}$ changes to Mn^{4+} . The result is a ferrimagnetic structure that consists of a mostly collinear antiferromagnetic structure with some slight canting of the moments. By reducing the frustration in the magnetic lattice, the temperature of transition is also vastly changed, with a $T_N = 25$ K in $\text{Ba}_{1.2}\text{Mn}_8\text{O}_{16}$ going to $T_C = 180$ K in $\text{Ba}_{1.2}\text{Mn}_7\text{O}_{16}$. We propose that a J_1 - J_2 - J_3 model for the magnetic exchange interactions would be useful in designing new magnetic materials based on the Mn oxides with the hollandite structure. As demonstrated with the mixed valence manganites before, the use of neutron diffraction is an indispensable tool in exploring new structure types such as these hollandites and elucidating their magnetic properties.

References

- [1] M. M. Thackeray, *Prog. Solid State Ch.* **25**, 1 (1997).
- [2] A. P. Ramirez, *J. Phys. Condens. Matter* **9**, 8171 (1997).
- [3] J. B. Goodenough, *Prog. Solid State Ch.* **5**, 145 (1971).
- [4] A. M. Larson, P. Moetakef, K. Gaskell, C. M. Brown, G. King, E. E. Rodriguez, *Chem. Mater.* **27**, 1901 (2015).
- [5] S. Mandal, A. Andreanov, Y. Crespo, N. Seriani, *Phys. Rev. B* **90**, 104420 (2014).

New metal–organic framework exhibiting increased charge density and enhanced H₂ binding

M. R. Hudson¹, M. T. Kapelowski², S. J. Geier², D. Stück², J. A. Mason², J. N. Nelson³, D. J. Xiao², Z. Hulvey^{1,4}, E. Gilmour³, S. A. FitzGerald³, M. Head-Gordon^{2,5}, C. M. Brown^{1,6}, and J. R. Long^{2,7}

Metal-organic frameworks (MOFs) are a class of porous materials whose properties can be tuned for specific applications, such as storing and separating gases, by choice of the component inorganic units and bridging organic linkers. Strong adsorption sites are installed on the pore surface, such as exposed metal cations, in order to selectively attract specific gas molecules [1-3]. The MOF $M_2(\text{dobdc})$ ($M = \text{Mg, Mn, Fe, Co, Ni, Cu, Zn}$; $\text{dobdc}^{4-} = 2,5\text{-dioxido-1,4-benzenedicarboxylate}$) structure type contains a high density of exposed metal cations, primary binding sites for small gas molecules, and have been investigated for potential applications, including H₂ and CH₄ storage, CO₂ capture, and CO separations [1-4]. Discovering new frameworks is not trivial, but selectively tuning the most promising existing MOFs by altering the linker, the metal, or both provides a viable strategy for developing new adsorbents. We have tuned the electronics of the exposed metal cations $M_2(\text{dobdc})$, and thus its affinity for gas molecules, by synthesizing a structural isomer of the $M_2(\text{dobdc})$ framework, $M_2(m\text{-dobdc})$ ($M = \text{Mg, Mn, Fe, Co, or Ni}$), where the *para* carboxylic acid functionalities and *para* hydroxyl substituents, are replaced with their *meta* counterparts. The new framework has subtle differences in the electronic structure of the ligand and overall connectivity as compared to the $M_2(\text{dobdc})$ framework. Isomers of MOFs are known and primarily derive from what are termed “framework isomers.” The structure of $M_2(m\text{-dobdc})$, however, is an example of a ligand-originated isomer. This framework’s gas separation properties are probed using H₂ adsorption, as H₂ is simple, has low polarizability, and has potential use as a clean fuel.

Powder X-ray and neutron diffraction methods were used to solve the crystal structure of $\text{Co}_2(m\text{-dobdc})$ confirming that the $M_2(m\text{-dobdc})$ frameworks are indeed structurally analogous to $M_2(\text{dobdc})$ (Fig. 1). Similar to $\text{Co}_2(\text{dobdc})$, $\text{Co}_2(m\text{-dobdc})$ possesses helical chains of Co²⁺ centers running parallel to the crystallographic *c* axis. Based on the change in point group symmetry of the linker from C_{2h} in

$\text{H}_4(\text{dobdc})$ to C_{2v} in $\text{H}_4(m\text{-dobdc})$, a change in the space group from $R\bar{3}$ in $\text{Co}_2(\text{dobdc})$ to $R3m$ in $\text{Co}_2(m\text{-dobdc})$ is observed. The orientation of the carboxylate groups of the linker is changed, with the CO₂⁻ unit twisting out of the plane of the aromatic ring by approximately 12.5° in $\text{Co}_2(m\text{-dobdc})$, as compared to just 3.5° in $\text{Co}_2(\text{dobdc})$. Metal centers in $\text{Co}_2(m\text{-dobdc})$ that face into the same pore align directly along the crystallographic *b* axis, resulting in a Co...Co separation of 14.9(1) Å across the channels. In $\text{Co}_2(\text{dobdc})$, the metals are offset from each other by one-third of a twist in the chain, leading to a Co...Co separation of 15.24(8) Å [1].

Low-pressure H₂ adsorption isotherms were measured for the four $M_2(m\text{-dobdc})$ frameworks at 77 K to probe the potentially modified electronic structures at the open metal sites. Although the $M_2(\text{dobdc})$ MOFs have a higher H₂ uptake at 1 bar, at very low pressures, $\text{Ni}_2(m\text{-dobdc})$ has a significantly higher uptake than $\text{Ni}_2(\text{dobdc})$ indicating that the interaction of H₂ with the exposed Ni²⁺ cations on the surface of $\text{Ni}_2(m\text{-dobdc})$ is stronger than in $\text{Ni}_2(\text{dobdc})$, the best in the series. Similar to $M_2(\text{dobdc})$, the isosteric heat of

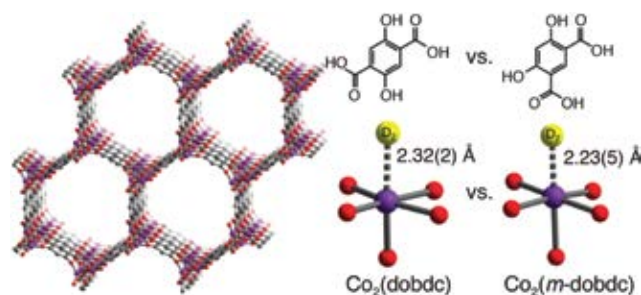


FIGURE 1: (Left) Crystal structure of $\text{Co}_2(m\text{-dobdc})$ showing 1-D hexagonal pores and helical metal chains. (Right) Partial crystal structures of $\text{Co}_2(\text{dobdc})$ vs. $\text{Co}_2(m\text{-dobdc})$ showing the primary D₂ binding site I (yellow).

adsorption plots for $M_2(m\text{-dobdc})$ imply a nearly constant H₂ binding enthalpy until a loading of (0.7 to 0.8) H₂/M²⁺ (H₂ per open metal) followed by a sharp decrease as all exposed metal cations become occupied and only weaker adsorption sites remain [1]. Increasing the binding

¹NIST Center for Neutron Research, National Institute of Standards and Technology, Gaithersburg, MD 20899

²University of California, Berkeley, CA 94720

³Oberlin College, Oberlin, OH 44074

⁴University of Maryland, College Park, MD 20742

⁵Chemical Sciences Division, Lawrence Berkeley National Laboratory, Berkeley, CA 94720

⁶University of Delaware, Newark, DE 19716

⁷Materials Sciences Division, Lawrence Berkeley National Laboratory, Berkeley, CA 94720

enthalpy of H₂ in MOFs is important, as a binding enthalpy of (–15 to –20) kJ/mol is predicted to be optimal for the on-board storage of H₂ at ambient temperatures. The low-coverage isosteric heats of adsorption of *M*₂(*m*-dobdc) are –10.3 kJ/mol (Mn²⁺), –11.1 kJ/mol (Fe²⁺), –11.6 kJ/mol (Co²⁺), and –12.3 kJ/mol (Ni²⁺). The trend further mirrors that observed for H₂ binding within *M*₂(dobdc) and are, on average, ≈ 1.0 kJ/mol stronger than in the corresponding *M*₂(dobdc) [1,4].

In-situ powder neutron diffraction experiments were performed by dosing precise quantities of D₂ to determine the reason for the higher H₂ binding enthalpy seen in the *M*₂(*m*-dobdc) MOFs. It was anticipated that the open metal site would provide the primary H₂ binding site (I) and at a loading 0.75 D₂/Co²⁺ in Co₂(*m*-dobdc), this is the case with D₂···M²⁺ distance of 2.23(5) Å, closer than 2.32(2) Å in Co₂(dobdc), confirming that the H₂ binds more strongly to the open metal sites within the meta (Fig. 1) [1]. At a loading of 1.25 D₂/M²⁺, a second binding site (II) adjacent to the primary site becomes populated (Fig. 2). This can be attributed to a D₂···D₂ interaction (2.88(4) Å) combined with a D₂···O (3.28(6) Å) from the nearest framework oxygen atom. Site II is in a similar location to the secondary binding sites observed in Co₂(dobdc). The site I to site II D₂···D₂, 3.05(2) Å, in Co₂(*m*-dobdc) at a loading of 2.25 D₂/M²⁺ is significantly shorter than the 3.16(2) Å observed in Co₂(dobdc). This closer site I to site II separation in Co₂(*m*-dobdc) is most likely a polarization effect. A third binding site (III) located ≈ 3.08 Å above the mean plane of the aromatic ring of the *m*-dobdc⁴⁻ linker becomes populated at higher loadings of D₂ (Fig. 2). This site is equidistant (3.25(6) Å) to two D₂ at neighboring site I positions in Co₂(*m*-dobdc), whereas in Co₂(dobdc), the different symmetry leads to two distinct site I···site III interactions at distances of 3.06(3) and 3.24(3) Å. Importantly, for Co₂(*m*-dobdc) there are only half as many D₂ situated at site III as in Co₂(dobdc) at high loadings, which leads to the observation of a fourth binding site (IV) not seen in the *M*₂(dobdc) series (Fig. 2). The differing symmetry of the *meta* framework contributes to this additional binding site, as the two framework O atoms interacting with the D₂ molecule in site IV are equivalent in Co₂(*m*-dobdc), but not in Co₂(dobdc).

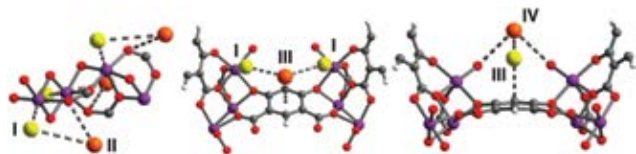


FIGURE 2: Partial crystal structures of Co₂(*m*-dobdc) showing the interactions of the primary (I) and secondary D₂ binding sites II, III, and IV (yellow, orange spheres). Purple gray, red, and white spheres: Co, C, O, H, respectively.

Inelastic neutron scattering (INS) experiments were carried out to probe the site-specific binding properties of H₂ (Fig. 3). At loadings up to 1.0 n-H₂/M²⁺, two low-energy rotational lines are apparent at 7.8(1) meV and 9.5(1) meV for Co₂(*m*-dobdc) and 7.5(1) meV and 9.3(1) meV for Ni₂(*m*-dobdc). These features are similar to those observed in INS spectra for several compounds in the *M*₂(dobdc) series and have been assigned to transitions occurring from the *J* = 0 state to sublevels of the split *J* = 1 rotational state for initial H₂ molecules adsorbed at the metal centers [4]. The position of the first peak is at higher energies and the position of the second peak is at lower energies than is observed for all the *M*₂(dobdc) compounds. The energy splitting of these peaks has been previously shown to have no correlation with the binding strength of H₂ at the open metal site. At loadings above 0.75 n-H₂/M²⁺, as sites II–IV populate, the additional H₂ molecules affect the rotational potential for H₂ molecules at site I, adjusting the rotational energy level and resulting in the two peaks shifting.

These results demonstrate the synthesis of a new family of MOFs, *M*₂(*m*-dobdc), representing a potentially less expensive version of their well-known structural isomers *M*₂(dobdc). Future efforts will focus on determining whether the enhanced charge density at the metal sites leads to improvements compared to their *M*₂(dobdc) analogues in the efficacy of key gas separations.

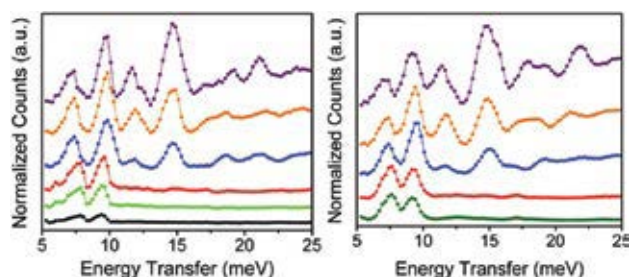


FIGURE 3: Background subtracted INS data for Co₂(*m*-dobdc) (left) and Ni₂(*m*-dobdc) (right) at loadings of 0.33 (black), 0.50 (dark green), 0.67 (light green), 1.0 (red), 2.0 (blue), 3.0 (yellow), and 4.0 (purple) n-H₂ molecules per metal atom (offset for clarity).

References

- [1] M. T. Kapelewski, *et al.*, J. Am. Chem. Soc. **136**, 12119 (2014).
- [2] W. L. Queen, M. R. Hudson, *et al.*, Chem. Sci. **5**, 4569 (2014).
- [3] E.D. Bloch, M. R. Hudson, *et al.*, J. Am. Chem. Soc. **136**, 10752, (2014).
- [4] W. L. Queen, *et al.*, Dalton Trans. **41**, 4180 (2012).

Structural behavior, dynamics, and superionic conduction in $\text{Na}_2\text{B}_{10}\text{H}_{10}$

T. J. Udovic¹, W. S. Tang^{1,2}, H. Wu¹, W. Zhou¹, J. J. Rush^{1,2}, A. V. Skripov³, A. V. Soloninin³, R. V. Skoryunov³, O. A. Babanova³, V. Stavila⁴, M. Matsuo⁵, A. Unemoto⁵, and S. Orimo⁵



Recently, we found that $\text{Na}_2\text{B}_{12}\text{H}_{12}$, which possesses large icosahedral $\text{B}_{12}\text{H}_{12}^{2-}$ anions, undergoes an order-disorder phase transition [1] near 529 K accompanied by superionic conductivity ($\approx 0.1 \text{ S cm}^{-1}$) [2] rivaling that of other favored materials currently of interest for use in Na-ion batteries. These types of large polyhedral anion-based compounds represent an intriguing new area for discovering other materials with similar superionic conductivities, but with lower transition temperatures.

One such material is the related sodium salt, $\text{Na}_2\text{B}_{10}\text{H}_{10}$, which contains large, ellipsoidal-shaped $\text{B}_{10}\text{H}_{10}^{2-}$ anions. Our differential scanning calorimetry measurements indicated a much lower order-disorder transition near 360 K [3]. Neutron powder diffraction (NPD) measurements [4] on the BT-1 High-resolution Powder Diffractometer of an isotopically-tailored $\text{Na}_2^{11}\text{B}_{10}\text{D}_{10}$ sample (see Fig. 1), we were able to correct the previously inaccurate low- T ordered monoclinic $P2_1/c$ structure derived from X-ray powder diffraction (XRPD). Our NPD-derived structure was verified to be the lower-energy configuration by density-functional-theory (DFT) calculations. Moreover, the DFT-simulated phonon density of states for this structure was found to be consistent with the observed neutron vibrational spectra measured on the Filter-Analyzer Neutron spectrometer for both $\text{Na}_2^{11}\text{B}_{10}\text{D}_{10}$ and $\text{Na}_2^{11}\text{B}_{10}\text{H}_{10}$ (see Fig. 2).

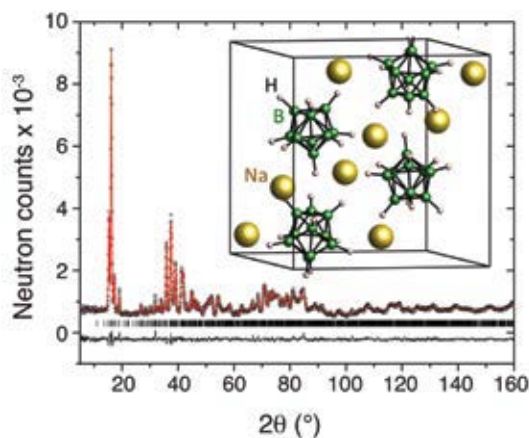


FIGURE 1: NPD data for $\text{Na}_2^{11}\text{B}_{10}\text{D}_{10}$ at 2.5 K with refinement results corresponding to the depicted ordered monoclinic structure. Yellow, green, and white spheres denote Na, B, and H, respectively.

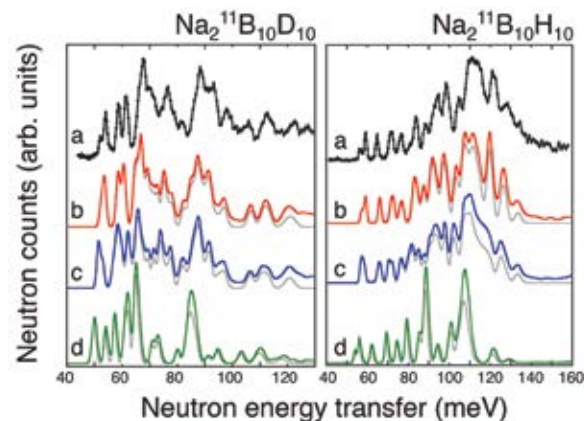


FIGURE 2: Neutron vibrational spectra for (a) $\text{Na}_2^{11}\text{B}_{10}\text{D}_{10}$ and $\text{Na}_2^{11}\text{B}_{10}\text{H}_{10}$ at 4 K compared to the simulated one-phonon (gray) and one+two-phonon densities of states (red, blue, and green) from first-principles phonon calculations of the different DFT-optimized structures: (b) NPD-derived structure, (c) previous XRPD-derived structure, and (d) “isolated” $^{11}\text{B}_{10}\text{D}_{10}^{2-}$ anions.

Further NPD measurements of $\text{Na}_2^{11}\text{B}_{10}\text{D}_{10}$ above the phase transition indicated the formation of a disordered, face-centered-cubic (fcc) phase, possessing a vacancy-rich Na^+ cation sublattice (see Fig. 3) [3,4]. Fourier difference maps suggested a broad distribution of cation positions, and the inclusion of three different interstitial positions was ultimately necessary to attain a good model fit. The refinements also suggested extensive anion orientational disorder, which could be represented in various ways via multiple B and H positions. The structure depicted in Fig. 3 reflects the simplest representation of six approximately superimposed anion orientations.

Anion dynamical behavior was probed by neutron fixed-window scans [3] of $\text{Na}_2^{11}\text{B}_{10}\text{H}_{10}$ on the High-Flux Backscattering Spectrometer. The results in Fig. 4 suggest that a dramatic change in $\text{B}_{10}\text{H}_{10}^{2-}$ anion reorientational mobility occurs upon phase transformation. In particular, the large elastic neutron counts in the low- T ordered phase suggest anion reorientational jump frequencies less than 10^8 s^{-1} , whereas the roughly 80 % lower counts in the high- T disordered phase suggest an orders-of-

¹NIST Center for Neutron Research, National Institute of Standards and Technology, Gaithersburg, MD 20899

²Department of Materials Science and Engineering, University of Maryland, College Park, MD 20742

³Institute of Metal Physics, Ural Branch of the Russian Academy of Sciences, Ekaterinburg, Russia

⁴Energy Nanomaterials, Sandia National Laboratories, Livermore, CA 94551

⁵Institute for Materials Research, Tohoku University, Sendai, Japan

magnitude enhancement to greater than 10^{10} s^{-1} . The Fig. 4 inset of a quasielastic neutron scattering (QENS) spectrum [3] measured on the Disk-Chopper Spectrometer for the disordered phase at 375 K indicates a quasielastic component with a Lorentzian linewidth of about $41(1) \text{ } \mu\text{eV}$ FWHM, which reflects a jump correlation frequency on the order of $3 \times 10^{10} \text{ s}^{-1}$. The ratio of elastic and total scattering intensities (i.e., elastic incoherent structure factor) suggests that, besides $\text{B}_{10}\text{H}_{10}^{2-}$ reorientational jumps around the long axis, anion flips leading to exchanges of apical H atom positions are also occurring.

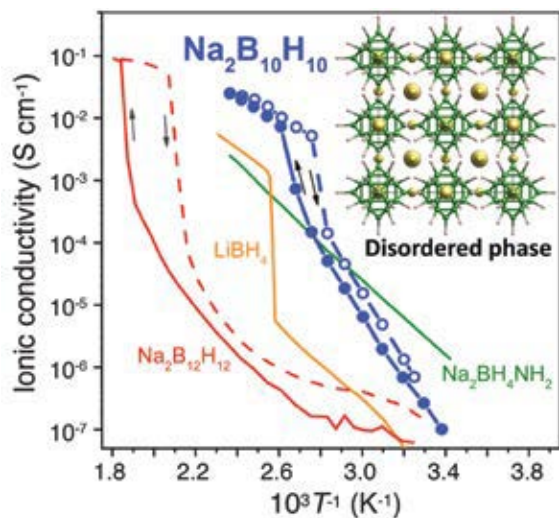


FIGURE 3: Temperature dependence of the ionic conductivity of $\text{Na}_2\text{B}_{10}\text{H}_{10}$ compared with that for other complex hydride materials (see Refs. in [4]). Inset shows the high- T disordered fcc structure.

We probed the Na^+ dynamical behavior in $\text{Na}_2\text{B}_{10}\text{H}_{10}$ by ^{23}Na NMR measurements [3], which confirmed that the transition from the ordered to the disordered phase is accompanied by a sharp rise in the Na^+ translational jump rate to $>1.5 \times 10^8 \text{ s}^{-1}$ and a large drop in the activation energy from 750(20) meV to 190(10) meV. Moreover, the very small ^{23}Na NMR linewidth (0.2 kHz FWHM) observed in the disordered phase confirmed that Na^+ cations were undergoing long-range diffusion.

Finally, we characterized the ionic conduction behavior of $\text{Na}_2\text{B}_{10}\text{H}_{10}$ by ac impedance measurements [3]. Figure 3 indicates conductivity ($\approx 0.01 \text{ S cm}^{-1}$) above the hysteretic transition unmatched by any other known complex hydride materials. This superionic conductivity is consistent with the relatively small activation energy for Na^+ diffusion within the liquid-like cation sublattice. Again, similar to disordered $\text{Na}_2\text{B}_{12}\text{H}_{12}$, [2] the overly large size and quasispherical shape

of the polyhedral anions probably result in less restrictive interstitial pathways and, hence, reduced Na^+ diffusional bottlenecks between the various cation sites within the close-packed anion sublattice.

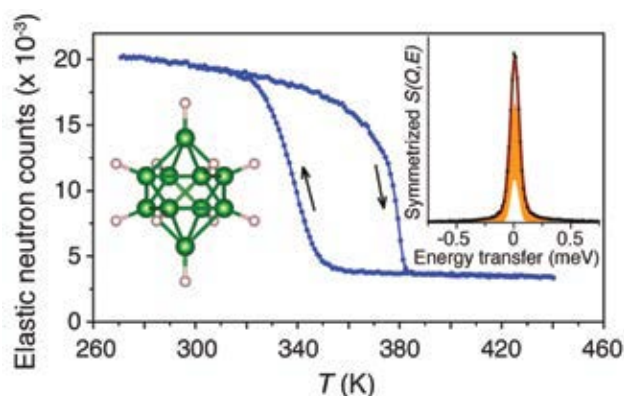


FIGURE 4: Neutron elastic-scattering fixed-window scan at $0.8 \text{ } \mu\text{eV}$ (FWHM) instrumental resolution for $\text{Na}_2^{11}\text{B}_{10}\text{H}_{10}$ upon heating and cooling at 0.25 K min^{-1} , at a neutron momentum transfer Q of $0.87 \text{ } \text{\AA}^{-1}$. The right inset shows a quasielastic scattering spectrum at 375 K at the same Q value, at $79 \text{ } \mu\text{eV}$ (FWHM) instrumental resolution. The fit (red) to the data (black) is comprised of elastic (white) and quasielastic (orange) contributions. The left inset depicts the $\text{B}_{10}\text{H}_{10}^{2-}$ anion.

As for other disordered complex hydrides, the reorientationally mobile anions associated with superionic $\text{Na}_2\text{B}_{10}\text{H}_{10}$ may also lower the cation diffusional barrier by providing a dynamically cooperative environment for cation jumps within the interstitial space formed by the anion sublattice. At least an order-of-magnitude higher anion reorientational jump rate compared to the Na^+ diffusional jump rate may enable the anions to act in some sense as 'lubricants' for cation diffusive motions. For all these disordered materials, a more theoretical grasp of the relationship of structural disorder and anion reorientational mobility to cation diffusion and conductivity awaits future first-principles molecular dynamics calculations.

References

- [1] N. Verdal, J.-H. Her, V. Stavila, A. V. Soloninin, O. A. Babanova, A. V. Skripov, T. J. Udovic, J. J. Rush, *J. Sol. State Chem.* **212**, 81 (2014).
- [2] T. J. Udovic, M. Matsuo, A. Unemoto, N. Verdal, V. Stavila, A. V. Skripov, J. J. Rush, H. Takamura, S. Orimo, *Chem. Comm.* **50**, 3750 (2014).
- [3] T. J. Udovic, M. Matsuo, W. S. Tang, H. Wu, V. Stavila, A. V. Soloninin, R. V. Skoryunov, O. A. Babanova, A. V. Skripov, J. J. Rush, A. Unemoto, H. Takamura, S. Orimo, *Adv. Mater.* **26**, 7622 (2014).
- [4] H. Wu, W. S. Tang, W. Zhou, V. Stavila, J. J. Rush, T. J. Udovic, *Cryst. Eng. Comm.* **17**, 3533 (2015).

Magnetic scattering and vortex lattice in an iron-based ferromagnetic superconductor

J. W. Lynn¹, X. Zhou², C. K. H. Borg², S. R. Saha³, J. Paglione³, and E. E. Rodriguez²



The magnetic properties of superconductors have a rich and interesting history. Early work showed that even tiny concentrations of magnetic impurities destroyed the superconducting pairing through the exchange-driven spin depairing mechanism, prohibiting any possibility of cooperative magnetic behavior [1]. The first exception to this rule was provided by the cubic rare-earth substituted CeRu_2 alloys, followed by the ternary Chevrel-phase (RMO_6S_8 , R = rare earth) and related superconductors, where the first demonstrations of long-range magnetic order coexisting with superconductivity were obtained. The majority of these Chevrel-phase materials order antiferromagnetically where coexistence of long-range order with superconductivity is common, but these materials also provided the first examples of the rare occurrence of ferromagnetism and consequent electromagnetic competition with superconductivity. Antiferromagnetic order is also found for the Cu spins and all the rare earths in the cuprates, and for all the $\text{RNi}_2\text{B}_2\text{C}$ borocarbides with the singular exception of $\text{ErNi}_2\text{B}_2\text{C}$ at low temperature (below 2.3 K) where a net magnetization developed that resulted in the spontaneous formation of flux quanta (vortices).

For the high- T_c iron-based superconductors of direct interest here, all the iron and rare-earth orderings have been antiferromagnetic in nature until very recently, with the apparent development of 3d iron ferromagnetism around 10 K in the form of spontaneous vortex creation in $(\text{Li}_{1-x}\text{Fe}_x\text{OH})\text{FeSe}$, well below the superconducting transition temperature T_c which can be as high as 43 K. To investigate both the magnetic and superconducting properties of this system, we have carried out neutron diffraction and small-angle neutron scattering (SANS) measurements on a polycrystalline sample $(^7\text{Li}_{0.82}\text{Fe}_{0.18}\text{OD})\text{FeSe}$, where the ^7Li isotope has been employed to avoid the neutron absorption of ^6Li , and H has been replaced by D to avoid the huge nuclear incoherent cross section [2].

High intensity powder diffraction measurements were carried out to search for magnetic Bragg peaks. For the present system no evidence for magnetic ordering

was found. This perhaps is not surprising given that the ferromagnetism is expected to arise in the Li-Fe layer; with an expected moment of less than $1 \mu_B/\text{Fe}$ and only 18 % of the sites occupied, the site-averaged ferromagnetic moment will be very difficult to observe in powder diffraction.

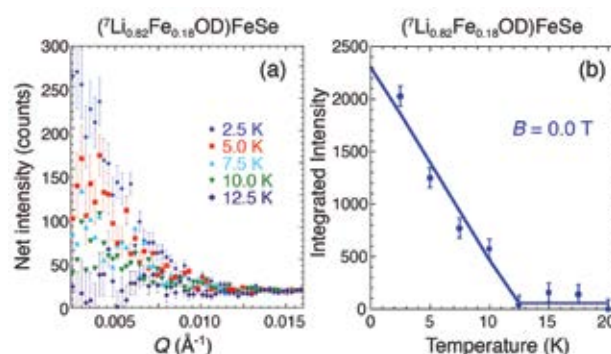


FIGURE 1: (a) Magnetic scattering as a function of wave vector Q for several temperatures. No magnetic field is applied. At 12.5 K very little magnetic scattering is observed, as is the case at higher temperatures (see text). Below the ferromagnetic transition magnetic scattering intensity develops, which increases monotonically with both decreasing Q and T . No peak in this Q range is observed, ruling out the formation of a long range ordered oscillatory magnetic state. (b) Integrated intensity as a function of temperature, revealing a magnetic transition temperature of ≈ 12.5 K. Uncertainties are statistical in origin and represent one standard deviation.

To detect long wavelength oscillatory magnetic order, pure ferromagnetism, and study the vortex scattering, small-angle neutron scattering (SANS) is the technique of choice. We have observed two separate components of magnetic scattering, one in zero applied field due to an inhomogeneous mixed state originating from either the spontaneous formation of vortices or ferromagnetic domains, while in an applied field we observe the scattering from a well-developed vortex lattice that arises below the superconducting transition temperature for this sample of $T_c = 18$ K [2]. Figure 1a shows the wave vector dependence of the difference scattering in this regime at several temperatures of interest, with data being taken between 2.5 K and 37.5 K in steps of 2.5 K. At and above 12.5 K no magnetic signal is observed, while for lower

¹NIST Center for Neutron Research, National Institute of Standards and Technology, Gaithersburg, MD 20899

²Department of Chemistry and Biochemistry, University of Maryland, College Park, MD 20742

³Department of Physics, University of Maryland, College Park, MD 20742

temperatures we observe a rapid increase in intensity with decreasing T . At each temperature this scattering increases monotonically with decreasing Q but otherwise does not appear to change its shape. We see that there is a well-defined onset of scattering at the onset of ferromagnetism at ≈ 12 K, which could originate from the spontaneous formation of vortices. They will be oriented randomly in the powder and most won't coherently Bragg diffract, but individual vortices will scatter and is likely the origin of the SANS scattering shown in Fig. 1.

SANS measurements in a horizontal applied magnetic field are shown in Fig. 2. Figure 2a shows the net intensity at 5 K upon cooling in a field of 0.4 T. In comparison with the data in Fig. 1a, we see that the smallest Q ferromagnetic scattering has reduced in intensity as expected since in this layered superconductor only some of the spontaneous vortices will align with the field. We also see a well-defined peak at larger Q . A least-squares fit to a (resolution-limited) Gaussian peak yields a position $Q = 0.0078(3) \text{ \AA}^{-1}$. The expected position for a triangular vortex lattice is given by

$$Q_{10} = 2\pi \sqrt{\frac{2B}{(\sqrt{3})\phi_0}}$$

where $\phi_0 = 2.068 \times 10^5 \text{ T \AA}^2$ is the flux quantum and B is the internal field. For an applied field of 0.4 T the calculated position is $Q = 0.0077 \text{ \AA}^{-1}$, which is in excellent agreement with the measurement.

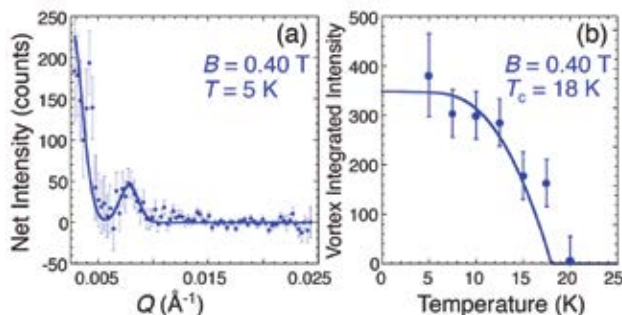


FIGURE 2: (a) Magnetic intensity at 5 K after cooling from 25 K in an applied field of 0.4 T. The ferromagnetic scattering has shifted to smaller Q , indicating that the length scale has increased or the strength for this scattering has decreased as would be expected when a field is applied. The peak at $Q = 0.0077 \text{ \AA}^{-1}$ is due to the vortex lattice. (b) Integrated intensity of the vortex scattering as a function of temperature. The onset of scattering occurs at $T_c = 18$ K. No evidence of the ferromagnetic ordering is observed, indicating that the ordered moment is small (see text).

The temperature dependence of the vortex scattering, determined by integrating the net scattering over the peak is shown in Fig. 2b, develops a signal below T_c as expected. In the ferromagnetic state we expect an additional contribution from the internally generated magnetic flux, which would shift the vortex peak to larger Q , and increase its intensity. Neither trend is observed in these data, again indicating that the ferromagnetic moment is quite small.

For ferromagnetic superconductors like ErRh_4B_4 , HoMo_6S_8 and HoMo_6Se_8 the magnetization that develops in the superconducting state competes with the Meissner screening through the London penetration depth. This competition results in a long wavelength oscillatory magnetic order that coexists with superconductivity, with a wavelength that is either strongly temperature dependent, or results in a strongly first-order transition to pure ferromagnetism where the superconductivity is destroyed. The present system certainly behaves differently in that we do not see any oscillatory magnetic order, thus leaving the other possibility that vortices spontaneously form. In a polycrystalline sample the vortices will be randomly oriented and it is very unlikely that a spontaneous vortex lattice could ever be observed, and indeed a true spontaneous vortex lattice—formed in the absence of an applied field—still remains to be observed in any ferromagnetic superconductor. Efforts to observe this will require single crystal samples, and such measurements are underway. What is clear is that $\text{Li}_{1-x}\text{Fe}_x\text{OHFeSe}$ is a fascinating ferromagnetic superconductor, and further measurements to investigate the magnetic order, spin fluctuations, lattice dynamics, and vortex structure in greater detail should prove very interesting.

References

- [1] Neutron Scattering Studies of Magnetic Ordering in Ternary Superconductors, W. Thomlinson, J. W. Lynn, G. Shirane and D. Moncton, in *Superconductivity in Ternary Compounds*, ed. by M. B. Maple and Ø. Fischer, "Topics in Current Physics", Vol. 34, Chap. 8, (Springer-Verlag, New York, 1982).
- [2] J. W. Lynn, X. Zhou, C. K. H. Borg, S. R. Saha, J. Paglione, E. E. Rodriguez, Phys. Rev. B **92**, 060510(R) (2015).

Static and dynamic short-range order in a frustrated magnet with exchange disorder

K. A. Ross^{1,2,3}, J. W. Krizan⁴, J. A. Rodriguez-Rivera^{2,5}, R. J. Cava⁴, and C. L. Broholm^{1,2,6}



Built from corner-sharing tetrahedra, the pyrochlore lattice hosts magnetic and electronic phases with local- rather than long-range orders. The attendant manifold of low energy states gives rise to unique physical properties and may support exotic quasi-particles such as magnetic monopoles, artificial photons, visons, and spinons.

While past attention has focused on pyrochlore oxides, Cava *et al.* recently discovered a new class of pyrochlore fluorides with enhanced energy scales, exchange anisotropies, and new opportunities for doping. The chemical formula is $AA'B_2F_7$, where integral valence and charge neutrality requires a split A-site with net charge 3^+ . This is accomplished in $Na^+Ca_2^{2+}Co^{2+}F_7$ where the corresponding cation disorder is expected to introduce weak, potentially correlated exchange disorder.

Our MACS experiment on single crystalline $NaCaCo_2F_7$ provides a first view of a new and surprising world of fluoride pyrochlore magnetism. Figure 1(a)-(c) shows the momentum dependence of magnetic scattering for different values of energy transfer. The data reflect the spatial correlations of spins in different energy regimes. Throughout the energy range probed there is no scattering near the origin of momentum space nor near the equivalent Γ -points (004) and (220). This constitutes experimental evidence that the dipole moment vanishes on every tetrahedron for time scales exceeding $\tau = \hbar/E$. At the lowest energies we see relatively sharp, though not resolution limited, magnetic peaks in a pattern that clearly identifies the short range order as being of the easy plane

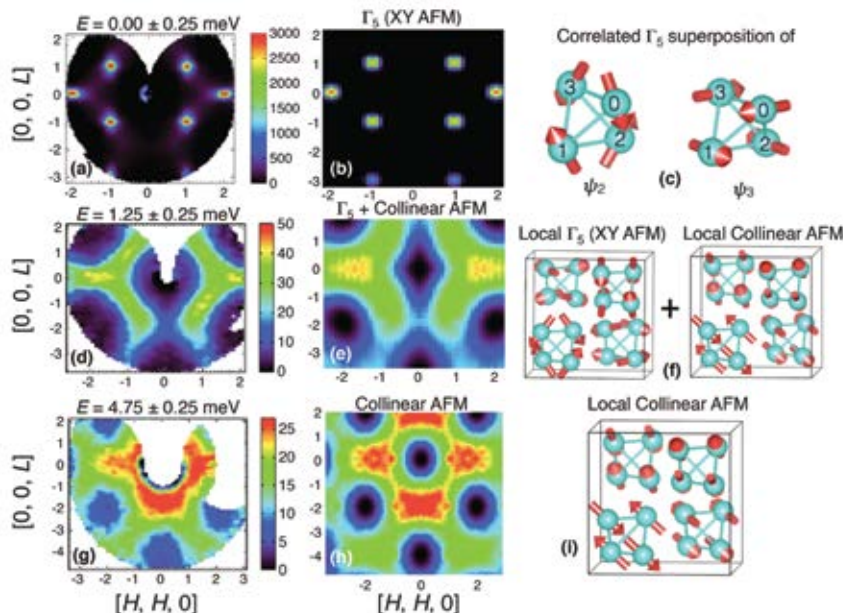


FIGURE 1: Elastic and inelastic magnetic neutron scattering from the pyrochlore fluoride $NaCaCo_2F_7$ measured on the MACS cold neutron spectrometer. Each row represents information at different energy transfer (0 meV, 1.25 meV, and 4.75 meV) that addresses spin correlations at progressively shorter time scales $\tau = \hbar/E$. (a), (d), and (g) show magnetic scattering data obtained after suitable background subtraction. (b), (e), and (f) show the calculated patterns of magnetic scattering associated with the spin configurations indicated in (c), (f), and (i).

variety described by the Γ_5 irreducible representation. The corresponding basis vectors that make up this state (denoted ψ_2 and ψ_3) are shown in Fig. 1(c) and the associated magnetic neutron scattering calculated for a correlation length $\xi \approx 16 \text{ \AA}$ is shown in Fig. 1(b).

Beyond the peaks, a diffuse pattern of scattering is also clearly visible in Fig. 1(a). The salient features of this scattering are consistent with easy plane antiferromagnetic tetrahedra without inter-tetrahedron correlations (Fig. 1(e)-(f)).

At higher energies (Fig. 1 (g)-(i)) the character of the scattering changes to a block-like form that is associated

¹Institute for Quantum Matter and Department of Physics and Astronomy, Johns Hopkins University, Baltimore, MD 21218

²NIST Center for Neutron Research, National Institute of Standards and Technology, Gaithersburg, MD 20899

³Colorado State University, Fort Collins, CO 80523

⁴Princeton University, Princeton, NJ 08544

⁵University of Maryland, College Park, MD 20742

⁶Department of Materials Science and Engineering, Johns Hopkins University, Baltimore, MD 21218

with uniaxial antiferromagnetic spin correlations on uncorrelated tetrahedra. Fig. 2 shows the coupled momentum and energy dependence of the magnetic scattering. The signal near (002), which is associated with a uniaxial antiferromagnetic arrangement of spins on tetrahedra, appears as a broad spectral maximum that is peaked at $E = 5$ meV. This heavily damped mode represents the lowest energy excitation that violates the easy plane character of the system while retaining antiferromagnetic correlations.

While the elastic magnetic scattering in Fig. 1(a) develops at a freezing transition for $T < T_f = 15$ K, there is no marked

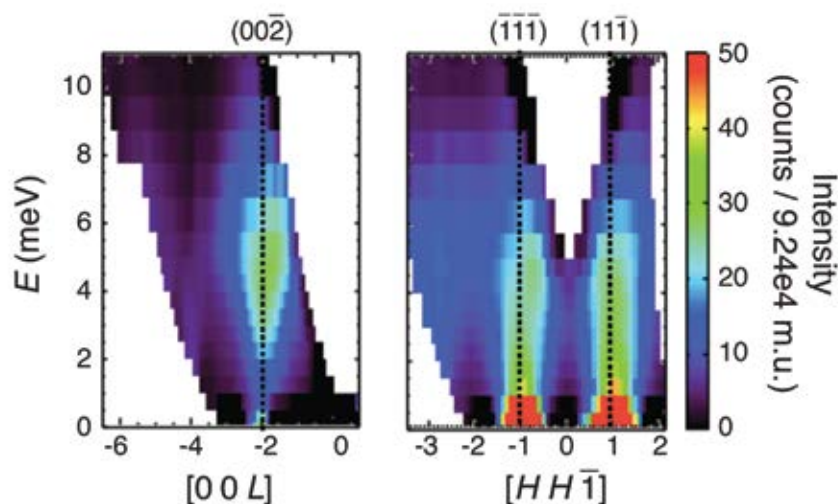


FIGURE 2: Momentum-energy transfer dependence of inelastic magnetic scattering from single crystalline $\text{NaCaCo}_2\text{F}_7$ acquired on MACS. While scattering extends to the quasi-elastic line at the (111) type antiferromagnetic quasi-Bragg points, a finite energy transfer is associated with collinear spin excitations that give rise to scattering at (002).

evolution of the spin correlation length at this transition. The quasi-elastic scattering represents a fraction $r = 0.3(1)$ of the total scattering as for $j_{\text{eff}} = 1/2$ moments frozen on a time scale that exceeds $\tau = \hbar/\delta E = 2.6$ ps. This is contrary

to expectations given the so-called order by disorder mechanism for the easy plane frustrated pyrochlore antiferromagnet: in the presence of weak exchange disorder, the easy plane short range order we observe was thought to be unstable towards the development of true long range order in a second order phase transition.

An interesting factor of potential significance to understand this situation is that exchange disorder in $\text{NaCaCo}_2\text{F}_7$ may be correlated contrary to assumptions in the theoretical work. Exchange disorder arises from the distribution of Na^+ and Ca^{2+} on the A-site of the lattice, which in turn forms a lattice of corner-sharing tetrahedra. Coulomb repulsion

is minimized when each tetrahedron satisfies an ice rule accommodating exactly two each of sodium and calcium. To explore this potential explanation, diffraction measurements in search for the corresponding diffuse structural scattering will be pursued.

In summary, MACS has provided a comprehensive map of spin correlations in the first of a new family of pyrochlore fluorides. The measurements show Co-tetrahedra are antiferromagnetically correlated with an easy plane configuration at low energies and a uniaxial damped mode near 5 meV. A theoretical prediction of long range "order by disorder" in this easy plane system notwithstanding, we find an antiferromagnetic correlation length of just 16 Å in the low T frozen state.

Correlations in the exchange disorder arising from Coulomb repulsion on the mixed cation A-site may be a relevant factor in this intriguing new class of frustrated magnets.

Electric field control of interfacial ferromagnetism in oxide heterostructures

A. J. Grutter¹, B. J. Kirby¹, M. T. Gray^{2,3}, C. L. Flint^{2,3}, U. S. Alaan^{2,3}, Y. Suzuki^{3,4}, and J. A. Borchers¹

Directly controlling magnetism and magnetic materials through the application of a bias voltage is an important and persistently elusive goal in the development of new magnetoelectric devices. Only in recent years have new thin film deposition techniques and a greater understanding of complex magnetic oxides enabled significant progress to be made in engineering magnetoelectric coupling [1]. For the most part, successful attempts at electric field control of magnetism have employed ferro- or piezoelectric layers to induce structural distortions in ferromagnetic layers such as FeRh or (La, Sr)MnO₃ [1]. Instead of relying on structural tuning, we have established electric field control of ferromagnetic CaRuO₃/CaMnO₃ heterostructures through modification of the interfacial band structure. Using polarized neutron reflectometry (PNR), we probe the voltage dependent magnetization of an interfacial ferromagnetic layer that is a single atomic monolayer thick. Our results demonstrate that the application of a bias voltage increases the magnetic moment of this ferromagnetic layer to 300 % of the unbiased value.

We selected the CaRuO₃/CaMnO₃ system for its extreme sensitivity to changes in the interfacial electronic state [2, 3]. In the bulk, CaRuO₃ is a paramagnetic metal while CaMnO₃ is an antiferromagnetic insulator. Thus, neither component exhibits a spontaneous magnetization on its own. When grown as a bilayer or superlattice, however, it has been well established that ferromagnetism emerges at the interface between the two materials [2, 4]. The associated spontaneous magnetization is tightly confined to an interfacial layer of CaMnO₃ with a thickness of ≈ 4 Å [3, 5, 6]. Density functional theory calculations and recent experimental results suggest that the origin of the ferromagnetism is leakage of mobile conduction electrons from the metallic CaRuO₃ to the antiferromagnetic CaMnO₃ [3]. Although insulating CaMnO₃ is normally dominated by antiferromagnetic superexchange interactions among its highly localized and immobile electrons, the injection of small numbers of delocalized, mobile electrons results in weak ferromagnetic double exchange.

Thus, competition develops between the ferromagnetic and antiferromagnetic interactions and a compromise is reached between the two states. The resulting net magnetization is approximately $1 \mu_B$ per interfacial Mn ion, a factor of three weaker than the $3 \mu_B/\text{Mn}$ we expect from fully aligned Mn⁴⁺ ions. It is therefore understood that the magnetic moment of interfacial Mn atoms are canted relative to each other, being neither fully parallel nor fully antiparallel.

It should be possible to tip the balance between the ferromagnetic and antiferromagnetic states by controlling the number of electrons leaking into the CaMnO₃. By creating a capacitor-like structure and applying an electric field, we can encourage migration of additional electrons across the interface, where they will facilitate a strengthened double exchange interaction. Thus, we fabricated the bilayer structure shown in Figure 1, with electrodes on top of the structure and on the rear of the substrate. Despite the large distance between the front and back electrodes, the extremely high dielectric constant of SrTiO₃ permitted large numbers of electrons to be accumulated even at relatively small potential of ± 400 V.

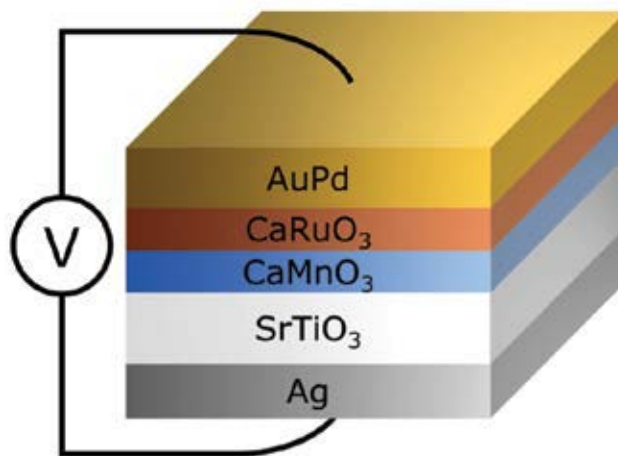


FIGURE 1: The capacitor-type samples structure incorporates a rear electrode on the SrTiO₃ substrate, 9 unit cells of CaMnO₃, 3 unit cells of CaRuO₃, and a capping electrode of AuPd.

¹NIST Center for Neutron Research, National Institute of Standards and Technology, Gaithersburg, MD 20899

²Department of Materials Science and Engineering, Stanford University, Stanford, CA 94305

³Geballe Laboratory for Advanced Materials, Stanford University, Stanford, CA 94305

⁴Department of Applied Physics, Stanford University, Stanford, CA 94305

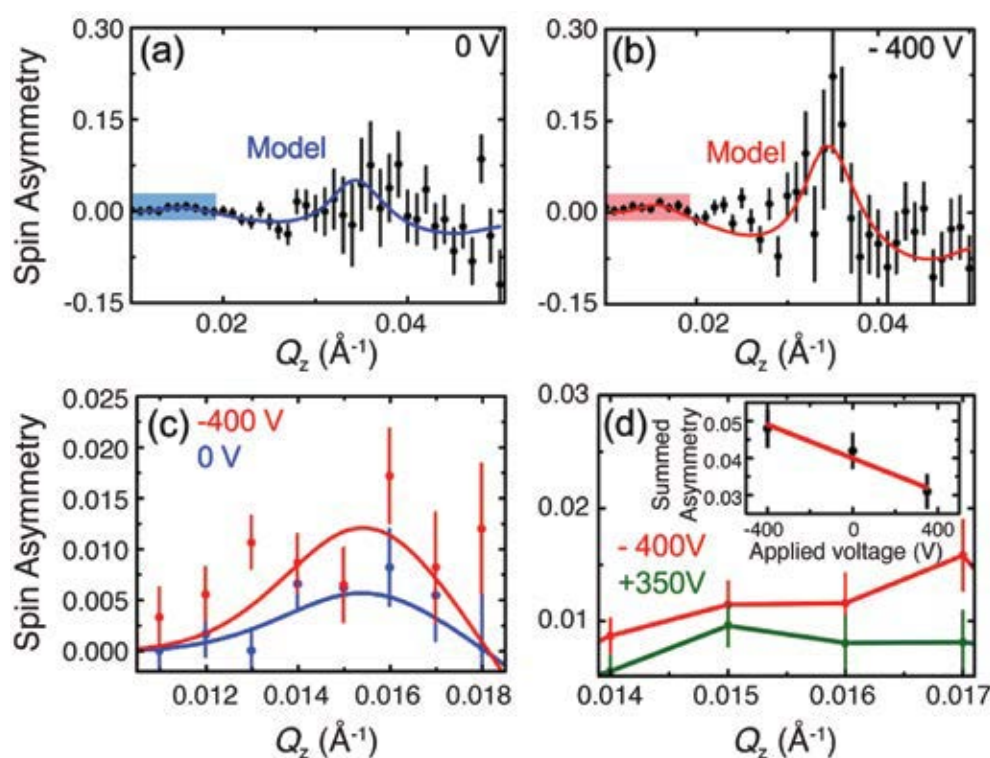


FIGURE 2: Spin asymmetry of the neutron reflectivity at (a) 0 V and (b) -400 V. The spin asymmetry is the normalized difference between the reflectivity of spin-up and spin-down neutrons and the magnitude of the peaks is directly proportional to the magnetization. (c) The most statistically significant portion of the measurement is shown at very low Q , where a comparison of the two voltage states shows a clear difference. (d) A second measurement at low Q in which voltage is varied from -400 V to +350 V at 10 K. The inset shows integrated intensity of spin asymmetry.

We previously isolated the magnetism in these interfaces through the fabrication of superlattices in which alternating layers of CaRuO_3 and CaMnO_3 are stacked repeatedly [5]. In this way, many interfaces are incorporated into a single sample, yielding magnetic moments large enough to study using techniques such as SQUID magnetometry. However, the need to apply an electric field limited us to a bilayer structure with a single $\text{CaRuO}_3/\text{CaMnO}_3$ interface. The signal arising from a single interface is well below the noise floor of most magnetometry techniques, and such a small magnetic moment may also originate from microscopic contamination by ferrous particulates. Fortunately, because PNR is only sensitive to the magnetization of objects that reflect the neutron beam, we may be certain that all of the measured signal arises exclusively within the sample. Additionally, the extreme sensitivity of PNR allows the detection of a magnetic moment arising from a single atomic monolayer. Finally we can use PNR simulation tools to extract the interfacial magnetization and model the structural and magnetic depth profile of the sample.

Therefore, we cooled our samples to 10 K in a variety of electric fields and measured the voltage dependence of

the magnetization. The measurements in Figure 2(a), 2(b) and 2(c) show the spin asymmetry after cooling in applied voltages of 0 V and -400 V. The spin asymmetry is the difference in measured reflectivity of spin-up neutrons and spin-down neutrons divided by the sum. For this measurement, the magnitude of the spin asymmetry is directly proportional to the magnetization. Despite the extreme difficulty of detecting such a small magnetic signal, a significant change in the spin asymmetry is observed under an applied voltage of -400 V. Furthermore, we show in Figure 2(d) that even at constant temperature the magnetization is highly voltage dependent over a range from -400 V to +350 V. Through careful statistical

analysis of each measurement, we have determined that applying a large bias voltage increased the magnetization by a factor of 2.5 to 3.0, precisely as expected for a fully ferromagnetic state.

Thus, we have demonstrated the ability to detect and control the magnetization occurring at the $\text{CaRuO}_3/\text{CaMnO}_3$ interface. By increasing and decreasing the amount of electron leakage across the interface, we may move the system from a canted antiferromagnetic state to one in which double-exchange mediated ferromagnetism completely dominates at the interface. This represents a new and relatively unexplored mechanism through which emergent properties at functional magnetic interfaces may be controlled.

References

- [1] R. O. Cherifi *et al.*, *Nature Materials* **13**, 345 (2014).
- [2] K. S. Takahashi *et al.*, *Appl. Phys. Lett.* **79**, 1324 (2001).
- [3] B. R. K. Nanda *et al.*, *Phys. Rev. Lett.* **98**, 216804 (2007).
- [4] J. W. Freeland *et al.*, *Phys. Rev. B* **81**, 094414 (2010).
- [5] C. He *et al.*, *Phys. Rev. Lett.* **109**, 197202 (2012).
- [6] A. J. Grutter *et al.*, *Phys. Rev. Lett.* **111**, 087202 (2013).

A tale of two spin-ladders in SrHo_2O_4

J.-J. Wen¹, W. Tian², V. O. Garlea², S. M. Koohpayeh¹, T. M. McQueen^{1,3}, H.-F. Li^{4,5}, J.-Q. Yan⁶, D. Vaknin⁷, and C. L. Broholm^{1,2,8}



The combination of single ion anisotropy, anisotropic exchange interactions, and dipolar interactions lead to complex collective phenomena in rare-earth-based magnets. Through careful analysis of these effects and wide-angle neutron scattering experiments using the MACS instrument, we explain the enigmatic coexistence of long- and short-range order in SrHo_2O_4 , and in the process uncover a new mechanism by which long-range order can be averted in frustrated magnets.

The orthorhombic structure of SrHo_2O_4 features two distinct holmium sites marked red and blue in Fig. 1. Their apparent similarities belie their distinct anisotropic magnetism. Because of the different electrostatic environment associated with their oxygen coordination, blue sites can only support a magnetic moment along the b-direction while red holmium spins are oriented along the c direction. This provides the unusual circumstance that single crystal susceptibility measurements can separately access the magnetism of red and blue holmium through probing the field along the crystallographic c and b direction respectively. Such measurements indicate that holmium forms zigzag spin ladders with differing rail and rung interactions. For blue ladders, the inter- and intra-rail interactions favor antiferromagnetic rails while the ground state for red ladders consists of antiparallel ferromagnetic rails (Fig. 1(b)). Another difference between red and blue holmium sites is apparent in the spectrum of crystal field excitations: red spin chains have low energy crystal field

levels that facilitate thermalization, while no low lying energy levels are available to facilitate blue spin flips.

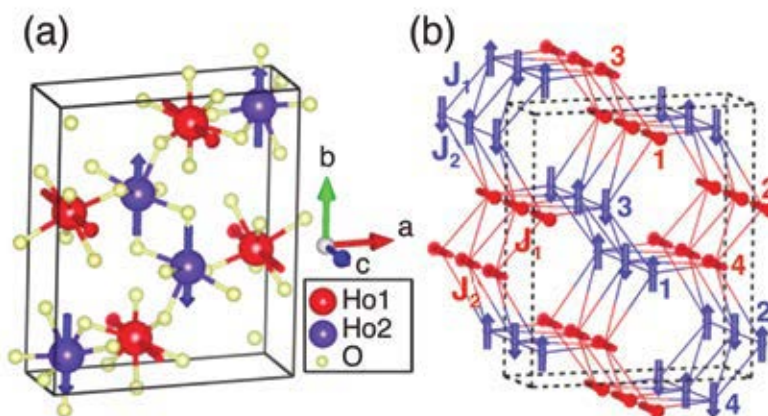


FIGURE 1: The crystal structure of SrHo_2O_4 features two similar-looking but distinct spin ladders. (a) Shows the different six-fold oxygen coordination of blue and red holmium sites that yield different easy axes. (b) Shows the corresponding distinct orders: red ladders feature longitudinal oppositely aligned spin-rails. Blue ladder spins are perpendicular and alternate.

The results of elastic magnetic neutron scattering measurements conducted on the MACS instrument are summarized in Fig. 2. Both at high temperatures (top row of Fig. 2) and low temperatures (middle row of Fig. 2) the $(0KL)$ plane of scattering (right column of Fig. 2) features ridge-like structures that are narrow in the $(00L)$ direction. This is diffraction evidence that spin correlations extend furthest along the c-axis. The $L = 0$ ridge is associated with the red chains with ferromagnetic rails while the $L = 0.5$ ridge indicates unit cell doubling and thus antiferromagnetic rails as anticipated from susceptibility measurements along the b-direction and depicted for blue spins in Fig. 1(b).

¹Institute for Quantum Matter and Department of Physics and Astronomy, The Johns Hopkins University, Baltimore, MD 21218

²Oak Ridge National Laboratory, Oak Ridge, TN 37831

³Department of Chemistry and Department of Materials Science and Engineering, The Johns Hopkins University, Baltimore, MD 21218

⁴Jülich Centre for Neutron Science (JCNS), Forschungszentrum Jülich GmbH, Outstation at Institut Laue-Langevin, Boîte Postale 156, F-38042 Grenoble Cedex 9, France

⁵Institut für Kristallographie der RWTH Aachen University, D-52056 Aachen, Germany

⁶University of Tennessee, Knoxville, TN 37996

⁷Iowa State University, Ames, IA 50011

⁸NIST Center for Neutron Research, National Institute of Standards and Technology, Gaithersburg, MD 20899

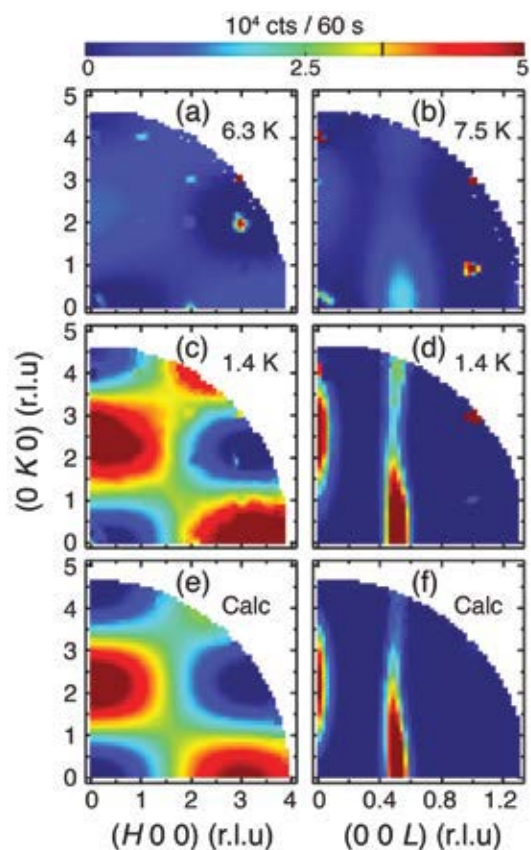


FIGURE 2: Diffuse elastic magnetic scattering from orthorhombic SrHo_2O_4 in the quasi-one-dimensional paramagnetic phase. The red (blue) spins shown in Fig. 1 give rise to the streak at $L = 0$ ($L = 0.5$) in frame (d). Frame (c) shows the inter-rail interference scattering for red spin ladders. Frames (e) and (f) show the calculated intensity based on the ANNNI model with exchange constants derived from susceptibility data.

In the $(H00)$ plane of scattering (Fig. 2 left column) that probes red chains with ferromagnetically oriented rails ($L = 0$) very broad structures that extend throughout the Brillouin zone are observed. This indicates that spin correlations do not extend beyond red chains to the neighboring blue chains resulting in SrHo_2O_4 displaying decoupled spin-ladders down to 1.4 K. The reason for this decoupling is apparent from Fig. 1(b): the discordant modulation of magnetism along the blue and red rails of the spin ladders precludes their correlation.

A comprehensive theoretical understanding of the magnetism of decoupled Ising spin ladders exists. Indeed, closed form expressions for the temperature dependent spin correlations are available. Based on the near and next nearest neighbor interactions for red and blue spin chains

derived from susceptibility measurements along the c and b crystalline directions respectively, and the temperature of the measurement, Figs. 2(e-f) show a calculation of the magnetic diffraction intensity pattern in the two reciprocal lattice planes. The outstanding agreement between the experiment and the theoretical calculation down to the slight modulation of the $L \approx 0.5$ ridge position, gives confidence that our proposed framework describing the magnetism of SrHo_2O_4 is correct.

The most puzzling aspect of SrHo_2O_4 now finds a natural explanation within this framework. Both in previous measurements on powder samples and in the present measurements on single crystalline samples conducted at HFIR, it was found that long-range spin order only develops on red spin ladders while blue spin ladders fail to develop coherent magnetic order. For a single red spin ladder with ferromagnetic rails, only two different variants of order exist and these are related by reversing the direction of all spins. In contrast, each antiferromagnetic rail of blue ladders has two inversion variants, which can be paired with the corresponding two variants of the opposite rail for a total of four degenerate ground states. As blue spin chains are cooled the theory alluded to above posits their thermal spin configurations consist of increasingly longer segments of one of these four states separated by soliton-like defects.

Thus when cooling SrHo_2O_4 , the following occurs: red spin ladders, for which thermalization is facilitated by low-lying crystal field levels develop long-range inter-ladder order at $T = 0.68(2)$ K. When this Ising order reaches saturation at $T = 0.52(2)$ K, red ladders effectively isolate the blue ladders that they surround because their ferromagnetic rails are discordant with the antiferromagnetic blue rails. As a result, thermalization seizes blue ladders in place and these are left with the low density of soliton-like defects associated with their thermal equilibrium at $T = 0.52(2)$ K. While there are already relatively long-range spin correlations along blue ladders at this temperature, there can be no inter-ladder coherence because this is thoroughly disrupted by remnant soliton-like defects. Thus it happens that order on red ladders can arrest the development of inter-ladder order on blue ladders. This curious tale of two types of spin ladders shows that a magnetically disordered state can persist within a high-quality single crystal not because it is energetically favorable, but because cooling kinetically traps the disordered state.

Magnetism and superconductivity in non-centrosymmetric topological RPdBi half-Heusler semimetals

Y. Nakajima¹, R. Hu¹, K. Kirshenbaum¹, A. Hughes¹, P. Syers¹, X. Wang¹, K. Wang¹, R. Wang¹, S. Saha¹, D. Pratt², J. W. Lynn², and J. Paglione¹

Topological Insulators (TIs), lacking spontaneously symmetry-breaking ordered states, are characterized by the presence of gapless boundary modes with chirality. In the so-called Z2 two and three-dimensional systems, these topologically protected metallic states have the potential for realizing new technologies in spintronics and quantum computation. Besides the intriguing topological boundary states per se, the combination of topologically ordered and symmetry-breaking ordered states such as superconductivity and magnetic order gives rise to new and exotic collective modes in topologically non-trivial materials. In particular, antiferromagnetism breaks time reversal and translational symmetries simultaneously, but can be preserved together, yielding a new, antiferromagnetic TI [1]. Despite extensive studies on bismuth-based TI materials, only a few materials have been identified that may harbor the combination of symmetry-breaking and topological phases.

One such promising candidate class of materials for the realization of combined topological and symmetry-breaking orders is the family of cubic RPdBi (R =rare earth) half-Heusler compounds [2]. These compounds are located at the border between topologically trivial and non-trivial electronic structure, allowing the band inversion strength to be tuned via atomic number, lattice density, and spin-orbit coupling strength. The R ions occupy a face-centered-cubic (fcc) lattice that renders magnetic structures ideal for antiferromagnetic TIs, while the superconductivity that emerges in this non-centrosymmetric crystal structure is exotic, providing unique opportunities to investigate the interplay of these states not only with each other but also with TI properties.

We have performed a systematic study of the superconductivity and magnetism in polycrystalline and single crystals of the half-Heusler series RPdBi (R = Y, Sm, Gd, Tb, Dy, Ho, Er, Tm, and Lu) using magnetization, susceptibility, specific heat, charge transport, and neutron diffraction [3].

The 4f electrons are expected to be localized and this has been confirmed by bulk measurements, which can be simply described by crystal-field-split free R^{3+} ion moments. Fig. 1a shows the neutron magnetic diffraction pattern for DyPdBi on a powdered sample of crushed single crystals, with strong magnetic Bragg peaks corresponding to half-integral reflections of an fcc type-II antiferromagnet. This magnetic structure is characterized by a doubling of the simple fcc Dy unit cell along all three crystallographic directions as illustrated in the inset of Fig. 1b, with ferromagnetic layers stacked antiferromagnetically along the [111] direction, a magnetic symmetry of particular interest for topological antiferromagnetism [1]. The R = Tb and Ho materials exhibit the identical spin structure. A mean-field fit of the temperature dependence of the intensity of the (1/2, 1/2, 1/2) Bragg peak (Fig. 1b) establishes the antiferromagnetic transition temperature T_N = 4.9 K for a single crystal of TbPdBi, in excellent agreement with the transport and magnetic measurements and previous measurements on powders [4].

The superconductivity in RPdBi is revealed by low temperature charge transport and magnetic measurements, as summarized in the phase diagram of Fig. 2 where the superconducting transition temperature T_C and T_N are plotted as a function of the de Gennes factor $dG = (g_J - 1)^2 J(J + 1)$. Here g_J is the Landé factor and J is the total angular momentum of the R^{3+} ion Hund's rule ground state. T_N clearly scales well with dG for RPdBi, which indicates a Ruderman-Kittel-Kasuya-Yoshida (RKKY) exchange interaction between the conduction electrons and the local magnetic moments that induces the long-range magnetic order. On the other hand, T_C is suppressed linearly with dG , which indicates that the magnetic R^{3+} ions break the superconducting pairs. This coexistence of magnetism and superconductivity in this system serves as a prototype platform to elucidate the coupling of topological order with symmetry-breaking states.

¹Center for Nanophysics and Advanced Materials, Department of Physics, University of Maryland, College Park, MD 20742

²NIST Center for Neutron Research, National Institute of Standards and Technology, Gaithersburg, MD 20899

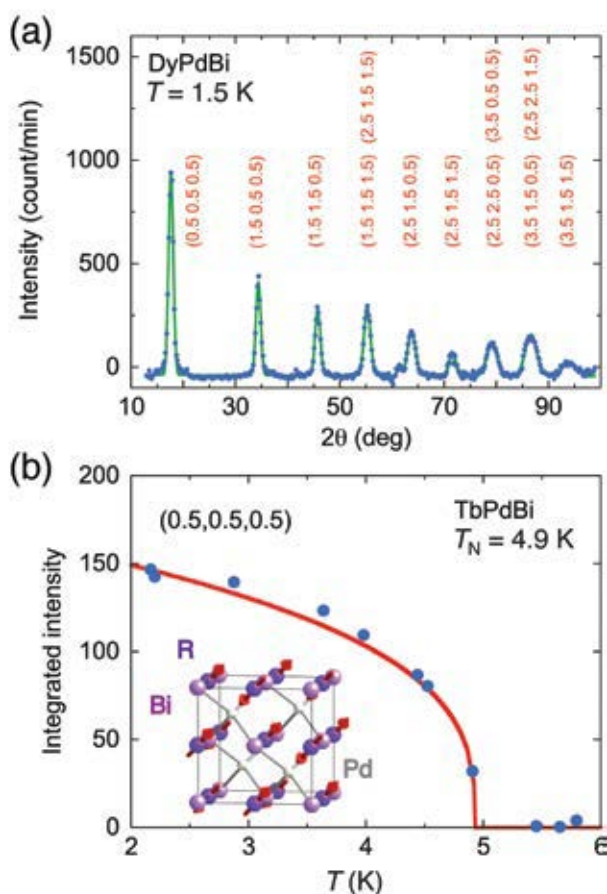


FIGURE 1: Antiferromagnetic order characterized by elastic neutron diffraction. (a) Low temperature magnetic diffraction pattern of DyPdBi obtained by subtracting the background data (18 K) from low temperature data (1.5 K). Labels indicate the series of half-integer antiferromagnetic peaks. (b) Intensity of the (1/2, 1/2, 1/2) magnetic Bragg peak for single-crystal TbPdBi. Solid curve is a mean-field fit to the data, and the inset shows a schematic of the antiferromagnetic spin structure.

In summary, we have investigated the coexistence of magnetism and superconductivity in the single-crystal *RPdBi* series. The magnetic rare earth members investigated so far exhibit an antiferromagnetic state characterized by ferromagnetic planes of spins stacked antiferromagnetically along the [111] direction, induced by the RKKY interaction between conduction electrons and localized moments. All *RPdBi* members except GdPdBi are superconductors. The anticorrelation between the magnetism and

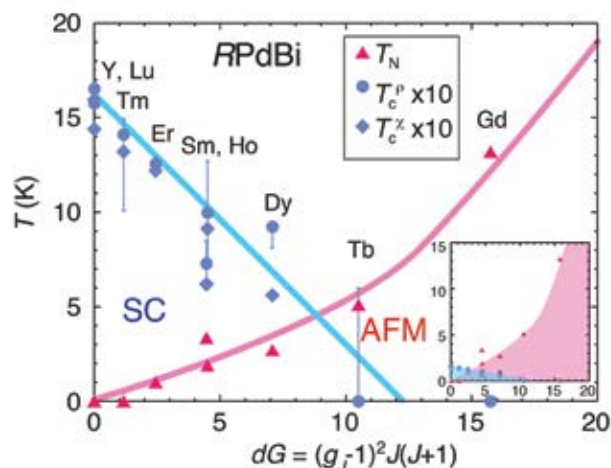


FIGURE 2: Phase diagram of the *RPdBi* series, demonstrating the evolution of the superconducting and antiferromagnetic states as a function of de Gennes factor $dG = (g_J - 1)^2 J(J+1)$. The superconducting transition T_c (blue) is obtained from the midpoint of the resistive transition (circles; upper and lower error bars indicate onset and zero resistance) and the onset of diamagnetism in ac susceptibility (diamonds), and Néel temperatures T_N (red triangles) are obtained from dc magnetic susceptibility. The plotted T_c is scaled by a factor of 10, and solid lines are guides to the eye. Note that T_c (T_N) for SmPdBi is lower (higher) than that for HoPdBi. Inset: unscaled T_c and T_N versus dG .

superconductivity is revealed by the scaling with the de Gennes factor, indicating *RPdBi* not only to be a new family of interesting magnetic superconductors, but together with their topological properties promise to be prototype systems to elucidate the emergence of novel quantum states of matter.

References

- [1] S. K. Mong, A. M. Essin, J. E. Moore, *Phys. Rev. B* **81**, 245209 (2010).
- [2] S. Chadov, X. Qi, J. Kubler, G. H. Fecher, C. Felser, S. C. Zhang, *Nature Mater.* **9**, 541 (2010).
- [3] Y. Nakajima, R. Hu, K. Kirshenbaum, A. Hughes, P. Syers, X. Wang, K. Wang, R. Wang, S. Saha, D. Pratt, J. W. Lynn, J. Paglione, *Sci. Adv.* **1**, e1500242 (2015).
- [4] K. Gofryk, D. Kaczorowski, T. Plackowski, A. Leithe-Jasper, Y. Gin, *Phys. Rev. B* **84**, 035208 (2011).

Stresses in aluminum sheet joined by the flow drill screwing process

T. Gnäupel-Herold and J. Milner

Flow drill screwing (FDS) is a novel technology designed to address the challenges of joining aluminum sheets for automotive applications. The predominant method for joining steel sheets is spot welding, which is more problematic for aluminum because it requires chemical de-oxidation of the sheet and frequent electrode changes. Similar to friction stir welding, in FDS the material is frictionally heated to a viscous state by pressing the rotating screw on the sheet, softening the sheet locally, allowing the screw to penetrate. When rotation stops, the aluminum alloy hardens and forms an intimate and strong contact with the screw. The whole joining operation takes only a few seconds, thus making it competitive with spot welding for production purposes. The scope of this work is to characterize the residual stresses in FDS joints, and to explore the role of the down force and the behavior under applied stress.

The process of FDS joining is remarkably simple: a screw with a wide head and a tapered end is pressed on the sheets to be joined and, through a combination of rotation (2000 min^{-1}) and down force (up to 2 kN) heats up the sheet metal through friction. Once the sheet reaches a viscous state, penetration starts, and the controlling parameter is now the fixed ratio of rotation speed and forward translation where during one revolution the screw is translated by the screw pitch distance (here: 0.8 mm). Similar to a conventional screw joint a typical FDS joint of two sheets penetrates only the bottom sheet while the top sheet has a pilot hole. Note that the samples investigated here differ in that the top sheet had no pilot hole, i.e., both sheets are threaded. The latter prohibits the axial clamping between sheets in conventional screw joints. The down force contributes little to clamping of the two sheets because the material surrounding the bolt is too soft for bearing any significant force during joining. As a side effect, some of the sheet material displaced by the bolt accumulates between sheets and it increases sheet separation (see Figure 1).

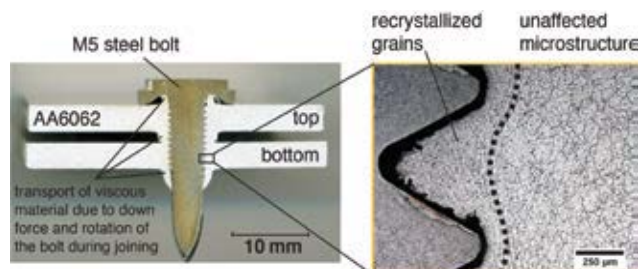


FIGURE 1: Left: cross section of a FDS joint of the type investigated here. Right: Close-up of the microstructure at the thread interface. The dark region at the interface is not empty space but an artifact of the sample preparation.

For a specific joining process considerations of speed and cost are front and center; the residual stresses become important because of their role regarding the strength of the joint and its fatigue properties. Residual stresses originate from two main sources: a) the difference in thermal expansion coefficients (CTE) between steel and aluminum ($\text{CTE}_{\text{Al}} \approx 2 \times \text{CTE}_{\text{steel}}$) and b) the displacement of aluminum through plastic flow. The interplay between the two effects has not yet been analyzed which emphasizes the need for experimental data even more. Stress characterization of the FDS joint is done best non-destructively through diffraction which analyzes the spatial and orientation distribution of elastic lattice strains in the aluminum sheet. Results presented here were obtained at the BT8 Residual Stress Diffractometer using a cuboidal gage volume of $(2 \times 2 \times 2) \text{ mm}^3$. Measurements in aluminum were done at 1 mm spacing, starting 1 mm away from the screw interface. Because of strong preferred orientation the measurements could not be done along the principal directions of the sheet; instead, directions of strong intensity for the (311) reflection were used which were obtained from a pole figure measurement. In addition to two FDS samples (thickness 3.17 mm; down forces of 2167 N and 1325 N) one single sheet was measured in order to study the stress field around a conventional screw (sheet thickness 3.17 mm, M5 cap screw, 4.6 Nm tightening torque). For simplicity, and because the aluminum sheet is elastically nearly isotropic, the system is considered to have rotational symmetry, thus stresses are shown in terms of radial and tangential stresses (Figure 2).

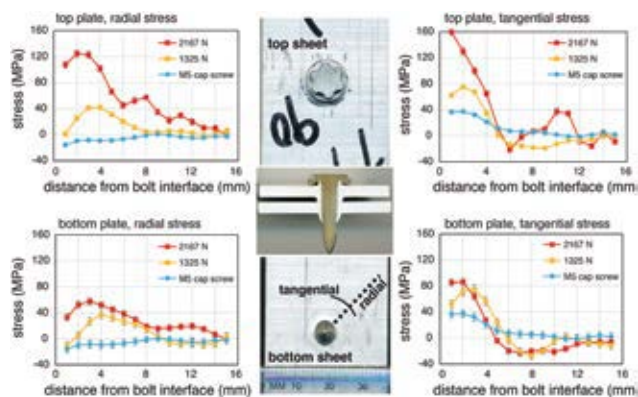


FIGURE 2. Residual stresses for the two sheets and for different down forces. For comparison, a conventional M5 screw joint without down force and no heating involved.

Stresses around the FDS joint are significantly higher than for a cap screw, and stresses are generally higher in the top plate. More significantly, stresses are tensile which is problematic if applied stresses produce stress concentrations in the proximity of bolted holes. Superposition of existing residual stresses can quickly reach yield stress levels or lead to unsatisfactory fatigue behavior. For testing under applied load lap shear of two sheets joined together by FDS is the most common scheme where top and bottom sheet are pulled in opposite directions (Figure 3).

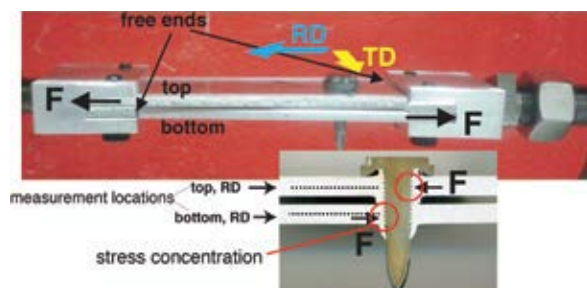


FIGURE 3. FDS joined sample (joined with 1325 N down force) in a stress rig for neutron measurements under applied load. The stress concentration region on the bottom plate was measured.

Sheets under applied load that have geometrical inhomogeneities such as holes with tight fitting pins 'see' a concentration of stress around these inhomogeneities; for this case, the analytical solution predicts that the superimposed external stress is compressive with a magnitude of $-4 \times$ the applied stress around the contact region where the pin radius vector is parallel to the applied load. Numerical solutions for loading of a tight fitting pin [1] find smaller factors around -1.2 for the radial stress and 0.5 for the hoop stress that would add more tensile stress to the already existing tensile stress. However, our sample is somewhat different from the ideal case in that it has both axial 'clamping' near the threaded region and the increased

sheet thickness near the bolt interface. The analytical solution and the numeric simulation do not include residual stresses, and it is assumed that applied stresses (including stress concentrations) are added to the residual stresses as long as the yield point is not exceeded. The total stresses were measured for the bottom plate along the RD line shown in Figure 3.

Due to the compressive nature of the force exerted by the screw the total stresses are reduced and radial stresses become compressive overall. However, the reduction is not nearly as big as expected for the analytical solution ($-4 \times \sigma_{\text{appl}}$) and much closer to the numerical one ($-1.2 \times \sigma_{\text{appl}}$). The observed hoop stress reduction does not agree with the simulation, which predicts that about 50 % of the applied tensile stress is *added* to the residual stress.

The findings presented here are the first glimpse into the behavior of an FDS joint under load. Theoretical predictions of stress concentrations made for simpler geometries do not provide an accurate description of the experimental results, thus highlighting the need for tailored theoretical solutions that also include the effects of the thread and the role of heat input and cooling conditions of the aluminum sheet. The stress distribution for thinner gage sheets is currently under investigation.

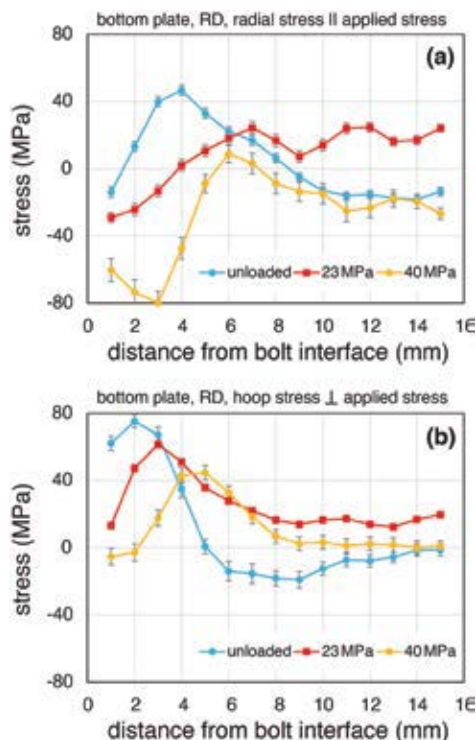


FIGURE 4. Radial stress (a) and hoop stress (b) along the RD line in the bottom sheet. Values in the legend describe the gross applied stress.

References

- [1] J. H. Crews Jr., C. S. Hong, I. S. Raju, NASA- Technical Paper 1862, NAS 1.60:1862 (1981).

Twisting neutron waves

D. A. Pushin,^{1,2} M. Arif,³ R. Barankov,⁴ C. W. Clark,^{3,5,6} D. G. Cory,^{1,7,8,9} and M. G. Huber³

We have recently demonstrated orbital angular momentum (OAM) control of neutrons, accomplished with macroscopic spiral phase plates and analyzed with neutron interferometry. Orbital angular momentum states represent a ‘twisting’ of a particle’s wavefront around its propagation axis. Previously demonstrated for light [1] and electron beams [2], OAM states have been exploited in various applications including studies of quantum entanglement and quantum information science, subwavelength microscopy, the rotation of nanoparticles, and in determining the chirality of metal oxides. However, control of OAM states for the neutron had not yet been achieved. This is despite the fact that neutrons already play an important role in many areas such as materials science, quantum information, and fundamental physics. Our techniques, applied to spatially incoherent beams, demonstrate the addition and the conservation of quantized angular momenta (L). Neutron-based quantum information science, foundational studies of quantum mechanics, and neutron scattering and imaging of magnetic, superconducting, and chiral materials, now have access to another fundamental, quantized degree of freedom.

Figure 1a shows a schematic diagram of the experiment as performed at the Neutron Interferometry and Optics Facility (NIOF) [4] at the NIST Center for Neutron Research. For background and stability reasons, the NIOF is located within three nested enclosures (as a Matryoshka doll). To minimize phase drifts during the week-long data collection times, the temperature of the innermost enclosure is actively controlled to remain at $24\text{ }^{\circ}\text{C} \pm 0.005\text{ }^{\circ}\text{C}$. The middle enclosure is a Faraday cage that adds additional temperature isolation and sound damping. Both inner enclosures sit on a 40 000 kg vibration-isolated table which

actively suppresses the mechanical noise spectrum above 0.5 Hz and is controlled with micron precision. A 15 mm diameter beam of neutrons enters the interferometer (analogous to a Mach-Zehnder interferometer) and is Bragg diffracted into two coherent paths. Spiral phase plates (SPP) are inserted into one of the paths such that the neutron acquires a variation of phase across its wavefront. The second blade of the NI is employed as a lossy mirror (reflectivity < 100 %) whose function is to redirect the beams onto the third blade of the NI where the two paths coherently mix. The interfering transmitted/reflected neutron paths are detected using a two-dimensional (2D) neutron camera and an integrating ^3He neutron counter. The integrating ^3He detector was used for aligning the system, monitoring of the reactor flux, measuring the initial phase (θ_0), and for monitoring phase drifts. A 2 mm thick plate of fused silica is installed between the second and third blades. This serves as a “phase flag”: by rotating this phase flag we can introduce and control a spatially uniform phase difference between neutron paths. The spatially resolved data from the 2D neutron detector provides information on the ‘twisting’ encoded on the neutron’s wavefront by the SPP.

The SPPs were machined out of dowels of aluminum by a 5-axis computer numerical control milling machine at the NIST machine shop. Since the incident neutron beam contains an incoherent mixture of different OAM states, we adopted the strategy of using interferometry to demonstrate SPP control of the average OAM of an incoherent neutron beam. Here the incident neutron wavefunction Ψ is simply modulated to $\Psi \rightarrow \Psi e^{i\theta(\phi)}$ through its transmission through the SPP. The phase $\theta(\phi)$ a function introduced by the SPP where the angle ϕ is defined in Fig. 1b. A step of the spiral of $h_5 = 112\text{ }\mu\text{m}$ corresponds to a $\theta(360^{\circ}) = 2\pi$ phase shift for a

¹ Institute for Quantum Computing, Waterloo, Ontario N2L 3G1

² Department of Physics and Astronomy at the University of Waterloo, Waterloo, Ontario N2L 3G1

³ National Institute of Standards and Technology, Gaithersburg, MD 20899

⁴ Photonics Center and Department of Biomedical Engineering at Boston University, Boston, MA 02215

⁵ Joint Quantum Institute, College Park, MD 20742

⁶ University of Maryland, College Park, MD 20742

⁷ Department of Chemistry at the University of Waterloo, Waterloo, Ontario N2L 3G1

⁸ Perimeter Institute for Theoretical Physics, Waterloo, Ontario N2L 2Y5

⁹ Canadian Institute for Advanced Research, Toronto, Ontario M5G 1Z8

neutron travelling through an aluminum plate. Similarly, spiral phase plates have been used by Peel *et al.* [3] to demonstrate orbital angular momentum in beams of x-rays. The phase of a neutron with wavelength (λ) passing through SPP with respect to free space is given by

$$\theta(\phi) = -N b_c \lambda h(\phi) = -N b_c \lambda \left[h_o + \frac{h_s \phi}{2\pi} \right]$$

Here N is the atom density and b_c is the coherent scattering length of aluminum. Figure 1c shows photographs of two spiral phase plates with $2h_s = 224 \mu\text{m}$. We fabricated several such plates, corresponding to phase singularities of 2π , 4π , 8π , and 15π .

Equivalently, we can describe acquired phase by the effective angular momentum $L = N b_c \lambda h_s / 2\pi$. Every OAM component of an incoherent beam entering the SPP obtains an additional phase 'twist' proportional to L . The average angular momentum, measured in units of \hbar , of the neutron after the interferometer is $\langle L \rangle = L + \langle L_{\text{int}} \rangle$, where $\langle L_{\text{int}} \rangle$ is the initial average angular momentum. For this experiment we used SPP with momenta, $L = (1, 2, 4, \text{ and } 7.5)$. For a non-integer effective thickness of the phase plate, such as $L = 7.5$, a superposition of different OAM states would be produced with dominant contributions at $L = 7$ and $L = 8$. In general, given the uncertainty of L , even for the values of $L = m + \delta L$ close to the integers $m = 0, \pm 1, \dots$ the resulting state should always be a mixture of OAM states. Figure 2 shows a false-color representation of the 2D intensity distribution using the 2D detector placed after the third blade of the NI where we see the interferograms generated by SPPs corresponding to $L = (1, 2, 4, \text{ and } 7.5)$.

We have demonstrated control of orbital angular momentum of incoherent neutrons using easily manufactured macroscopic SPPs. The average OAM of the beams has been measured using a perfect crystal neutron interferometer. The interferometric experiments exemplify the celebrated particle-wave duality of neutrons: on the one hand, neutrons are detected as individual particles, while on the other, neutrons traverse space like waves, carrying quantized values of orbital angular momentum. Our interferograms indicate that each of these individual states has its orbital angular momentum changed by the same amount when passed through a spiral phase plate of integer order. Combining the actions of several phase plates demonstrates the additivity of orbital angular momenta. Possible future directions of such studies are: quantum information in higher dimensions including quantum error correction optimizing SPPs and experimenting with alternative phase-shifting devices,

such as the fork-dislocation gratings used in OAM control of electrons and photons; spatial filtering of the input beam to achieve better spatial coherence of the beams leading to production of OAM states; entanglement of neutron spin and orbital angular momenta; and angular-momentum-resolved measurements of neutron scattering. OAM states may also extend phase-contrast neutron imaging to two dimensions.

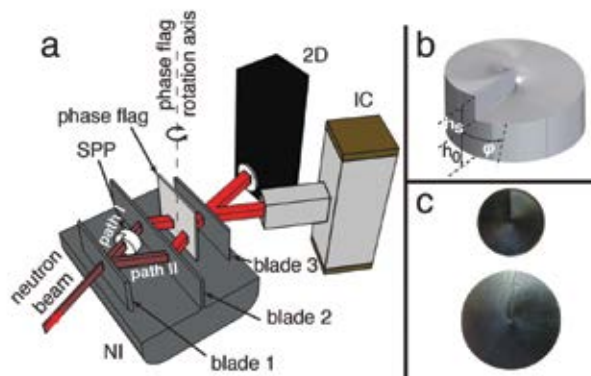


FIGURE 1: Schematic diagram of the neutron interferometer (NI). a) The incident neutron beam is coherently split into two coherent paths by the Bragg diffraction and then detected by an integrating counter (IC) and two-dimensional imaging detector (2D). The neutron counts recorded by the two detectors contain information about the relative phase of the neutron wavefunction accumulated along the two separate paths. The spiral phase plate is placed in one path to produce a spatial phase distribution across the neutron wavefront. b) Schematic diagram of the spiral phase plate (SPP). The step of the spiral, h_s , is chosen to match a 2π phase shift difference between a path passing the plate and the reference path in air. c) Photographs of actual SPPs with $h_s = 224 \mu\text{m}$ with diameters of 10 mm (above) and 15 mm (below).

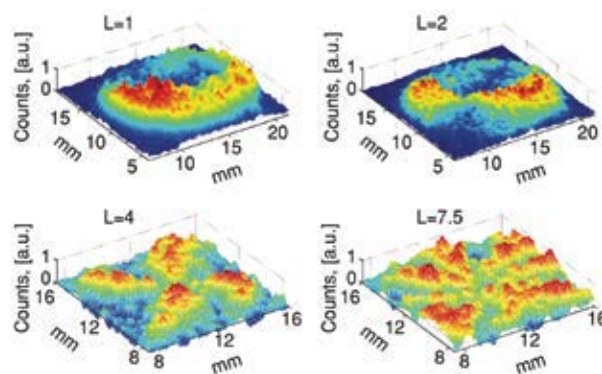


FIGURE 2: Phase Profile Created by SPP. These intensity profiles are proportional to phase distribution of a neutron beam passing through the spiral phase plates for $L = (1, 2, 4, \text{ and } 7.5)$.

References

- [1] A. M. Yao and M. J. Padgett, *Adv. Opt. Photon.* **3**, 161 (2011).
- [2] A. G. Peele *et al.*, *J. Opt. Soc. Am. A* **21**, 1575 (2004).
- [3] B. J. McMoran *et al.*, *Science* **331**, 192 (2011).
- [4] D. A. Pushin *et al.*, *Adv. High Energy Phys.* **2015**, 687480 (2015).

Combining SANS and USANS to characterize porosity evolution during hydrothermal alteration of mantle rocks

B. M. Tutolo,^{1,2} C. Gagnon,³ D. F. R. Mildner,³ M. O. Saar,^{1,4} and W. E. Seyfried, Jr.¹



Igneous rocks underlying Earth's oceans contain the equivalent of approximately 2 % of the ocean's volume of water [1]. Peridotites, which are mantle-sourced igneous rocks containing exceptionally low concentrations of the element Si, can comprise 40 % (by mass) or more of the oceanic crust at slow and ultra-slow spreading segments of the mid-ocean ridges. When these rocks are exposed to seawater at near-surface temperatures (i.e., < 350 °C), they present one of the most chemically reactive systems on Earth [2]. As such, field samples of peridotite are almost always hydrothermally altered in complex ways, and quite often the rocks have been completely converted to hydrous secondary phases such as serpentine. This process, broadly termed "serpentinization," presents a challenging problem in the Earth sciences, because freshly crystallized mantle peridotites are essentially impermeable to infiltrating seawater, and serpentinization reactions can increase the rock volume (thereby making them even more impermeable) by around 40 % ([2,3], Fig. 1). In this study, we have performed small-angle neutron scattering (SANS) and ultra small-angle neutron scattering (USANS) on the NG7 and BT5 instruments, respectively, in order to analyze the evolution of porosity, pore size distribution, and specific surface area (SSA) of pores and mineral-pore interfaces in the range of $\approx 10 \mu\text{m}$ to $\approx 10 \text{nm}$. These measurements represent the first physical measurements of the progression of serpentinization at this scale and provide key insights into the nanoscale mechanism of serpentinization.

Through experimental and field studies of serpentinized peridotite and associated fluids, researchers have developed constraints on the geochemical evolution of these systems [4]. However, the physical evolution of porosity and permeability with serpentinization progress has been much harder to constrain [2-5]. As demonstrated in Fig. 1, a primary research focus in this system is the question of how largely impermeable mantle rocks can change from freshly formed to nearly completely serpentinized within the relatively short time that they spend at temperatures conducive to serpentinization reactions. Recently, fundamental theoretical advances have been made in understanding the mechanism of

"reaction-driven cracking," or the physical cracking of rock minerals due to local overpressures associated with the crystallization of serpentine [2,3,5]. This mechanism, by opening up pore space within the host rock, provides a self-sustaining, positive feedback for pervasive serpentinization, and can be reconciled against field observations of serpentinized rocks (Fig. 1(b)). However, fundamental physical measurements of the evolution of flow pathways as the reactions proceed have not yet materialized, due to the challenging scale (i.e., nanometers to micrometers) at which the relevant processes occur.



FIGURE 1: Representative images of the way in which serpentinization affects the porosity and permeability of mantle rocks. In (a), we have presented an artistic representation of the freshly crystallized igneous texture of an olivine-rich mantle peridotite. Notably, pathways for fluid flow only exist along grain boundaries, and, as such, freshly crystallized mantle rocks are highly impermeable to infiltrating seawater. In (b), we present a cross-polarized photomicrograph of a serpentinized peridotite from off-axis at the mid-Atlantic Ridge. The serpentine-filled grain boundaries and fractures crisscrossing all olivine grains within this image provide clear evidence that seawater has pervasively infiltrated into this rock, and that the volume-increasing serpentinization reaction has the ability to fracture surrounding mineral grains.

¹ University of Minnesota, Minneapolis, MN 55455

² University of Oxford, Oxford, UK OX1 3AN

³ NIST Center for Neutron Research, National Institute of Standards and Technology, Gaithersburg, MD 20899

⁴ ETH-Zürich, Zürich, Switzerland

To fulfill this data need and capture the physical features of serpentinization on a scale beyond the resolution capabilities of conventional, image-based techniques, we have performed combined USANS on 11 sections of variably serpentinized field samples from both the 2 million-year-old Atlantis Massif oceanic core complex on the mid-Atlantic Ridge and the 1.1 billion-year-old Duluth Complex in northern Minnesota. These samples provide a considerable spectrum in style, intensity, and geochemistry of serpentinization. USANS analysis of the Atlantis Massif samples represent a particularly unique and rare opportunity, because they were sampled directly from the mid-Atlantic Ridge in the central Atlantic Ocean, where serpentinization is ongoing.

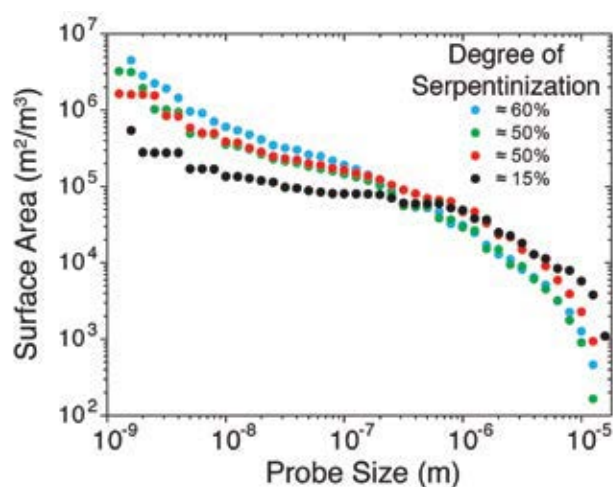


FIGURE 2: Representative plot of the evolution of multi-scale specific surface area (SSA) as a function of degree of serpentinization. Combined USANS scattering intensity data were approximated as a distribution of polydisperse, spherical pores [8,9], and the SSA was calculated as a function of probe size by summing the surface area of all pores within this fitted distribution with a size greater than the chosen probe size.

The benefits of USANS as a technique for discerning nanometer- to micrometer-scale features in geologic samples has become increasingly apparent over the last decade [6,7,8], and our study was particularly motivated by groundbreaking work previously performed by Navarre-Sitchler *et al.* [6] using NCNR resources. These researchers showed that USANS can be most effective for describing the progression of chemical reactions into natural, low porosity igneous rocks. Similar to previous studies, we have utilized the geologically tailored software PRINSAS [9] in order to analyze our data sets.

A representative quantification of the schematic reaction sequence illustrated in Fig. 1 is plotted in Fig. 2. These measurements indicate that, as serpentinization proceeds, the primary, micrometer-scale, grain boundary pores

illustrated in Fig. 1(a) are increasingly converted to intra- and inter-crystalline, nanometer-scale pores, which are intuitively associated with serpentine-filled fractures and reaction rims along grain boundaries (Fig. 1(b)). In porous materials where the pore size distribution spans multiple length scales (i.e., rocks), the SSA is a function of the size of the probe being used for the measurement [8]. Therefore, the fact that the more serpentinized samples have considerably more SSA when measured with probes in the range of $\approx 10^{-9}$ m to $\approx 5 \times 10^{-7}$ m gives a strong indication that pores with nano-scale roughness are increasingly created as the serpentinization reactions proceed. Notably, SSA of serpentinized mantle rocks measured by N_2 gas sorption (probe size = 4 Å), are in agreement with those calculated here [10]. Interestingly, the net calculated change in porosity from the least serpentinized section to the most serpentinized section presented in Fig. 2 is $\approx 1\%$, which is probably on the same order as the uncertainty of the calculations themselves. Therefore, counter-intuitively, it appears likely that the porosity generated during reaction-driven fracturing more or less offsets that destroyed by pore-space-filling serpentinization reactions. Together, this set of observations provides fundamental insight into the progress of serpentinization at the sub-micrometer scale and will help to inform further theoretical models of the coupled evolution of fluid flow and serpentinization in mantle rocks.

References

- [1] H. P. Johnson, M. J. Prius, *Earth Planet. Sci. Lett.* **216**, 565 (2003).
- [2] P. B. Kelemen, G. Hirth, *Earth Planet. Sci. Lett.*, **345**, 81 (2012).
- [3] B. Jamtveit, A. Malthe-Sørensen, O. Kostenko, *Earth and Planet. Sci. Lett.* **267**, 620 (2008).
- [4] W. E. Seyfried, N. J. Pester, B. M. Tutolo, K. Ding, *Geochim. Cosmochim. Acta* **163**, 59 (2015).
- [5] A. H. MacDonald, W. S. Fyfe, *Tectonophysics* **116**(1), 123 (1985).
- [6] A. K. Navarre-Sitchler, D. Cole, G. Rother, L. Jin, H. L. Buss, S. L. Brantley, *Geochim. Cosmochim. Acta* **109**, 400 (2013).
- [7] L. M. Anovitz, G. W. Lynn, D. R. Cole, G. Rother, L. F. Allard, W. A. Hamilton, L. Porcar, M. H. Kim, *Geochim. Cosmochim. Acta* **73**(24), 7303 (2009).
- [8] A. P. Radlinski, M. Mastalerz, A. L. Hinde, M. Hainbuchner, H. Rauch, M. Baron, J. S. Lin, L. Fan, P. Thiyagarajan, *Int. J. Coal Geol.* **59**(3), 245 (2004).
- [9] A. L. Hinde, *J. Appl. Cryst.* **37**(6), 1020 (2004).
- [10] I. Okland, S. Huang, I. H. Thorseth, R. B. Pedersen, *Chem. Geol.* **387**, 22 (2014).

Foamy porosity in gas shale

H. E. King, Jr.¹, A. P. R. Eberle¹, C. C. Walters¹, C. E. Kliewer¹, D. Ertas¹, and C. Huynh²



In the last decade, natural gas production from shale has grown to become a major energy supply for the United States. This rapid development of shale gas has been mirrored by an intense drive to understand the science underlying gas storage and transport for these small pore size, low permeability rocks. Shales are sedimentary rocks consisting of both organic and inorganic matter. As with conventional rocks, hydrocarbons are produced from pores. However, the inherently small particle size of shale's components sets a scale for the pores ranging from μm to nm. Efforts to characterize the pores have been challenging and are incomplete.

In the study highlighted here [1], we examined the pore architecture and connectivity in gas shales using a set of complimentary analyses. Key data on pore size and number, spanning several decades in size, was obtained through Small-Angle Neutron Scattering (SANS). We then compared these data to porosimetry and to imaging using helium ion microscopy (HIM). By combining analyses that are diagnostic of pore / pore-throat size with advanced imaging, we account for the total porosity and conclude that about one-third of the porosity is in the organic phase with a distinct pore size that is a direct result of thermal evolution of the kerogen within.

Samples were taken from cores of organic-rich, thermally mature shales having gas potential. The SANS samples were disks approximately 20 mm diameter and thickness ≈ 0.3 mm. Sample preparation for HIM analysis involved nothing more than mechanically exposing a fresh surface of the shale, fractured from a larger piece.

Typical scattering data are shown in Fig. 1a, where we have included USANS data down to $Q = 0.0001 \text{ \AA}^{-1}$. (Data at lower Q were affected by multiple scattering.) Three key features to note are: 1) at low Q there is a rollover to a lower power-law slope, 2) the mid Q data exhibit approximately power-law scaling, and 3) at high Q , there is a distinct intensity bump.

Similar to other porous sedimentary rocks, scattering from pores dominates. There is little contrast among the various mineral and organic phases; whereas the pore-to-matrix scattering length density contrast is 20 times that of the largest mineral-organic contrast. We ascribe the scattering to a polydisperse set of spherical pores [2] and fit that distribution via a numeric model for polydisperse spheres (PDSM) as follows:

$$I(Q) = (\Delta\rho)^2 \sum P^2(Q,r) F(r) V^2(r) N \Delta r$$

where N , $V(r)$, and $P(Q,r)$ are the number, volume, and form factor for the spheres of radius r . This technique, when applied to conventional porous rocks, has shown consistency between SANS porosity and various porosimetry data [3]. Here we find that the SANS porosity agrees well with helium porosimetry. The rollover in the power law at low Q indicates that larger features are not important. Indeed, analysis of the porosity as a function of Q , shows no significant contribution for data $Q < 0.001 \text{ \AA}^{-1}$. Consequently only SANS data were analyzed for the remaining samples.

A surprising outcome of the fits shown in Fig. 1 is the significant population of nearly uniform sized pores with diameters of ≈ 1.5 nm, seen for all of the shale gas samples we have analyzed, but absent for other organic-rich rocks, such as low maturity oil shale. Conventional

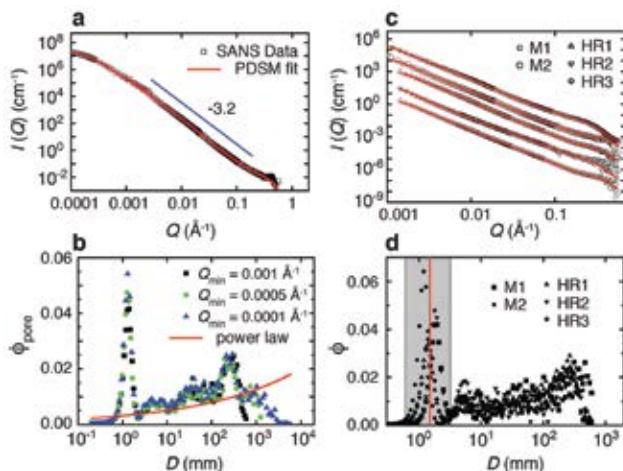


FIGURE 1: a) SANS and USANS for sample M2 with fit of the PDSM model. b) The pore size distribution function extracted from fit using different low- Q limits. c) Summary for all samples, data and model fits, each is shifted vertically for clarity. d) Pore size distribution function, with line representing average pore size.

¹ExxonMobil Research and Engineering Company, 1545 Route 22 East, Annandale, NJ 08801

²Carl Zeiss Microscopy, LLC, Applications Laboratory, One Corporation Way, Peabody, MA 01960

rocks exhibit only a power-law pore-size distribution, with the expected pore size distribution indicated by the line in Fig. 1b. Contrast matching experiments show that these small pores are located in the organic component of the shale, consequently the concentration of pores is considerably elevated in that small, $\approx 10\%$ mass fraction shale component. To account for pore-to-pore correlation required a new model, a Polydisperse Hard Sphere function. These fits showed that the volume fraction of pores in the organic is high, a volume fraction of (10 % to 35 %). We coin the term "foamy porosity" and show below how this is linked to gas evolution from the kerogen.

The shales were also analyzed using an Orion Plus HIM located at the Carl Zeiss facility at Peabody, MA. Resolution under the conditions utilized is better than 1 nm. Sample preparation by mechanically exposing a fresh surface of the shale through fracture, has been particularly effective in exposing thin layers of highly porous organic matter parallel to bedding planes.

By focusing on the organic layers and using an instrument sensitive to topology and with high resolution, we resolve a significant population of small pores in the organic phase, with some pores also present in the mineral matrix. Using the SANS-derived pore size distribution we calculated a 2D representation and compared that with a HIM imaged region from the same sample (Fig. 2) finding a close correspondence.

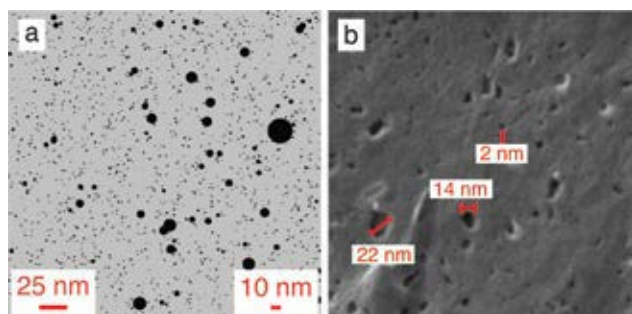


FIGURE 2: Example from sample HR3 showing a) calculated pore population from PDSM result, and b) helium ion image taken at same magnification as simulated image with selected pores labeled.

We suggest a possible origin of the unique population of nearly uniform pores in the organic phase. In the hypothetical scenario that the kerogen were not crosslinked, the interfacial energy Γ between these two phases would cause bubbles of the expelled fluid to coalesce into a macroscopic fluid phase via Ostwald ripening. In reality, by the time the phase separation starts, the kerogen network is already highly cross-linked, with a characteristic molecular weight of segments between crosslinks of several hundred. This corresponds to a typical

segment contour length L_c of order ≈ 1 nm. When cross-linking is present, there is an additional, elastic contribution to the free energy of each bubble. The net effect in this moderate deformation regime is an additional effective interfacial energy Γ_e due to biaxial stretching of the kerogen to accommodate the bubble. However, each bubble is surrounded by a cage formed by cross-linked segments and it is not possible to stretch these beyond their contour length L_c without breaking covalent bonds. This constraint allows us to calculate the equilibrium pressure p_b inside a bubble of radius R surrounded by the kerogen at pressure p_k , finding that it has a minimum (Fig. 3) at a characteristic radius $R^* \sim L_c$. This "foamy" pore structure remains preserved because the kerogen network eventually converts from a rubbery to a glassy state that arrests the imposed pore structure.

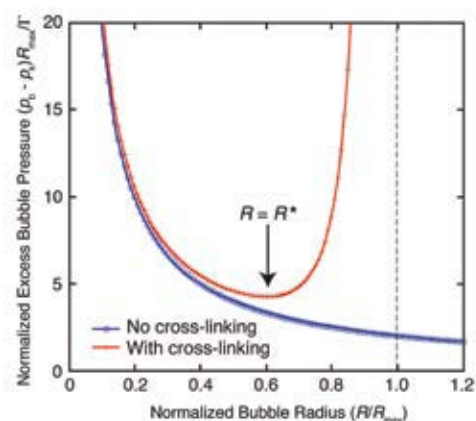


FIGURE 3: Schematic internal pressure p_k of bubbles with radius R in equilibrium with the kerogen at pressure p_k , in the absence of cross-linking (blue circles) and in the presence of cross-linking (red crosses). In the absence of cross-links, a single macro-bubble would be thermodynamically preferred, whereas cross-links favor a characteristic bubble size.

Combining model results from SANS data and direct imaging from helium ion microscopy, we conclude that shale gas samples exhibit a unique porosity component, housed in the organic component. These small pores are nearly uniform in diameter, ≈ 1.5 nm, and account for about one third of the total porosity. Building on well-established models for kerogen diagenesis, our "foamy porosity" model predicts arrested coarsening at a size determined by cross-link density, giving a diameter $O \approx 2$ nm, as observed.

References

- [1] H. E. King, Jr., A. P. R. Eberle, C. C. Walters, C. E. Kliever, D. Ertas, C. Huynh, *Energy & Fuels* **29** (3), 1375 (2015).
- [2] H. E. King, Jr., S. T. Milner, M. Y. Lin, J. P. Singh, T. Mason, *Phys. Rev. E* **75**, 021403 (2007).
- [3] A. P. Radlinski, M. A. Ioannidis, A. L. Hinde, M. Hainbuchner, M. Baron, H. Rauch, S. R. Kline, *J. Coll. Interface Sci.* **274**, 607 (2004).

A tight situation: polymer arrest in carbon nanotube networks

R. Ashkar,^{1,2} M. Abdulbaki,³ M. Tyagi,^{1,2} A. Faraone,^{1,2} P. Butler,^{1,4} and R. Krishnamoorti³



The discovery of carbon nanotubes has revolutionized the design of electronics and high-strength materials over the last few decades. These hair-like nanoparticles possess superior electrical properties, are 10 times stronger than steel and 100 times lighter – which makes them an attractive additive in common polymers, resulting in what is known as carbon nanotube (CNT) composites. Not surprisingly, CNT composites have been proposed for a variety of advanced applications from flexible electronic devices and solar panels to body armors, race cars, and next-generation commuter airplanes. These applications are based on the assumption that the inclusion of CNTs in polymer matrices would impart the superior nanotube properties to the composite material. But despite tremendous efforts, CNT composites have not fulfilled their promise yet. The caveat is that CNT dispersion in polymers usually perturbs the static and dynamic properties of the polymer matrix, and sometimes results in rather undesired properties. While most studies on nanocomposites focus on the microstructure and its effect on material performance, there is a growing awareness that the softness of these materials allows components to move around relatively easily resulting in fast dynamics that are critical to material design. The dynamics in such composites are expected to originate from particle-polymer interfacial interactions, which consequently influence longer length and time scale properties and eventually determine the success or failure of the material. Unfortunately, studying these phenomena is a challenge to conventional experimental probes due to their limited capabilities in measuring and resolving dynamics at molecular scales.

The characterization of nanoscale dynamics is even more complicated in non-dilute CNT composites prevalent in current industrial applications. Presently, the majority of such applications require CNT loadings above the percolation threshold; i.e., the concentration at which the dispersed CNTs physically touch each other and form a continuous network. In such systems, the overlap of the interfacial regions could result in complex polymer

dynamics that do not follow conventional nanocomposite theory and are thus extremely challenging to predict. The complication is exacerbated by the abundance of interface of CNTs which, in the case of strong polymer/CNT attractions, is speculated to result in significant perturbation of the adjacent polymer chains. In this context, the number of conflicting reports on the effect of interfacial interactions on dynamics begs for direct experimental observation which could distinguish between interfacial and non-interfacial polymer dynamics in these non-trivial systems.

An example of a model system that satisfies the percolation and mutual affinity conditions are composites of single wall nanotubes (SWNT) and poly(methyl methacrylate) (PMMA). Using high flux backscattering spectroscopy at NCNR, we were able to resolve the dynamics of non-interfacial from interfacial polymer segments in SWNT-PMMA composites with loadings above the SWNT percolation threshold [1]. Operated in the fixed window scan mode, this type of measurement detects the incoherent elastic scattering intensity, $I_{el}(Q)$, over an array of detectors with access to different length scales or wavevector transfers, Q (Fig. 1). The sum of intensities over the entire Q range is a measure of the fraction of effectively static entities within the sample. Entities that are slower than the instrumental resolution, i.e., ≈ 2 ns, appear static while those faster than this time frame contribute to non-elastic scattering and decrease the elastic intensity. Our composites show a slower decrease in the elastic intensities with increasing SWNT loading, consistent with a picture of transient pinning of polymer segments at the SWNT interface over time intervals longer than 2 ns. The Q -dependence of I_{el} provides a direct measure of the mean square displacements (MSD), $\langle u^2 \rangle$, of mobile hydrogen atoms through the Debye-Waller expression: $\ln[I_{el}(Q)] \propto -\frac{1}{3} Q^2 \langle u^2 \rangle$.

In the composites, this corresponds to the non-interfacial mobile polymer segments. The MSD patterns indicate a remarkable suppression of the local polymer mobility in the composites relative to pure PMMA (see Fig. 1) but do not show significant variation with SWNT loading over the wide

¹ NIST Center for Neutron Research, National Institute of Standards and Technology, Gaithersburg, MD 20899

² University of Maryland, College Park, MD 20742

³ University of Houston, Houston, TX 77204

⁴ University of Delaware, Newark, DE 19711

concentration range and resultant mesh sizes considered here. This invariability of the MSDs with the compactness of the SWNT network suggests that the fast non-interfacial segments in the composites are kinetically caged by the slow polymer domains around the nanotubes, analogous to polymer blends with fast and slow components [2].

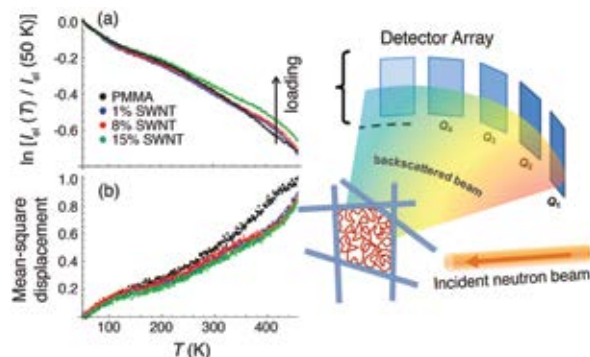


FIGURE 1: Schematic representation of the backscattering geometry with the multiple Q -value detectors allowing direct measurement of (a) total elastic intensity and (b) atomic mean square displacements.

The MSD patterns provide insights into the onset of thermally activated polymer dynamics using a simple thermodynamic model with a linear temperature dependence of $\langle u^2 \rangle$. In this framework, the crossover temperatures shown in Fig. 2 are found to be consistent with previously reported dynamical transitions in PMMA. The composites show the same transition temperatures except for ≈ 20 K increase in the highest- T crossover designating the glass transition temperature, T_g . This increase in T_g corroborates the picture of slow interfacial polymer domains in percolated SWNT networks [3] and qualitatively suggests a slowdown in the structural polymer relaxations.

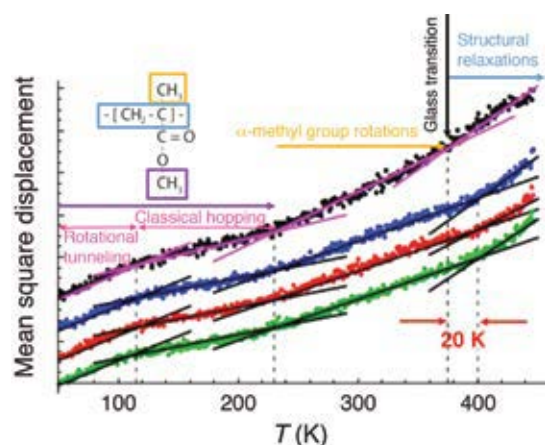


FIGURE 2: Identification of the onset of thermally activated polymer dynamics from MSD patterns based on a simple thermodynamic framework described in the text. The color scheme is the same as in Fig. 1.

A quantitative measurement of the structural relaxations was possible through complementary neutron spin-

echo spectroscopy (NSE), which can be selectively tuned to Q -values at which structural relaxations are most prominent. The values of the relaxation times, τ_R , obtained from fits of the decay rates to a stretched-exponential model, reveal an order of magnitude slowdown of the polymer dynamics in the SWNT composites compared to pure PMMA. However, both pure and composite samples show similar linear trends in the relaxation process (over the NSE time-window) manifested in almost identical activation energies, $E_A \approx 38.5 k_B T$. This implies that the energy barrier required for structural polymer relaxations is not disrupted by the inclusion of the nanotubes. But, due to chain connectivity, the local pinning of chain segments at the interfaces results in a dramatic slowdown of the structural relaxations that occur at longer length/time scales.

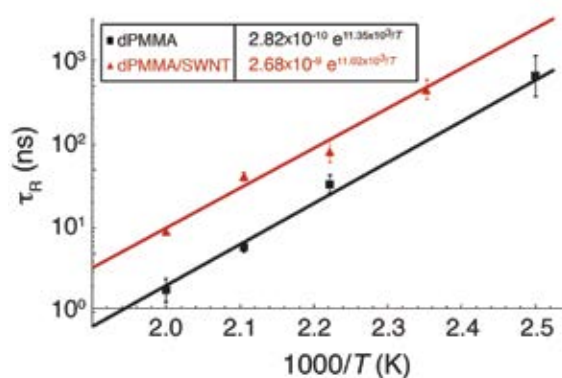


FIGURE 3: Structural relaxation times measured by NSE show an order of magnitude slowdown in polymer dynamics in the SWNT composite (volume fraction of 8 %) compared to neat PMMA.

In conclusion, the implementation of different neutron scattering spectroscopy techniques provides a clear picture of polymer dynamics in an industrially favored class of CNT nanocomposites characterized by percolated nanotube networks and strong polymer-CNT attractions. Backscattering measurements allow a distinction between the transient pinned interfacial segments and the mobile segments away from the interface while NSE measurements clarify the long-range effect of these pinning events. In addition to their value to the design of CNT composites with tailored properties and reliable long-term performance, these findings should help guide theories and simulations of hierarchical polymer dynamics in a broad class of nanocomposites.

References

- [1] R. Ashkar, M. Abdul Baki, M. Tyagi, A. Faraone, P. Butler, R. Krishnamoorti, *ACS Macro Letters* **3** (12), 1262 (2014).
- [2] M. Tyagi, A. Arbe, J. Colmenero, B. Frick, J. R. Stewart, *Macromolecules* **39**, 3007 (2006).
- [3] D. Long, F. Lequeux, *Eur. Phys. J. E* **4**, 371 (2001).

Architectural paints: from hierarchical structure to rheology

A. K. Van Dyk¹, T. Chatterjee², V. V. Ginzburg², and A. I. Nakatani³

nSoft



A commercial paint exhibits a desired viscosity profile over shear rates from $\approx 10^{-5} \text{ s}^{-1}$ for settling to $> 10^4 \text{ s}^{-1}$ for brushing, rolling, and spray applications. In general, the composition and chemistry govern the formulation microstructure. Due to formulation complexity, a full understanding of the fundamentals of paint rheology is still somewhat elusive, but has been attributed to changes in the flow-induced hierarchical structure existing in the paint. In this work, we have utilized ultra small-angle neutron scattering under shear (rheo-USANS) to study structural evolution of paints. Employing the structural parameters obtained from the scattering data, we developed an elementary viscosity expression that demonstrated good agreement between measured and calculated flow curves.

In typical paint formulations, the volume fraction of solids ranges from about 15 % to 45 %, with about 5 % to 35 % of the volume being polymeric latex binders. The rest of the solids are primarily inorganic pigment particles (TiO_2 and extender). To achieve the desired viscosity profile over a wide shear rate range, rheology modifiers (RMs) such as hydrophobically modified ethylene oxide urethane (HEUR) polymer are widely used in the coatings industry. HEUR polymers are nonionic, associative thickeners consisting of a hydrophilic poly(ethylene oxide) (PEO) backbone and hydrophobes [1]. Structural studies of commercially relevant paints in the wet state have been difficult to accomplish due to the opacity of the suspensions, relatively high volume fraction of solids, presence of different types of particles (e.g. latex and TiO_2) and relatively large and polydisperse particle sizes (100 nm to 10 μm).

Here, in-situ rheo-USANS measurements were performed at the BT-5 Perfect Crystal Diffractometer USANS instrument using the NIST couette shear cell. USANS data is slit smeared, meaning that there is poor resolution in the vorticity direction. Therefore, the structural parameters obtained from the rheo-USANS data are more representative of the structure in the flow direction. Additionally, we used contrast matching where the neutron scattering length density of the suspending medium

($\text{H}_2\text{O}/\text{D}_2\text{O}$ mixture) is matched to either the latex or pigment. This permits probing the shear dependence of the TiO_2 aggregate and latex binder particle aggregate structures independently [2].

Representative rheo-USANS data from a selected paint formulation (at two contrast match conditions) as a function of shear rate are presented in Figs. 1a and 1b. Correlation length, ξ , and self-similarity dimension or fractal dimension, D_f , characterize latex and TiO_2 aggregates. Under shear, the large fractal aggregates of latex and TiO_2 are expected to be restructured and broken into smaller fractal aggregates and finally into single particles at sufficiently high shear rate.

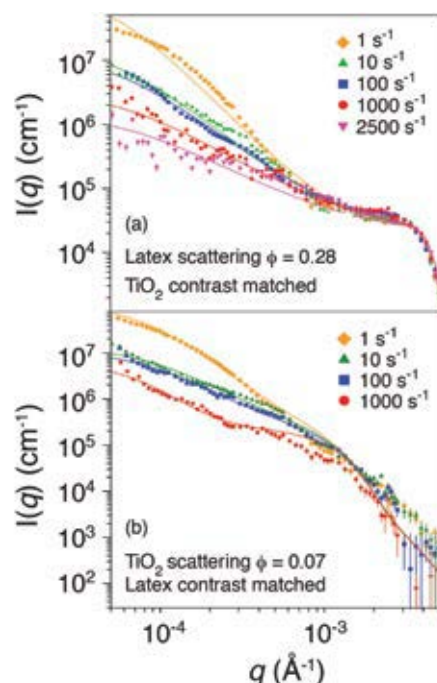


FIGURE 1: Rheo-USANS intensity profiles as a function of the scattering vector q for the Paint-1 formulation at (a) TiO_2 contrast matched condition and (b) Latex-A1 contrast matched condition, for different shear rates. The solid lines are model fits [2] to the experimental data.

Sketches qualitatively depicting latex and TiO_2 aggregate structures at various applied shear rates for two selected paints are presented in Fig. 2. The sketches mimic aggregates with a D_f and an aggregate R_G ($\approx \xi$) extracted

¹Dow Coatings Materials, The Dow Chemical Company, Collegeville, PA 19426

²Materials Science and Engineering, The Dow Chemical Company, Midland, MI 48674

³Analytical Sciences, The Dow Chemical Company, Collegeville, PA 19426

from rheo-USANS fitting. Aggregate orientation should not be construed to infer anisotropy. These schematics represent the time-averaged steady state aggregate structure where the time scale is orders of magnitude greater than both the aggregate-aggregate and aggregate-particle collision timescales. Paint-1 was formulated with a RM that has a relatively smaller hydrophobe size ($C_m \approx 12$) and a lower hydrophobe density. A smaller hydrophobe size results in a shorter relaxation time and consequently, aggregates are softer and deformation dominates (maintain cohesion under stretching). Under increasing shear, the latex aggregate structures evolve into more open structures (D_f decreases, resulting in diffusion limited aggregation, DLA-type structures), while the correlation length remains approximately constant. In contrast, Paint-3 has a larger hydrophobe ($C_m \approx 18$) and a greater hydrophobe density (>3). These latex aggregates are expected to form more rigid reaction limited aggregation, RLA-type structures.

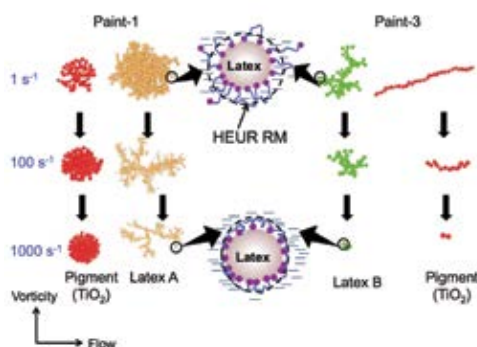


FIGURE 2: Qualitative schematics of aggregate structures based on rheo-USANS and rheo-SANS fitting parameters [1, 2]. Very small aggregates have been enlarged for better visibility. Flow and vorticity orientation is shown for the SANS latex-RM schematics but is not applicable to the USANS schematics.

The TiO_2 aggregate sizes in Paint-1 are much larger than the TiO_2 single particle size and the fractal dimensions indicate RLA-type structures, and therefore large numbers of particles are present in each aggregate even at high shear. In contrast, at low shear the TiO_2 aggregate fractal dimensions for Paint-3 are low, while the correlation lengths are much larger than the single particle radius, indicating the formation of strand-like aggregates. At high shear, these strand-like aggregates break into smaller aggregates and approach almost single TiO_2 particles. In passing, we mention that the TiO_2 dispersion state has a profound impact on the opacity of the film cast from these formulations.

The steady-shear viscosity of aggregate structures in colloidal suspensions is the sum of two main contributions – hydrodynamic and structural. Previously [1], we have shown that the latex-RM combination forms a core-

shell microstructure where the shell layer becomes anisotropic at high shear (with major axis along the vorticity direction) (Fig. 2). However, the latex-RM microstructure hydrodynamic volume contribution, based on the hard-sphere approach of Krieger and Dougherty [3] alone cannot account for the observed paint viscosity. Knowing the precise structural parameters of the transient soft colloidal aggregates, we developed a scaling model where the structural contribution is modeled after the Rouse model for polymer solutions. Others [4, 5] have also emphasized similarity between Rouse-mode relaxation and equations of motion for weakly associated colloids. While each structural parameter (latex transient aggregates and individual particles as well as TiO_2 transient aggregates and individual particles) contributes to the total viscosity, the dominant contribution arises from the latex transient aggregates [2]. This leads to a single-parameter approximate expression for viscosity

$$\eta \cong \eta_s \alpha_{\text{latex}} \phi_{\text{fractal latex}} \left(\frac{\xi_{\text{latex}}}{\langle R \rangle_{\text{latex}}} \right)^{D_f \text{ latex}}$$

In this description η is the solvent viscosity; ϕ is the volume fraction; ξ and D_f are the transient aggregate structural dimensions; and $\langle R \rangle$ is the fractal aggregate building-block dimension. The parameter α is a fitting parameter of $\approx O(1)$. Using such a simple expression, good agreement between measured and calculated viscosity was obtained as demonstrated in Fig. 3. This implies that structural parameters extracted from the scattering data are representative of the formulation structure under shear and that energy dissipation from transient fractal aggregates of latex is the predominant mechanism of viscosity creation in HEUR thickened latex paints.

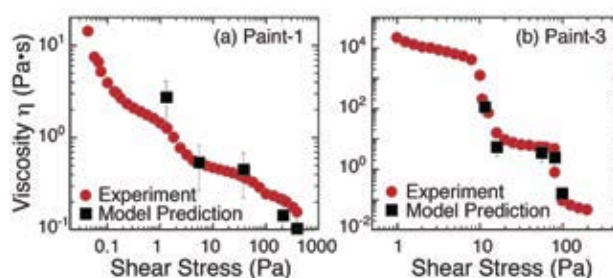


FIGURE 3: Calculated viscosity and comparison with experimentally measured values as a function of shear stress for a) Paint-1 and b) Paint-3.

References

- [1] T. Chatterjee, A. K. Van Dyk, A. I. Nakatani, *Macromolecules* **47** (3), 1155 (2014).
- [2] A. K. Van Dyk, T. Chatterjee, V. V. Ginzburg, A. I. Nakatani, *Macromolecules* **48** (6), 1866 (2015).
- [3] I. M. Krieger, T. J. Dougherty, *J. Soc. Rheol.* **3**, 137 (1959).
- [4] A. West, J. Melrose, R. Ball, *Phys. Rev. E* **49** (5), 4237 (1994).
- [5] T. C. B. McLeish, T. Jordan, M. T. Shaw, *J. Rheol.* **35** (3), 427 (1991).

Enhanced vertical ordering of block copolymer films by tuning temperature and molecular mass

A. Modi¹, X. Zhang², K. Yager³, J. F. Douglas⁴, S. Satija⁵, and A. Karim¹

Block copolymers (BCPs) are an important class of soft polymeric materials that are comprised of two or more different polymers ("blocks") that are chemically bound at junction points. In most cases, the polymer blocks tend to be spatially segregated rather than mixed due to repulsive interactions between blocks, and their collective ordering behavior results in self-organized assembly of a wide range of morphologies (of one block surrounded by a matrix of the other block). BCP morphologies can range from spheres to cylinders to lamellae to gyroid and other exotic morphologies. These morphologies can be highly periodic with varying degrees of connectivity and structural dimensions on the nanometer scale, typically on the order of 5 nm to 100 nm. These materials have the potential to be used in a wide variety of applications ranging from ultrathin membranes for water purification, to high-density data storage devices, to next generation transistors and optical devices. From a fundamental viewpoint, the ordering of block copolymers via self-assembly into periodic nanoscale structures is intriguing due to a complex interplay of block-block molecular interactions and molecular packing considerations.

In BCP thin films a high degree of control in the alignment of nanodomains is essential to utilize these materials as nanoscale templates for various top-down or bottom-up approaches to nano-fabrication. It is critical then to investigate the effect of molecular weight of the block components, the effects of annealing temperature on their film ordering properties, and other properties that affect the molecular scale ordering. In this regard, when BCPs are confined to thin films, their ordering behavior is significantly influenced by the interfacial interactions with confining boundaries. For instance, strong attraction of one of the blocks to the substrate can lead to preferential wetting of the block, which can not only change the morphology from that observed in the bulk but also alter the orientation of the block with respect to the substrate [1, 2]. In these examples, the control of orientation and morphology is much more challenging as boundary interactions may be controlled

by modification of the substrate surface or by altering the block chemistry during the synthesis process, both of which are often undesirable. It would thus be convenient to be able to tune an inherent molecular or processing parameter to avoid such undesirable surface effects. This forms the scientific basis and theme of this study.

Cylinder-forming BCPs may be used for applications such as membranes for filtration by virtue of the ability to optically and chemically etch the minority cylinder-forming block to create a high density of nanochannels for selective material transport. Membranes and other applications such as data storage require that the cylinders be oriented perpendicular to the substrate. However this only occurs if there is no significant energetic preference of either of the two blocks for the substrate or air interfaces, criteria, which are often difficult to satisfy. In thin films, it is generally observed that cylinder-forming PS-*b*-PMMA BCPs preferentially orient with the cylinders in a horizontal arrangement due to the energetic preference of the PMMA component for the oxide (plasma-treated) silicon wafer substrate. However, these measurements have mostly been conducted at relatively high temperatures, typically 180 °C and higher.

Scaling arguments predict an orientational transformation from cylinders oriented parallel to the supporting substrate to a perpendicular configuration when the polymer surface energy driving the BCP surface pattern formation is large, exactly the phenomena we examined here. Previously, we observed such a transformation in poly(styrene-*b*-methyl methacrylate) (PS-*b*-PMMA) copolymer thin films, and demonstrated that cylinder-forming BCPs have a rich "surface morphology diagram" delineating how the BCP surface morphology depends on ordering temperature, film casting method, and film thickness [3]. In recent work on BCP lamellae, we also found that decreasing the temperature helped achieve perpendicular lamellae orientation, provided the 'rough' boundary interaction at the substrate is made nearly neutral [2]. This allowed a tuning of the amount of BCP domains standing normal to the solid

¹Department of Polymer Engineering, University of Akron, Akron, OH 44325

²Center for Soft Condensed Matter Physics and Interdisciplinary Research, Soochow University, Suzhou 215006, China

³Center for Functional Nanomaterials, Brookhaven National Laboratory, Upton NY

⁴Materials Measurement Laboratory, National Institute of Standards and Technology, Gaithersburg, MD 20899

⁵NIST Center for Neutron Research, National Institute of Standards and Technology, Gaithersburg, MD 20899

substrate by varying temperature. This report considers a similar strategy of enhancing the ordering in cylinder-forming BCP films where we increase the thermodynamic driving force for ordering by either decreasing temperature or by increasing the BCP molecular mass to drive a vertical orientation of cylinders, overcoming substrate surface interactions that lead to orientation parallel to the substrate. Since the molecular block-block interaction parameter χ is inversely temperature dependent, this demonstrates that tuning the Flory-Huggins (F-H) interaction strength χ_N (N = number of monomers in BCP) provides control, allowing the formation of well-ordered surface patterns with the technologically interesting perpendicular cylinder BCP orientation [4]. This effect arises because the segregation strength χ_N controls the effective rigidity of self-assembled BCP structures.

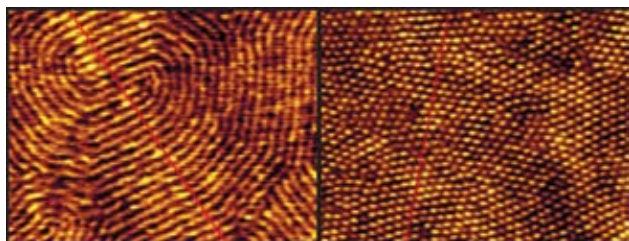


FIGURE 1: Tunability of BCP orientation with temperature. AFM height images for PS-PMMA BCPs with $M_w = 77.5$ kg/mol. Left image: Film thickness $h_f = 141$ nm annealing at 200°C for 15 h. Right image: $h_f = 94$ nm annealed at 164°C for 15 h. The scale bar is 200 nm, and applies to both images. One-dimensional height traces indicated by a red line used to calculate aspect ratio of surface structures. Image widths are $1.5\ \mu\text{m}$.

Figure 1 shows that in PS-*b*-PMMA thin films with a total relative molecular mass of 77.5 kg/mol and a mass fraction of PS of 0.74 (cylinder bulk phase), we obtain a traditional parallel cylinder orientation at relatively high temperatures ($\approx 200^\circ\text{C}$), however the morphology switches to vertically oriented cylinders at low temperature ($\approx 164^\circ\text{C}$). In other words, as we lower the temperature, the interfacial segregation strength (χ) increases, leading to a transition between the two orientations. We rule out temperature dependent surface tension differences as driving this transition as the surface tension difference increases at lower temperature. The system would form wetting layers of polymer morphology, which is not observed.

Neutron reflection studies (Fig. 2) confirm the parallel orientation of cylinders when annealed at the relatively high temperature of 200°C . An oscillatory average depth profile is observed due the hexagonally packed cylinders in the thin film that appear layered on the substrate, as seen in Ref. [1].

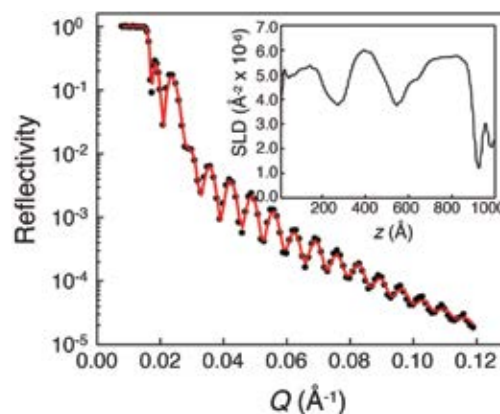


FIGURE 2: Neutron reflectivity measurements on dPS-*b*-PMMA films with a perpendicular cylinder morphology at the surface. NR scans (symbols) measured from a 96 nm flow-coated BCP film annealed at 200°C for 15 h.

We next consider the same effect by increasing the molecular mass, in which our relatively low molecular mass BCPs have a parallel orientation at $\approx 180^\circ\text{C}$. If our interpretation of orientation dependence on interaction strength is correct, this should allow us to observe a parallel to perpendicular orientation, even at elevated temperature. Figure 3 shows the vertical orientation of PS-*b*-PMMA cylinders at 182°C for high molecular weights of PS-PMMA BCPs ($M_w = 158.0$ kg/mol and 367.2 kg/mol). Thus we confirm that, as with low temperature vertical orientation cylinder forming PS-*b*-PMMA BCP films, we can achieve tunable vertical alignment of the PMMA cylinders on the substrate by enhancing the strength of the thermodynamic driving force for BCP ordering by simply increasing the BCP molecular mass, since the F-H product χ_N is the controlling parameter.

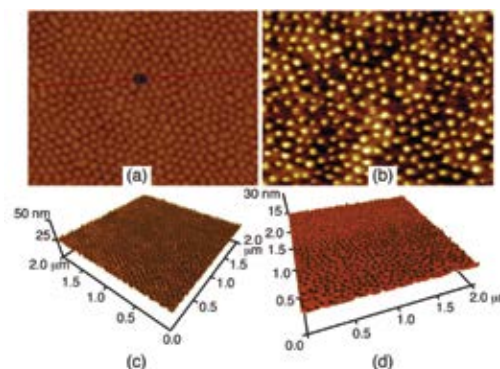


FIGURE 3: AFM height images for PS-PMMA BCPs with $M_w = 158.0$ kg/mol (left) and 367.2 kg/mol (right). Representative images of BCP films with (a) $h_f = 54$ nm annealed at 182°C for 15 h, (b) $h_f = 165$ nm annealed at 182°C for 15 h, (c and d) 3D view of (a and b). All panels are $2\ \mu\text{m}$ wide.

References

- [1] A. Karim *et al.*, J. Chem. Phys. **100** (2), 1620 (1994).
- [2] K. Yager *et al.*, Soft Matter **11**, 5154 (2015).
- [3] X. Zhang *et al.*, ACS Nano **2** (11), 2331 (2008).
- [4] X. Zhang *et al.*, RSC Adv. **5**, 32307 (2015).

Wide-angle neutron collection using a defocusing Rowland geometry

L. Harriger¹, and I. Zaliznyak²

Analyzer-detector multiplexing has become standard in the design of triple axis neutron spectrometers and can generate roughly an order-of-magnitude increase in data collection rate [1, 2]. Although the throughput is essentially determined by the total area of analyzer crystal, the true efficiency is limited due to the need to both eliminate cross-talk between different analyzer-detector channels and mitigate a sharp increase in background associated with the reduced shielding associated with wide-angle neutron collection.

Rowland focusing geometry [3] is traditionally used to flatten a large scattering angle (A_4) range into a single point by generating a monochromatic sample image at the detector position (horizontal focusing, Fig. 1a). An alternative approach is to use a monochromatic Rowland defocusing geometry, where the sample image is transferred to a position away from the detector and then viewed by a PSD through a radial collimator (Fig. 1b). Here, the individual analyzer blade rotations select out a desired E_f , while the collective blade group rotation (A_5) selects a Rowland circle that matches the sample image to the collimators focal length. Thus, Rowland defocusing identifies A_5 as a free parameter with a singular setting that enables the use of a radial collimator. Although energy dispersive setups have formerly provided collimated configurations, they typically produce irregular PSD trajectories through the 3D (Q, ω) volume that cannot easily be tuned to match the $S(Q, \omega)$ region of interest. However, Rowland defocusing results in a constant energy scan across the PSD, thereby decoupling Q and ω . As a result, the energy transfer can be freely selected and a much simpler PSD trajectory is then projected into the 2D scattering plane.

Ray tracing across the multiplexed assembly [4] (Fig. 1c), we find that the A_5 Rowland defocusing value is situated almost ideally for minimizing both beam depletion and A_4/E_f value mixing, while simultaneously optimizing the A_4 and PSD coverage. As a result, a 'resolved' horizontal focusing can be achieved by integrating a PSD in the Rowland defocusing geometry; providing similar intensity gains and Q -relaxation as traditional horizontal focusing but without the same information loss (Fig. 1c).

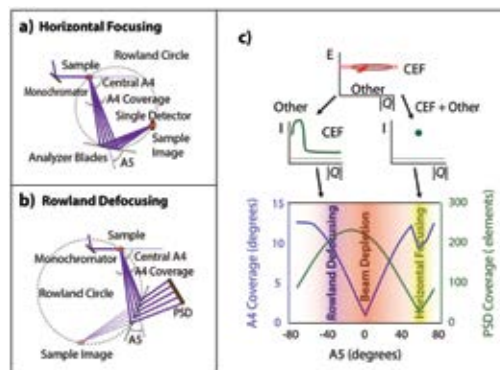


FIGURE 1: a) Application of the Rowland geometry to horizontal focusing with a single detector. b) Application of the Rowland geometry to Rowland defocusing with a PSD. c) A_5 parameter space for the fixed- E_f geometry.

A wide angle, next-generation spectrometer design based on the Rowland defocusing geometry can be realized by densely packing the Rowland circle with analyzer blades which provide an $\approx 150^\circ$ quasi-continuous sampling of A_4 (Fig. 2a). In a second design (Fig. 2b), the sample can be separated into a prismatic line of sample images by stacking multiple wide angle Rowland assemblies together thereby allowing simultaneous measurement of multiple E_f s over A_4 ranges between 60° to 90° . Rowland focusing is thus readily applicable to multiplexed triple axis spectroscopy with no required modification to design while also opening the door to next-generation spectrometers that fully leverage the power of this technique.

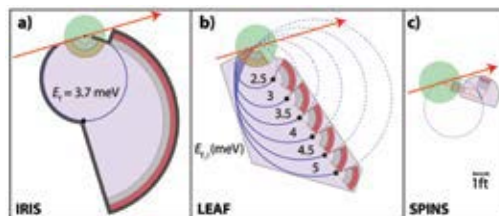


FIGURE 2: a) Wide angle Rowland defocusing design with a single E_f sampling. b) Wide angle Rowland defocusing design with multiple E_f sampling. c) To-scale comparison of designs to the SPINS spectrometer.

References

- [1] I. Zaliznyak *et al.*, *Modern Techniques in characterizing Magnetic Materials* (2005).
- [2] J. W. Lynn *et al.*, *Journal of Research of NIST* **117**, 61 (2012).
- [3] H. A. Rowland, *Philosophical Magazine Series 5* **16**, 197 (1883).
- [4] Results generated using the Matlab library PSD_Planner; leland.harriger@nist.gov

¹ NIST Center for Neutron Research, National Institute of Standards and Technology, Gaithersburg, MD 20899

² Brookhaven National Laboratory, Upton, NY 11973

Measurement and modeling of polarized specular neutron reflectivity in large magnetic fields

B. B. Maranville¹, B. J. Kirby¹, A. J. Grutter¹, P. A. Kienzie¹, C. F. Majkrzak¹, and Y. Liu²

Polarized specular neutron reflectometry measurements require a relatively small applied magnetic field throughout the apparatus to maintain a well-defined quantization axis of the neutron spin. Often, a larger field is also applied at the sample position to manipulate the magnetic state of the sample. The difference in the Zeeman energy for a spin-up vs. a spin-down neutron leads to observable shifts in the scattering for even modest applied fields (10s of mT) when spin-flip (SF) scattering is appreciable [1]. The reflectivity formalism including the Zeeman term has been only briefly described in the literature [2, 3].

These shifts are not a major concern in many experiments [3] because the effect is significant only when there is both a large applied field and strong SF scattering. However, there are important cases where accounting for the Zeeman shift is necessary; e.g., in advanced recording media with high magnetic anisotropy the sample magnetization is not parallel to even large applied fields.

In purely elastic scattering, energy conservation leads to a field-dependent angular shift in the reflected SF beams. The momentum k_z for the SF reflections is then magnetic field B -dependent in the fronting medium:

$$\left(k_{F,z}^{+,-}\right)^2 = \left(k_{F,z}^{\pm}\right)^2 + 8\pi\rho_{F,B} \quad (1) \quad \left(k_{F,z}^{-,+}\right)^2 = \left(k_{F,z}^{\pm}\right)^2 - 8\pi\rho_{F,B} \quad (2)$$

$$\rho_{F,B} = \frac{2\mu_n m B}{4\pi\hbar^2} \approx B \times 2.316 \times 10^{-6} \text{ \AA}^{-2} \text{ T}^{-1} \quad (3)$$

The non-SF k_z are not shifted. In the Schrödinger equations that describe the spin-polarized neutron wave propagation, the energy must also include the magnetic potential, nuclear potential, and kinetic energy, which will be different for the (+) and (-) incident neutron spin.

$$\left[\frac{-\hbar^2}{2m} \frac{\partial^2}{\partial z^2} \hat{1} + \hat{V}(z) - E_{F,z}^i \hat{1} \right] \begin{pmatrix} \psi^{i,+} \\ \psi^{i,-} \end{pmatrix} = 0 \quad (4)$$

$$E_{F,z}^{\pm} = \frac{\hbar^2}{2m} \left[4\pi(\rho_{F,N} \pm \rho_{F,B}) + (k_{V,z})^2 \right] \quad (5)$$

Here the ρ terms are the nuclear and magnetic scattering length densities and E is the energy in the fronting medium. This inclusion of the Zeeman energy term in the total energy is how the current calculations differ from previous ones.

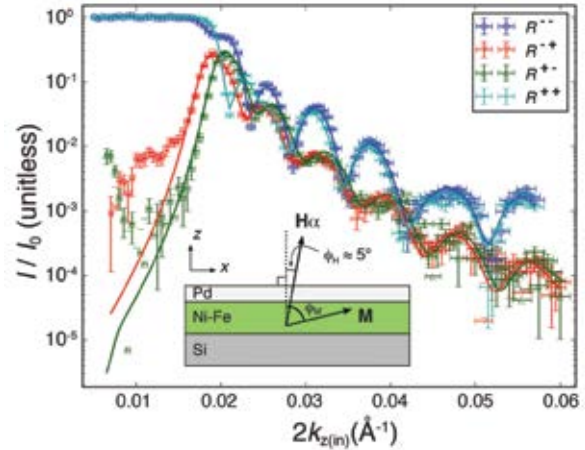


FIGURE 1: Data and modeling for the example system. Inset: test sample geometry.

To demonstrate the effects described above, we measured the polarized reflectivity from a magnetically soft thin film, taking advantage of the shape anisotropy to achieve a large magnetization non-collinear with the nearly perpendicular applied field. Measurements were carried out on the Polarized Beam Reflectometer. All 4 spin cross-sections were measured at 3 different detector angles for each sample angle to capture the shifted SF scattering described by Eqs. 1 and 2. The two non-SF cross-sections were extracted from the standard unshifted configuration in which the detector angle equaled twice the sample angle. The two SF cross sections were obtained from detector positions shifted higher and lower. The results are shown in Fig. 2 along with a fit [4] using a newly updated version of the Refl1D software [5], which now includes the Zeeman energy corrections described in this work.

Users now have access to predefined routines for configuring the instrument to collect Zeeman-shifted scattering data at relevant angles for any applied field, and can accurately model their data with Refl1D, creating new opportunities for polarized reflectivity measurements on samples with high anisotropy.

References

- [1] G. Felcher *et al.*, Nature **377**, 409 (1995).
- [2] R. van de Kruijs *et al.*, Physica B: Cond. Matt. **283**, 189 (2000).
- [3] Y. Liu *et al.*, Phys. Rev. B **83**, 174418 (2011).
- [4] B. B. Maranville, B. J. Kirby, A. J. Grutter, P. A. Kienzie, C. F. Majkrzak, Y. Liu, submitted to J. Appl. Cryst. (2015).
- [5] Refl1D download: <http://ncnr.nist.gov/refl1d>

¹NIST Center for Neutron Research, National Institute of Standards and Technology, Gaithersburg, MD 20899

²Quantum Condensed Matter Division, Oak Ridge National Laboratory, Oak Ridge, TN 37831

A far-ultraviolet neutron observatory

M. A. Coplan¹, A. L. Kowler¹, C. M. Lavelle², A. K. Thompson³, R. E. Vest³, and C. W. Clark⁴

A novel far-ultraviolet (FUV) neutron detector has been commissioned on beamline NG6m. It is the core element of a “Neutron Observatory” that will deliver real-time neutron fluence data to users of the NCNR in a simple format, and provide a stable platform for helium-free neutron detector development.

Our neutron detector was developed during research on alternatives to ³He neutron detection conducted at the NIST Center for Neutron Research, the Center for Nanoscale Science and Technology, and SURF III Synchrotron Ultraviolet Radiation Facility. The basic detection mechanism is briefly summarized as follows; more detailed accounts may be found in Refs. [1] and [2].

The detector is based on neutron absorption by the isotope ¹⁰B. Figure 1 shows a silicon substrate plated with a micron-thick film of isotopically enriched ¹⁰B, mounted in a reaction cell. In operation, the cell is filled with a noble gas (Ar, Kr, or Xe) at approximately atmospheric pressure, and neutrons enter the cell from the left. Absorption of the neutrons by ¹⁰B produces alpha particles and ⁷Li nuclei with MeV energies. The energetic particles then react with the background noble gas and produce diatomic noble gas molecules in electronically excited states, commonly known as “excimers.” Once formed, the excimers quickly dissociate into free atoms accompanied by emission of photons with wavelengths of 120 nm to 180 nm, which lie in the far ultraviolet range of the electromagnetic spectrum. Tens of thousands FUV photons are produced for each neutron absorption reaction [3, 4] implying that about a third of the entire nuclear reaction energy is converted into FUV photons. Moreover, the photons are emitted in bursts over intervals of tens of nanoseconds.

Taking full advantage of this remarkably efficient coupling of neutrons to the electromagnetic field led to the development of a stable and accurate FUV detection system where the photon bursts are detected with a FUV-sensitive photomultiplier tube, that views the structure of Fig. 1 looking down from the top of the figure. The photon bursts are converted to electron pulses by the photomultiplier. A microcontroller supplies high voltage to the photomultiplier, monitors noble gas pressure, integrates

the photomultiplier output bursts into single data pulses, processes the data to obtain absolute neutron fluence rates, and transmits the results to a conventional computer for distribution on the internet.

The advantages of the Neutron Observatory are simplicity (the only active elements are the stable ¹⁰B films and noble gases), efficient, robust operation resulting from the high photon production, and traceable absolute calibration (the cross sections for the ¹⁰B absorption of neutrons are known with high accuracy). An interface has been designed to provide NCNR operational information to users, and to support research in alternative neutron target architectures and photon conversion mechanisms.

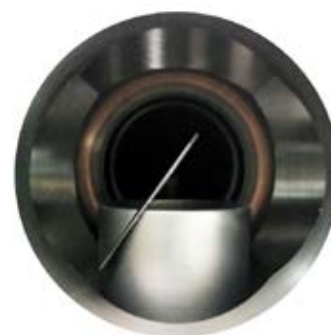


FIGURE 1: Photograph of the reaction chamber of the neutron detector. The neutron target is a thin film of isotopically-enriched ¹⁰B deposited on a 2.5 cm square silicon substrate and positioned at 45° with respect to the incident neutron beam that enters the reaction chamber from the left. The chamber is filled with a noble gas at approximately atmospheric pressure. As described in the text, energetic products of the ¹⁰B - neutron absorption reaction excite far ultraviolet photon emission in the noble gas. The photons are detected by a photomultiplier tube, which views the face of the target from a position a few cm above the top of the present figure.

References

- [1] C. W. Clark, P. P. Hughes, M. A. Coplan, A. K. Thompson, R. E. Vest, U.S. Patent No. 8,816,296, (2014).
- [2] C. M. Lavelle, M. Coplan, E. C. Miller, A. K. Thompson, A. L. Kowler, R. E. Vest, A. T. Yue, T. Koeth, M. Al-Sheikhly, C. W. Clark, *Appl. Phys. Lett.* **106**, 094103 (2015).
- [3] P. P. Hughes, M. A. Coplan, A. K. Thompson, R. E. Vest, C. W. Clark, *Appl. Phys. Lett.* **97**, 234105 (2010).
- [4] J. C. McComb, M. A. Coplan, M. Al-Sheikhly, A. K. Thompson, R. E. Vest, C. W. Clark, *J. Appl. Phys.* **115**, 144504 (2014).

¹University of Maryland, College Park, MD 20742

²The Johns Hopkins University Applied Physics Laboratory, Laurel, MD 20723

³National Institute of Standards and Technology, Gaithersburg, MD 20899

⁴Joint Quantum Institute, National Institute of Standards and Technology and University of Maryland, Gaithersburg, MD 20899

Extensional-flow SANS of wormlike micelles

R. McAllister¹ and K. M. Weigandt²

nSoft

Non-shear flows are commonly observed in industrial processing of complex fluids. Examples of extensional flow include the delivery of pharmaceuticals via syringe and hypodermic needle and extrusion or molding of polymer melts. Despite the frequency with which complex fluids experience extensional stresses, the structure and rheology of complex fluids undergoing extensional flow remains relatively understudied when compared to shear flow.

An extensional flow cell platform with eight access ports (four per side) has been developed such that customizable inserts can be quickly exchanged providing flexibility in experiment design (Figure 1a) [1]. This flow cell is currently available to the general SANS user community. In a cross-slot flow cell two opposing fluid fronts split evenly into outlet ports perpendicular to the inlet (Figure 1b). At the center there is a stagnation point where the flow velocity is zero and the fluid experiences purely extensional strain. To maximize scattering, while primarily measuring the effects of extensional strain, a 1 mm diameter sample aperture centered at the stagnation point is used.

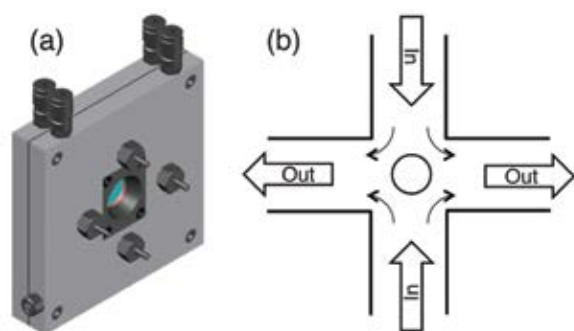


FIGURE 1: (a): schematic of flow cell, (b): diagram depicting cross-slot flow.

To demonstrate its capabilities, our initial measurements focus on measuring the alignment of wormlike micelle solutions (WLMs). The WLMs contain 75 mmol/L cetylpyridinium chloride and 45 mmol/L sodium salicylate. Four cross-slot inserts, 2 mm wide and ≈ 1 mm, 2 mm, 3 mm, and 5 mm deep were used. Additionally, a 10 mm wide and 1.6 mm deep insert was also used to more closely simulate the devices used in earlier SANS measurements [2]. Since the WLMs approximate plug like flow, a nominal extensional rate ($\dot{\epsilon}$) can be calculated as Q/w^2d where Q is the volumetric flow rate, w is the cross-slot width and d is

the channel depth [3]. Annular averages ($q = 0.03 \text{ \AA}^{-1}$) of the reduced data were fit with an even Legendre expansion to determine the orientation parameter (P_2) and the direction of alignment (ϕ).

P_2 and ϕ are plotted as a function of $\dot{\epsilon}$ in Figure 2. WLMs start to exhibit alignment in the direction of extensional strain at $\dot{\epsilon} > 0.1 \text{ s}^{-1}$ and P_2 increases monotonically until $\dot{\epsilon} \approx 0.8 \text{ s}^{-1}$. At $\dot{\epsilon} > 0.8 \text{ s}^{-1}$, the orientation direction begins to shift and there is a sharp reduction in the degree of alignment for most cross-slots. These changes indicate that the fluid from each inlet is no longer splitting evenly into the side channels thus eliminating the stagnation point. The low aspect ratio ($H/W = 0.16$) requires order of magnitude higher linear flow velocity to achieve equivalent $\dot{\epsilon}$ relative to the high aspect ratio ($H/W = 2.5$) channels. In this case, the degree of alignment increases substantially upon loss of the stagnation point due to greater local shear stresses. However, for WLMs that can be approximated as having plug-like flow, it seems that the measurement of extensional effects (prior to the onset of instabilities) is not significantly affected by the cross-slot aspect ratio.

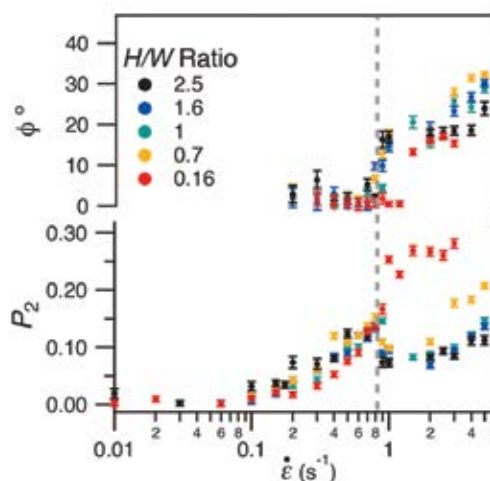


FIGURE 2: Orientation parameter and alignment angle plotted as a function of nominal extensional strain rate for WLMs in a series of cross-slot flow cells.

References

- [1] K. M. Weigandt, R. McAllister, in preparation (2015).
- [2] J. Penfold, I. Tucker, *J. Phys. Chem. B*, **111** (32), 9496 (2007).
- [3] S. J. Haward, *et al.*, *Soft Matter*, **8**, 536 (2012).

¹ University of Delaware, Newark, DE 19716

² NIST Center for Neutron Research, National Institute of Standards and Technology, Gaithersburg, MD 20899

Design and installation of a new instrument for prompt gamma-ray activation analysis

R. L. Paul¹, D. Şahin², J. C. Cook², C. Brocker², R. Zeisler¹, and R. M. Lindstrom¹

Prompt-gamma activation analysis (PGAA) is used to determine chemical composition by measuring gamma radiation emitted by samples during neutron capture. PGAA is especially useful for measurement of light elements (in particular hydrogen and boron) for which optical spectroscopy is limited. An instrument for cold neutron PGAA, located on neutron guide NG7 from 1990 to 2014, was used for multielement characterization of a wide variety of materials, including metals and metal alloys, semiconductor and superconductor materials, fullerenes and their derivatives, and geological and biological samples [1-3]. Because of its hydrogen-free construction the detection limit for hydrogen was < 5 mg/kg in most matrices. However, the presence of an adjacent guide near the sample position, resulted in increased gamma-ray background, and placed limitations on both sample size and experimental space.

In response to the limitations of the NG7 instrument, a new PGAA instrument has been installed at neutron guide NGD as part of the recent NCNR expansion [4]. To minimize neutron and gamma-ray background, shielding was modeled with the help of the Monte Carlo N-Particle (MCNP) code [5]. The current design of the instrument begins at a ⁶Li-glass local beam shutter opening to emit the neutron beam through an evacuated flight tube into the adjoining PGAA sample chamber. The inside of the flight tube and chamber are lined with lithiated shielding to prevent gamma-ray background arising from capture of scattered neutrons, with ⁶Li glass inside the chamber as a beam stop. Prompt gamma rays emitted by the sample are measured using an n-type Ge detector mounted vertically into a bismuth germanate (BGO) Compton shield which improves the signal-to-noise ratio. The detector is shielded with lead to minimize gamma-ray background from all sources except the sample and with borated polymer to mitigate fast neutrons, produced by thermal neutron capture in ⁶Li, that could damage the detector.

The thermal equivalent neutron flux at the sample position has been measured as $6.8 \times 10^9 \text{ cm}^{-2}\text{s}^{-1}$, a factor of 10 improvement over the flux at the NG7 instrument. Background levels measured for H and other elements are

also a factor of 10 or more lower at NGD. The improved signal to noise ratio results in an a factor of 5 to 20 improvement in elemental detection limits over the NG7 instrument (Table 1).

Table 1: Detection limits (µg) for selected elements at NGD vs. NG7

Element	NG7	NGD
H	3	0.5
B	0.02	0.003
C	8000	900
N	1100	35
Na	40	10
Mg	600	70
Al	170	30
Si	700	40
S	75	10
Cl	4	0.4
K	44	6
Ca	140	30
Ti	10	2
Mn	14	2
Cr	28	5
Fe	140	10
Ni	70	3
Sm	0.03	0.004
Gd	0.015	0.001
Pb	2600	320

Future improvements are planned to take advantage of the increased experimental space and will include design and installation of reaction chambers to measure in-situ reaction products from catalysis and other chemical processes, neutron optics and scanning stages for 2-D and 3-D compositional mapping of samples, additional detectors for coincidence spectrometry, and an automatic sample chamber to increase productivity and efficiency of measurements.

References

- [1] R. L. Paul, R. M. Lindstrom, J. Radioanal. Nucl. Chem. **243**, 181 (2000).
- [2] R. L. Paul, Analyst **122**, 35R (1997).
- [3] R. L. Paul, R. M. Lindstrom, Metall. Mater. Trans. A, **43A**, 4888 (2012).
- [4] R. L. Paul, D. Şahin, J. C. Cook, C. Brocker, R. M. Lindstrom, D. J. O'Kelly, J. Radioanal. Nucl. Chem. **304**, 189 (2014).
- [5] LA-UR-03-1987, MCNP – A General Monte Carlo N-Particle Transport Code, Version 5, X-5 Monte Carlo Team, Los Alamos National Laboratory, April 2003, Rev. 2/1/2008.

¹ Material Measurement Laboratory, National Institute of Standards and Technology, Gaithersburg, MD 20899

² NIST Center for Neutron Research, National Institute of Standards and Technology, Gaithersburg, MD 20899

Reliability and Availability of the Reactor

The reactor operated 198 days during FY 2015, achieving a reliability of 98.5 %. The three days that were lost were due to two separate equipment failures: 1) the loss of an instrumentation power transformer and 2) the failure of a regulating control rod. The lost time was made up by extending the reactor cycles.

Replacement of Rabbit Tubes RT-1 and RT-2

"Rabbits" allow sample to be placed in the reactor for irradiation. During FY 2015, both the RT-1 and RT-2 rabbit tube tips were replaced. The new rabbit tips were fabricated in house by the NIST Shops and assembled by Scott Slifer. Other staff members replaced the old tips with new ones with minimal radiation doses to NCNR staff (Fig. 1). Thus the NCNR again has two fully operational rabbit tubes available for users.



FIGURE 1: James Lewis (L) and Justin Trilli (R) closing up shop on the RT1/RT2 replacement job.

Installing Cold Source Refrigerator Cold Box on the C200 floor

The NCNR has been actively engaged in the design of a liquid deuterium cold neutron source to replace

the current liquid hydrogen source. During FY 2015, the cold box for the new 7 kW cold source refrigerator was installed in its final location (Fig. 2). Transportation of refrigerator cold box through the facility involved a complicated non-standard lift procedure (Fig. 3), which required the development of a step-by-step lifting plan.



FIGURE 2: The cold source refrigerator cold box in its final position, with Sean Mullendore (L) and Scott Slifer (R) securing the assembly.

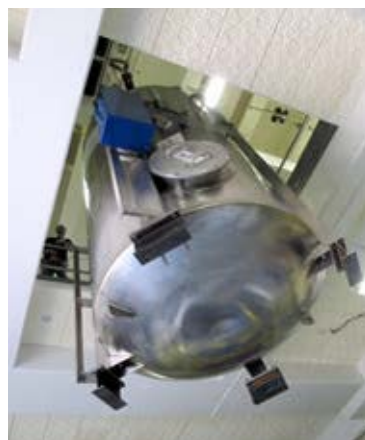


FIGURE 3: The cold source refrigerator cold box as it passes through the (normally plugged) ceiling opening in C-100.

Installations and Upgrades

Two major instrument development projects have seen significant progress this year. First, the design of the 40 m very Small Angle Neutron Scattering (vSANS) instrument has continued throughout 2015. The primary instrument optics have arrived and installation is well underway at NG-3. We anticipate that by the end of 2015, the neutron beam delivery system, velocity selector and neutron/gamma shielding (bunker), cryogenically cooled crystalline Bi-Be filter, attenuator assembly, polarizer guide, 11 pre-sample flight path boxes, and the sample area will all be in place and wiring of these systems will have begun. In addition, modifications have been made to the G-100 East truck bay including utility re-routing to provide support for the vSANS scattering tank which is expected to arrive in late spring of 2016. Tests of the vSANS detector have begun and detector installation is expected in the summer of 2016. Finally data acquisition software for vSANS is in active development and a prototype system is being used on the 10 m SANS in order to ensure that a functional data acquisition system is available when commissioning begins.

Second, scintillator detector development for the white beam reflectometer, CANDoR is nearly complete. Recent tests of the detector performance have shown the

achievement of greater than 80 % absolute neutron sensitivity. A final design will be chosen and procurement of components for fabrication will be complete by the end of 2015. Work continues on design and procurement of all beam line components in addition to assembly and testing of the focusing guide. CANDoR is currently scheduled to come on line in early 2017 on NG-1.

Several upgrade and installation projects have also been completed in 2015. The space vacated by the relocated PGAA instrument at NG-7 was replaced with the test station PHADES (Polarized ^3He And Detector Experiment Station). This station provides capabilities for detector development, polarized beam component tests and development, and single crystal alignment. Beam characterization and commissioning began in June with the instrument being fully functional in July.

Significant upgrades have enhanced the BT-8 Engineering Diffractometer. Upgrades in 2015 include removing the blades of the existing 40' collimator embedded in the BT-8 instrument shutter. The removal of the blades increased the beam cross section on the monochromator by 70 % with up to 50 % gain in flux on the sample. An air balancer mounted to a jib crane has been installed that provides support for samples up to 500 lb, allowing fine control of sample positioning for very large samples.

Design, fabrication and testing has also been completed for an octo-strain device (operational June 2015) and a shear device (operational September 2015). Further upgrades this year include a new position-sensitive detector, which has been delivered and has passed performance testing. Installation will take place once modifications to the detector housing are completed. A new monochromator and new sample translation tables have been purchased and will be installed in 2016. The monochromator will allow measurements at three wavelengths simultaneously, increasing the data collection rate. In addition, sample positioning will be greatly improved with the installation of an optical scanning system. This system



FIGURE 1: Eleven newly installed guide boxes at NG-3 for vSANS.

generates a representation of the sample shape in the context of the instrument, and determines the position of the sample within the instrument reference frame. This will greatly reduce the time required for sample alignment.

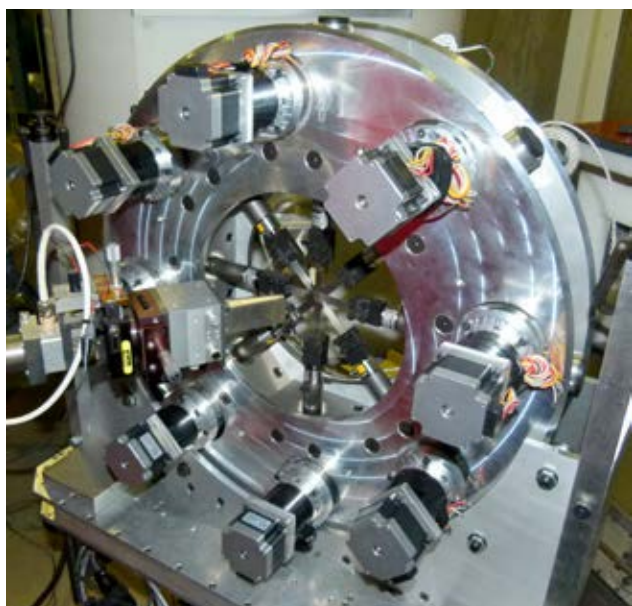


FIGURE 2: Octo-strain device during alignment on the BT-8 instrument table.

The aCORN experiment was relocated from NG-6 to NG-C and a Cold Neutron Imaging Instrument (CNII) was installed on the end position of NG-6. The CNII shutter was opened at the end of August producing the first test radiography image. The CNII instrument provides users with several imaging techniques including conventional radiography, neutron phase imaging, Bragg-edge imaging, polarized neutron imaging, simultaneous x-ray and neutron tomography, and neutron microscope imaging. The CNII instrument complements and extends the capabilities of the highly successful thermal neutron imaging station at BT-2.



FIGURE 3: The first CNII image, taken August 25th, of a steel sample created by NCNR machinist Doug Johnson.

The Neutron Spin Echo (NSE) instrument at NG-A saw performance gains as the cooling circuit for the main coils was upgraded, featuring a new heat exchanger. This allows the maximum current through the main coils to be

increased from 400 A to 500 A, directly translating to a 25 % increase in the maximum Fourier time accessible during NSE experiments.

Helium Spin Filters

The NCNR supports an active program to develop and provide ^3He neutron spin filters (NSFs) for measurements using polarized neutrons. Polarized beam experiments are routinely carried out on the BT-7 thermal neutron triple-axis spectrometer and the small-angle neutron scattering instruments. During the past year, the NCNR's spin filter program served 33 experiments, for a total of 103 days of beam time, 166 bar-liters of polarized ^3He gas, and 101 polarized ^3He cells.

During 2015, significant new capabilities in wide-angle polarization analysis capability were developed on MACS. The apparatus consists of a neutron-compatible solenoid, wide-angle analyzer cells, and a polarizer cell contained in an electrically shielded, RF solenoid for NMR-based polarization inversion. In the last year, the apparatus has been successfully employed for four experiments, yielding valuable operational experience for future routine user capability.

Wide-angle cells have been one of the most challenging and key elements in polarization analysis using ^3He spin filters. Sealed, two- or three-sectioned cells are currently being employed for polarized beam experiments on MACS. This year, we have developed horseshoe-shaped wide-angle cells by pinching off a section from a donut-shaped cell. A horseshoe-shaped cell has four advantages over a three-sectioned cell: 1) since the cell is made from fully blown glass, long relaxation times can be obtained with greater reliability; 2) the circular shape yields a uniform gas path length for all scattering angles; 3) the cross section of the cell is close to rectangular, yielding a more uniform gas path length compared to a round cross section; and 4) only one ^3He spin analyzer is necessary, reducing the demand on our optical pumping system and simplifying polarization corrections from ^3He polarization time-dependence. We successfully obtained a relaxation time of 350 h and achieved a ^3He polarization of 78 % for the first test of such a cell. The relatively smaller inner diameter of the horseshoe-shaped cell cannot accommodate existing MACS/DCS cryostats; hence a new dedicated cryostat with a 7.6 cm outside diameter cryostat tail piece is being purchased. In parallel, we will prepare and test more horseshoe cells.

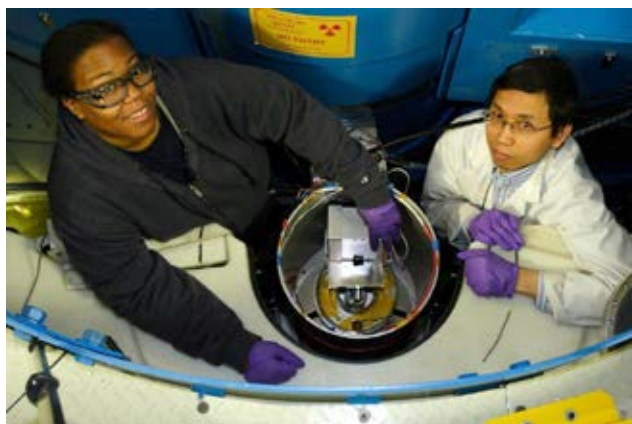


FIGURE 4: Shannon Watson and Wangchun Chen setting up a “horseshoe” cell for polarized beam measurements at MACS.

Data Acquisition Software

The New Instrument Control Environment (NICE) is a Java-based data acquisition package that incorporates a highly versatile scripting capability to enable end user adaptations to be coded under all the major scientific programming languages. NICE software has been deployed for data acquisition on two more instruments, the new NG-7 Test Station PHADES, and the NG-B 10 m SANS. User interfaces have been redesigned and expanded, improving the scripting capabilities and setup of experiment trajectories. After the final deployment at the 10 m SANS, NICE will be deployed on the remaining two 30 m SANS with specific design to streamline polarized beam experiments. The operational experience that will be obtained on the existing SANS instruments will be used to create fully functional data acquisition software for vSANS.

Data Analysis Software

The DAVE (Data Analysis and Visualization Environment) project is a software suite of programs designed for use with data taken on the inelastic neutron instruments at the NCNR and elsewhere. DAVE is actively maintained and developed according to the goals of the project, in response to user feedback and improvements to neutron instrumentation. For the triple axis instruments, the calibration program for the multi-crystal analyzer and position sensitive detector (PSD) for both SPINS and BT-7 have been combined and redesigned to handle other modes of operation as well as the existing “flat” analyzer mode where the individual analyzer blades are aligned. A

“see-through” mode is now included in which each analyzer blade rotates independently to select a different final energy (E_f). There is also a “fixed E_f ,” or more specifically, an Inverse Rowland focusing mode (see article on page 46) in which the final energy is fixed across the analyzer. The impact of these additions is that users can more easily plan experiments with different instrument setups that may better suit their needs. For the Mslice module there are numerous incremental updates that improve on data manipulation and visualization. For example, it is now possible to make cuts of two-dimensional data along any arbitrary direction instead of just along each axis. Also, there are now more flexible options to fold the data along a symmetry axis/axes of the sample in a way that can improve on both the statistics and presentation of data.

The SASView data analysis program has received an optimization upgrade, incorporating the Bumps optimization and uncertainty modeling engine. In addition to returning the best-fit value for a model, the Bumps engine performs a Markov chain Monte Carlo analysis to explore the multidimensional parameter uncertainty from the fit. In addition to returning the credible interval for individual parameter values, Bumps visualizes correlations between pairs of parameters to better understand the fit. As part of an international collaboration between NIST, ANSTO, SNS, ISIS, ILL and ESS, SASView Code Camp-III was held in Denmark in February 2015, resulting in the release of SASView 3.1, incorporating the new fitting engine.

Funded jointly by the NSF and EPSRC, the CCP-SAS project is focused on developing an easy-to-use open-source modeling package that enables users to generate physically accurate atomistic models, calculate scattering profiles and compare results to experimental scattering data sets in a single web-based software suite. In the past year our efforts have led to the release of SASSIE-web to the international scattering community. Several workshop and training sessions have taken place at scattering centers and scientific meetings. Over thirty manuscripts using our software products on a variety of structural biology and soft-matter problems have been published. With hundreds of users the goals of the next year are to enable the software to utilize high performance computational methods to model scattering data.

Serving the Science and Technology Community

Serving the Scientific Community

The mission of the NIST Center for Neutron Research is to assure the availability of neutron measurement capabilities to meet the needs of U.S. researchers from industry, academia and other U.S. government agencies. To carry out this mission, the NCNR uses several different mechanisms to work with participants from outside NIST, including a competitive proposal process, instrument partnerships, and collaborative research with NIST.

Proposal System

Most of the beam time on NCNR instruments is made available through a competitive, peer-review proposal process. The NCNR issues calls for proposals approximately twice a year. Proposals are reviewed at several different levels. First, expert external referees evaluate each proposal on merit and provide us with written comments and ratings. This is a very thorough process where several different referees review each proposal. Second, the proposals are evaluated on technical feasibility and safety by NCNR staff. Third, we convene our Beam Time Allocation Committee (BTAC) to assess the reviews and to allocate the available instrument time. Using the results of the external peer review and their own judgment, the BTAC makes recommendations to the NCNR Director on the amount of beam time to allocate to each approved experiment. Approved experiments are scheduled by NCNR staff members in consultation with the experimenters.

The current BTAC members are:

Andrew Allen (NIST Ceramics Division)
Jeffrey Allen (Michigan Technological University)
Collin Broholm (The Johns Hopkins University)
Leslie Butler (Louisiana State University)
Kushol Gupta (University of Pennsylvania)
Ramanan Krishnamoorti (University of Houston)
Valery Kiryukhin (Rutgers University)
Jennifer Lee (National Institutes of Health)
Raul Lobo (University of Delaware)
Janna Maranas (The Pennsylvania State University)

Steven May (Drexel University)

Ryan Murphy (Solvay)

Lilo Pozzo (University of Washington)

Carlos Rinaldi (University of Florida)

Stephan Rosenkranz (Argonne National Laboratory)

Gila Stein (University of Houston)

Partnerships

The NCNR may form partnerships with other institutions to fund the development and operation of selected instruments. These partnerships, or "Participating Research Teams", may have access to as much as 75 % of the available beam time on the instrument, depending on the share of total costs borne by the team. A minimum of 25 % of the available beam time is always made available through the NCNR proposal program to all users. Partnerships are negotiated for a fixed period (usually three years) and may be renewed if there is mutual interest and a continued need. These partnerships have proven to be an important and effective way to expand the research community's access to NCNR capabilities.

Collaboration with NIST

Some time on all instruments is available to NIST staff in support of our mission. This time is used to work on NIST research needs, instrument development, and promoting the widespread use of neutron measurements in important research areas, particularly by new users. As a result of these objectives, a significant fraction of the time available to NIST staff is used collaboratively by external users, who often take the lead in the research. Access through such collaborations is managed through written beam time requests. In contrast to proposals, beam time requests are reviewed and approved internally by NCNR staff. We encourage users interested in exploring collaborative research opportunities to contact an appropriate NCNR staff member.

Research Participation and Productivity

The NCNR continued its strong record of serving the U.S. research community this year. Over the 2015 reporting year, 2436 research participants benefited from use of the NCNR. (Research participants include users who come to

the NCNR to use the facility as well as active collaborators, including co-proposers of approved experiments, and co-authors of publications resulting from work performed at the NCNR.) As the number of participants has grown, the number of publications per year has increased in proportion. The quality of the publications continues to be at a very high level.

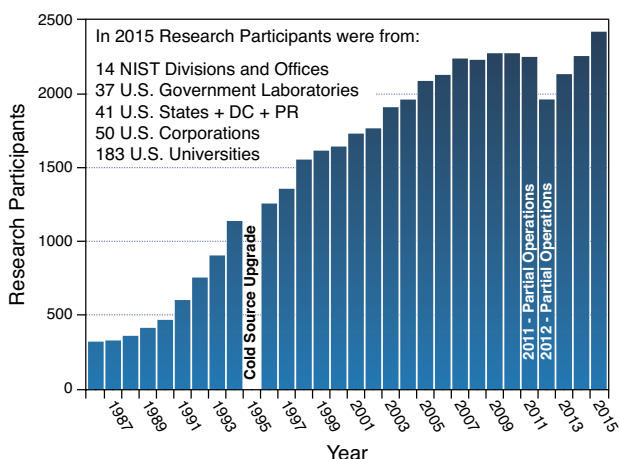


FIGURE 1: Research participants at the NCNR 1986-2015.

2015 NCNR Proposal Program

In response to the last two calls for proposals (calls 32 and 33) for instrument time, we received 716 proposals, of which 413 were approved and received beam time. For the most recent call, the oversubscription, i.e., the ratio of days requested on all proposals to the days available, was 2.0 on average, but as high as 3.1 for specific instruments. Proposal demand has grown constantly since the NCNR first began accepting proposals in 1991, and has more than doubled in the past decade. The following table shows the data for several instrument classes.

Instrument class	Proposals	Days requested	Days allocated
SANS and USANS	255	938	477
Reflectometers	92	576	360
Spectrometers	320	2174	878
Diffraction	25	98	72
Imaging	24	169	110
Total	716	3955	1897

Users Group

The NCNR Users Group (NUG) provides an independent forum for all facility users to raise issues to NCNR management, working through its executive officers to carry out this function. The current members of the NUG Executive Committee are Alan Nakatani (Dow Chemical, chair), Michael Crawford (DuPont), Amber Larson (University of Maryland, student/postdoc member), Michael Mackay (University of Delaware), Megan Robertson (University of Houston), Rafael Verduzco (Rice University) and Igor Zaliznyak (Brookhaven National Laboratory).

Panel of Assessment

The major organizational components of NIST are evaluated annually for quality and effectiveness by the National Research Council (NRC), the principal operating agency of both the National Academy of Sciences and the National Academy of Engineering. A panel appointed by the NRC last reported on the NIST Center of Neutron Research in July 2013. The findings are summarized in a document that may be viewed online at <http://www.nist.gov/director/nrc/upload/ncnr-final-report-2013.pdf>. A new panel convened at the NCNR on July 7-8, 2015, and their final report should be available online within the next calendar year. The panel members included Peter Green (University of Michigan), Frank Bates (University of Minnesota), Bruce Gaulin (McMaster University), Hubert King (ExxonMobil), Janos Kirz (Lawrence Berkeley Laboratory and Stony Brook University), Roger Leach (Dupont), V. Adrian Parseghian (University of Massachusetts), Sunhil Sinha (University of California at San Diego).

The Center for High Resolution Neutron Scattering (CHRNS)

CHRNS is a national user facility that is jointly funded by the National Science Foundation and the NCNR. Its primary goal is to maximize access to state-of-the-art neutron scattering instrumentation for the research community. It operates five neutron scattering instruments at the NCNR, enabling users from around the nation to observe dynamical phenomena involving energies from ≈ 30 neV to ≈ 10 meV, and to obtain structural information on length scales from ≈ 1 nm to ≈ 10 microns. A more detailed account of CHRNS activities may be found on page 58 of this report.

Partnerships for Specific Instruments

NG-7 SANS Consortium

A consortium that includes NIST, the ExxonMobil Research and Engineering Company, and the Industrial Partnership for Research in Interfacial and Materials Engineering (IPRIME) led by the University of Minnesota, operates, maintains, and conducts research at the NG-7 30 m SANS instrument. The consortium uses 57 % of the beam time on this instrument, with the remaining 43 % allocated to the general scientific community through the NCNR's proposal system. Consortium members conduct independent research programs primarily in the area of large-scale structure in soft matter. For example, ExxonMobil has used this instrument to deepen their understanding of the underlying nature of ExxonMobil's products and processes, especially in the fields of polymers, complex fluids, and petroleum mixtures.

The nSoft Consortium

Formed in August 2012, the nSoft Consortium allows member companies to participate with NIST in the development of advanced measurements of materials and manufacturing processes, and develop their own expertise in state-of-the-art measurement technologies to include in their analytical research programs. nSoft develops new neutron-based measurement science for manufacturers of soft materials including plastics, composites, protein solutions, surfactants, and colloidal fluids. Members receive access to leading expertise and training support in neutron technology and soft materials science at NIST. Contact: Ron Jones, nSoft Director, rljones@nist.gov, 301-975-4624.

NIST / General Motors – Neutron Imaging

An ongoing partnership and collaboration between General Motors and NIST that now includes Honda Motors through GM's partnership with Honda continues to yield exciting results using neutron imaging. Neutron imaging

has been employed to visualize the operation of fuel cells for automotive vehicle applications. Neutron imaging is an ideal method for visualizing hydrogen, the fuel of electric vehicle engines. These unique, fundamental measurements provide valuable material characterizations that will help improve the performance, increase the reliability, and reduce the time to market introduction of the next generation electric car engines. 25 % of the time on the BT-2 Neutron Imaging Facility is made available to the general scientific community through peer-reviewed proposals.

Interagency Collaborations

The Smithsonian Institution's Nuclear Laboratory for Archaeological Research is part of the Anthropology Department at the National Museum of Natural History. It has had a longstanding and productive partnership with the NCNR, during which time it has chemically analyzed over 43,100 archaeological artifacts by Instrumental Neutron Activation Analysis (INAA), drawing extensively on the collections of the Smithsonian, as well as on those of many other institutions in this country and abroad. Such chemical analyses provide a means of linking these diverse collections together in order to study continuity and change involved in the production of ceramic and other artifacts.

The Center for Food Safety and Applied Nutrition, U.S. Food and Drug Administration (FDA), maintains laboratory facilities at the NCNR providing agency-wide analytical support for food safety and food defense programs. Neutron activation and low-level gamma-ray detection techniques yield multi-element and radiological information about foods and related materials and provide a metrological foundation for FDA's field investigations and for radiological emergency response planning.

The Center for High Resolution Neutron Scattering (CHRNS)



The Center for High Resolution Neutron Scattering is a national user facility that is jointly funded by the National Science Foundation through its Division of Materials Research (grant number DMR-0944772) and by the NCNR. The primary purpose of this partnership is to maximize access to state-of-the-art neutron scattering instrumentation for the research community using the NCNR's proposal system. Proposals to use the CHRNS instruments are critically reviewed on the basis of scientific merit and/or technological importance. The core mission of CHRNS is fourfold: (i) to develop and operate neutron scattering instrumentation, with broad application in materials research, for use by the general scientific community; (ii) to promote the effective use of the CHRNS instruments by having an identifiable staff whose primary function is to assist users; (iii) to conduct research that advances the capabilities and utilization of CHRNS facilities; and (iv) to contribute to the development of human resources through educational and outreach efforts.

Following the submission of a new proposal and a site visit in January 2015, the CHRNS agreement was renewed (grant number DMR-1508249) for five years. The success of the proposal was based on the demonstrated ability of CHRNS to advance neutron scattering measurement capabilities and its prominent role in expanding, educating, and diversifying the community of researchers who use neutron methods. As part of the new agreement (which began in September 2015), the portfolio of instruments supported by CHRNS will continue to evolve to ensure that the scientific capabilities exceed or are comparable to the best worldwide. Input for these new directions was obtained from the scientific community through a variety of mechanisms including a workshop held in August 2014 entitled "Neutron Measurements for Materials Design and Characterization."

Scattering Instruments

During FY 2015, CHRNS supported operation of the following instruments: the NG-B 30m Small Angle Neutron Scattering (SANS) instrument, the Ultra-Small Angle Neutron Scattering (USANS) instrument, the Multi-Angle Crystal Spectrometer (MACS), the High Flux Backscattering Spectrometer (HFBS), and the Neutron Spin-Echo (NSE) spectrometer. Combined, CHRNS instruments can provide structural information on a length scale of ≈ 1 nm to ≈ 10 microns, and dynamical information on energy scales

from ≈ 30 neV to ≈ 10 meV. The new CHRNS agreement continues programs in instrument operations and development on HFBS, NSE, and MACS, which boasts the world's highest monochromatic cold-neutron flux and is now the premier instrument in the world for investigations of quantum magnetism. As part of the new CHRNS agreement, new magnetic correction coils will be installed on NSE within the next few years. The implementation of state-of-the-art Pythagoras coils will make possible measurements up to ≈ 300 ns, which will provide a three-fold increase of the effective instrument resolution. Significant additions to the CHRNS facility include two innovative instruments, vSANS and CANDOR, which will be folded into CHRNS as the installation and commissioning of these new instruments progress. The data rates provided by the multiplex detector assembly of the CANDOR reflectometer will exceed those available elsewhere in the world by perhaps an order of magnitude or more. The versatile vSANS instrument will cover extensive nano-to-meso length scales in a single measurement, eliminating the need for combined experiments on uSANS and SANS in many cases. CHRNS support for uSANS and SANS will thus be phased out following the commissioning of vSANS and CANDOR. The new CHRNS agreement also includes an expansion and enhancement of the existing NCNR effort in ^3He spin filters to ensure that full polarized beam capabilities are available on MACS, SANS, vSANS and CANDOR. Currently, both SANS and MACS make frequent use of record-breaking ^3He spin analyzer cells with specialized geometries.

Research

The wide range of instrument capabilities available in CHRNS support a very diverse scientific program, allowing researchers in materials science, chemistry, biology, and condensed matter physics to investigate materials such as polymers, metals, ceramics, magnetic materials, porous media, fluids, gels, and biological molecules. Ten scientific highlights utilizing the five current CHRNS instruments are featured in this Annual Report.

In the most recent Call for Proposals (call 33), 225 proposals requested CHRNS instruments, and 125 of these proposals received beam time. Of the 1139 days requested for the CHRNS instruments, 510 were awarded. (These numbers include all of the SANS proposals: Approximately 75 % of the beam time approved by BTAC will be run on the CHRNS

NGS SANS.) Roughly half of the users of neutron scattering techniques at the NCNR use CHRS-funded instruments, and more than one quarter of NCNR publications (see the "Publications" section on p. 63), over the current one-year period, are based on research performed using these instruments.

Scientific Support Services

In FY2015, CHRS provided scientific support in two critical areas: sample environment and chemical laboratories.

The laboratory staff continues to equip and maintain user laboratories and routinely assists users with sample preparations. The staff ensures that users have the tools and supplies they need for a successful experiment. Two new refrigerators were acquired that provide more space and reliable temperature control for sample and chemical storage. The x-ray capabilities will soon be expanded significantly with the recent purchase of an x-ray Laue that can be utilized for crystal alignment prior to neutron scattering experiments.

The CHRS Sample Environment team provides users with the equipment and training needed to make neutron measurements under external conditions of temperature, pressure, magnetic field, humidity, and fluid flow. During FY2105 a new syringe pump system was purchased and commissioned routine operation on the SANS instruments. This versatile device, with a flow range from 0.00001 mL/min to 60 mL/min and pressure up to 690 bar, can be utilized on a wide range of materials including aqueous and organic liquids, liquefied gases, and viscous fluids or colloids. These pumps are compatible with our new SANS flow cells which have interchangeable flow channel geometries and temperature control from $\approx 10^\circ\text{C}$ to $\approx 80^\circ\text{C}$. The SANS sample environment suite was expanded further with the addition of a new rheometer which is ideally suited for 1-3 and 2-3 shear direction measurements. Within the next year, we expect delivery of a new Peltier block, which will allow for more efficient temperature changes in routine SANS experiments.

Education and Outreach

This year the Center for High Resolution Neutron Scattering sponsored a variety of educational programs and activities tailored to specific age groups and professions. The annual Summer School, held on June 8-12, 2015 was entitled "Methods and Applications of Neutron Spectroscopy." Thirty-four graduate and postdoctoral students from 22 universities participated in the school.

Lectures, research seminars and were highlighted for a wide variety of neutron measurement techniques. The guest lecturers were Prof. Efrain Rodriguez from the University of Maryland, Prof. Yang Zhang from the University of Illinois at Urbana-Champaign, and Prof. Joel Helton from the U.S. Naval Academy. The evaluations were excellent and student feedback was very positive.

As part of its expanding education and outreach effort, CHRS offers to university-based research groups with BTAC-approved experimental proposals the opportunity to request travel support for an additional graduate student to participate in the experiment. This support is intended to enable prospective thesis students, for example, to acquire first-hand experience with a technique that they may later use in their own research. Announcements of this program are sent to all of the university groups whose experimental proposals receive beam time from the BTAC. Recipients of the announcement are encouraged to consider graduate students from under-represented groups for this opportunity. The program is also advertised on the NCNR's website at <http://www.ncnr.nist.gov/outreach.html>.

As in previous years, CHRS participated in NIST's Summer Undergraduate Research Fellowship (SURF) program. In 2015 CHRS hosted 14 SURF students, including four returning interns from the previous year. The students participated in research projects such as extensional flow of micelles, characterization of conducting nanoparticles for flow battery applications, magnetic ordering in heavy fermions, enhanced fitting for diffraction data refinement, and design of a new research reactor. They presented their work at the NIST SURF colloquium in early August 2015.



FIGURE 1: Participants and instructors in the NCNR 2015 Summer School "Methods and Applications of Neutron Spectroscopy"

Elementary, Middle, and High School Activities

The Summer High school Intern Program (SHIP) is a very successful, competitive NIST-wide program for students who are interested in performing scientific research during the summer. CHRNA hosted eight high school interns from local Maryland schools. The students' research included studying the effects of peptides on lipid phase behavior, exploring entropy in experimental design, applying machine learning to the classification of crystal unit cells, and developing a scintillator neutron detector. The results of the students' summer investigations were highlighted in a NIST-wide poster session in early August, as well as in a well-attended oral symposium at the NCNR. The success of the high school students is exemplified by the recent publication an article on the phase segregation of sulfonate groups in Nafion lamellae [S.C. DeCaluwe, *et al.*, *Soft Matter* **10**, 5763 (2014)], which features former SHIP (and SURF) student Pavan Bhargava as a co-author. Inspired, in part, by his intern experiences at the NCNR, Pavan is currently a graduate student in electrical engineering at the University of California at Berkeley.



FIGURE 2: The 2015 SURF students

The NCNR initiated a Research Experiences for Teachers (RET) program in the summer of 2010. Kevin Martz, a physics teacher from Richard Montgomery High School (Montgomery County, MD), was selected for the program for the summer of 2015. He collaborated with NCNR's Boualem Hammouda on SANS investigations of micelles under pressure.



FIGURE 3: The 2015 SHIP interns

The annual Summer Institute for Middle School Science Teachers brings middle school science teachers from across the United States to NIST for two weeks in order to give them a better understanding of the scientific process. Each year, CHRNA hosts the teachers for a one-day introduction to neutron scattering in July with a presentation that describes how neutrons are produced and how they are used to improve our understanding of materials at the atomic scale. Having toured the neutron guide hall and having seen several neutron instruments, the teachers learn about the types of experiments performed at the NCNR. To bring home projects suitable for middle school students, they then learn how to grow crystals of alum (hydrated aluminum potassium sulfate). Throughout the day and at lunchtime, the teachers have the opportunity to interact with staff members. In addition, a large number of specialized tours for middle school, high school, and university students were offered throughout the year.



FIGURE 4: Juscilino Leão demonstrates nuclear fission using mousetraps and ping-pong balls during the 2015 Summer Institute for Middle School Science Teachers



Thomas H. Epps, III, a frequent user of the NCNR, has been selected as the 2015 winner of the **Owens-Corning Early Career Award** by the Materials Engineering and Sciences Division (MESD) of the American Institute of Chemical Engineers (AIChE). Epps is the Thomas and Kipp Gutshall Associate Professor of Chemical and Biomolecular Engineering and associate professor of materials science and engineering at the University of Delaware. Epps was cited for "groundbreaking research in understanding and engineering block polymer interfacial energetics toward the nanoscale self-assembly of polymers in bulk, thin films, and solutions."



Doug Godfrin of the NCNR was awarded "**Most Outstanding Poster**" in the area of Biotechnology, Biology, and Polymers for his poster entitled: "Cluster Mediated Dynamics and Viscosity in Concentrated Protein Formulations" at the annual **Sigma Xi Post-doc poster** presentation. Congratulations also go to Doug for **placing 1st** in the **2014 AIChE Bio Nanotechnology Graduate Student Award Symposium** at the national meeting in November 2014. His presentation was titled "Viscosity increase in concentrated mAb solutions due to large transient clusters."



Alex Grutter of the NCNR received **second place** in the area of Materials for his poster entitled: "Probing Domain Structure in High-Density Segmented Nanowire Arrays Through Polarization Analyzed SANS" at the annual **Sigma Xi Post-doc poster presentation**.



Kate Gurnon of the Department of Chemical Engineering at the University of Delaware was awarded the 2015 **Alan P. Colburn Dissertation Prize** for her Ph. D. dissertation entitled: "Nonlinear Oscillatory Rheology and Structure of Wormlike Micellar Solutions and Colloidal Suspensions"



Prof. Sow-Hsin Chen from the Department of Nuclear Science & Engineering at the Massachusetts Institute of Technology was announced as the **2015 Guinier Prize** winner. The Guinier Prize, sponsored by the International Union of Crystallography (Iucr), recognizes lifetime achievement, a major breakthrough or an outstanding contribution to the field of small-angle scattering. Over his 50-year career, Professor Sow-Hsin Chen has made numerous original and novel contributions employing small-angle scattering in fundamental studies of soft condensed matter physics. He has trained a significant portion of the next generation of researchers in the field, including 45 PhD students. He and his students have made extensive use of many instruments at the NCNR. The announcement was made at the 16th International conference on Small-Angle Scattering in Berlin, September 2015.



Michael Mendenhall has received the 2015 **APS Outstanding Dissertation Award in Nuclear Physics** for his thesis titled "Measurement of the Neutron Decay Asymmetry Using Ultracold Neutrons". Michael received his Ph. D. from California Institute of Technology in 2014. For his thesis research, he worked with aCORN, using bottled ultracold neutrons to measure the angular correlation between neutron polarization and electron momentum.



Paul Brand and Tony Norbedo have been selected to receive the **Department of Commerce Silver Medal** for their outstanding work on the

new thermal shield cooling system. The specific citation is “for the design and implementation of an innovative upgrade that greatly extends the lifetime of the NIST Center for Neutron Research, a critical scientific user facility.”



Prof. Norman Wagner, Robert L. Pigford Chair of Chemical Engineering and joint professor, Department of Physics and Astronomy, University of Delaware, has been elected to the **National Academy of Engineering** in recognition of his research on “understanding flow-induced microstructural transitions in complex liquids and invention of ballistic-resistant fabrics by strain-hardening suspensions.” Norm is a frequent user of NCNR facilities.



Jeremy Cook has been selected to receive the **Department of Commerce Silver Medal** for his work designing the new neutron guides and shields that were a key part of the NCNR Expansion. Specifically, the citation for his work is “for the design of the neutron guide system and shielding crucial to the NCNR’s Neutron Facility Expansion Project, greatly advancing NIST’s measurement science mission.”



Kathryn Krycka is a recipient of the 2014 **NIST Bronze Medal Award**. Kathryn is being recognized for her “profound advancements to neutron spin polarization techniques and their subsequent application to the characterization of magnetic nanostructures.”



Thomas Gnäupel-Herold of the NCNR and Adam Creuziger of NIST MML are recipients of the 2014 **NIST Bronze Medal Award**. Thomas and Adam are being recognized for “the development of new analysis techniques for error determinations of crystallographic phase fractions, textures, and intergranular stresses.”



Kate Ross has been recognized by The Academy of Science of the Royal Society of Canada with the **2014 Alice Wilson Award**. This award is given yearly, recognizing women of outstanding academic qualifications in the Arts and Humanities, Social Sciences or Science who are entering a career in scholarship or research at the postdoctoral level. Kate spent two years as a postdoctoral fellow at Johns Hopkins University and the NCNR. She is currently an assistant professor at Colorado State University where she is working on designing new materials that display unusual quantum phases of matter. Kate uses neutron scattering as a probe of the quantum phenomena in these materials.

- Abdul-Jabbar, G., Sokolov, D.A., O'Neill, C.D., Stock, C., Vermeille, D., Demmel, F., Krüger, F., Green, A.G., Lévy-Bertrand, F., Grenier, B., Huxley, A.D., "Modulated Magnetism in PrPtAl," *Nat. Phys.* **11**(4), 321 (2015).
- Ajay Mallia, V., Weiss, R.G., "Structural Bases for Mechano-Responsive Properties in Molecular Gels of (*R*)-12-hydroxy-N-(ω -hydroxyalkyl)octadecanamides. Rates of Formation and Responses to Destructive Strain," *Soft Matter* **11**(25), 5010 (2015).
- Akabori, K., Huang, K., Treece, B.W., Jablin, M.S., Maranville, B., Woll, A., Nagle, J.F., Garcia, A.E., Tristram-Nagle, S., "HIV-1 Tat Membrane Interactions Probed using X-ray and Neutron Scattering, CD Spectroscopy and MD Simulations," *BBA-Biomembranes* **1838**, 3078 (2014).
- Akamatsu, M., FitzGerald, P.A., Shiina, M., Misono, T., Tsuchiya, K., Sakai, K., Abe, M., Warr, G.G., Sakai, H., "Micelle Structure in a Photoresponsive Surfactant with and without Solubilized Ethylbenzene from Small-Angle Neutron Scattering," *J. Phys. Chem. B* **119**(18), 5904 (2015).
- Al-Sheikhly, M., Amde, A.M., Livingston, R.A., "Final Report for Highway IDEA Project 136: Development of a 2nd Generation Neutron-Based Detector for Chloride in Concrete," *Trans. Res. Board Nat. Acad.*, **1** (2014).
- Allen, A.J., Espinal, L., Wong-Ng, W., Queen, W.L., Brown, C.M., Kline, S.R., Kauffman, K.L., Culp, J.T., Matranga, C., "Flexible Metal-Organic Framework Compounds: *In situ* Studies for Selective CO₂ Capture," *J. Alloy Compd.*, in press.
- Andersen, K.H., Barker, J.G., "Promising Times for Neutron Scattering," *J. Appl. Crystallogr.* **47**(4), 1163 (2014).
- Anovitz, L.M., Cole, D.R., Swift, A., Sheets, J., Elston, H., Welch, S., Chipera, S.J., Littrell, K.C., Mildner, D.F.R., Wasbrough, M.J., "Multiscale (nano to mm) Porosity in the Eagle Ford Shale: Changes as a Function of Maturity," in "Unconventional Resources Technology Conference," (Unconventional Resources Technology Conference, August 2014, Denver, CO), 1923519 (2014). [CHRS]
- Anovitz, L.M., Cole, D.R., Jackson, A.J., Rother, G., Littrell, K.C., Allard, L.F., Pollington, A.D., Wesolowski, D.J., "Effect of Quartz Overgrowth Precipitation on the Multiscale Porosity of Sandstone: A (U)SANS and Imaging Analysis," *Geochim. Cosmochim. Ac.* **158**(1), 199 (2015). [CHRS]
- Anovitz, L.M., Cole, D.R., Sheets, J., Swift, A., Elston, H.W., Welch, S., Chipera, S.J., Littrell, K.C., Mildner, D.F.R., Wasbrough, M.J., "Effects of Maturation on Multiscale (Nanometer to Millimeter) Porosity in the Eagle Ford Shale," Interpretation, in press. [CHRS]
- Asada, M., Jiang, N., Sendogdular, L., Sokolov, J., Endoh, M.K., Koga, T., Fukuto, M., Yang, L., Akgun, B., Dimitriou, M., Satija, S., "Melt Crystallization/Dewetting of Ultrathin PEO Films via Carbon Dioxide Annealing: the Effects of Polymer Adsorbed Layers," *Soft Matter* **10**(34), 6392 (2014).
- Ashkar, R., Stonaha, P., Washington, A., Shah, V.R., Fitzsimmons, M.R., Maranville, B., Majkrzak, C.F., Lee, W.T., Pynn, R., "Spin-Echo Resolved Grazing Incidence Scattering (SERGIS) at Pulsed and CW Neutron Sources," *J. Phys. Conf. Ser.* **251**, 012066 (2010).
- Ashkar, R., Bertrand, C., Abdulkali, M., Tyagi, M., Faraone, A., Butler, P., Krishnamoorti, R., "Hierarchical Polymer Dynamics in Carbon Nanocomposites with Strong Interfacial Attraction," in "TechConnect World Technical Proceedings 2015," edited by Wennings, S., in press.
- Ashkar, R., Baki, M.A., Tyagi, M., Faraone, A., Butler, P., Krishnamoorti, R., "Kinetic Polymer Arrest in Percolated SWNT Networks," *ACS Macro Lett.* **3**(12), 1262 (2014). [CHRS]
- Ashkar, R., Nagao, M., Butler, P.D., Woodka, A.C., Sen, M.K., Koga, T., "Tuning Membrane Thickness Fluctuations in Model Lipid Bilayers," *Biophys. J.* **109**(1), 106 (2015). [CHRS]
- Baek, J.S., Cuadra, A., Cheng, L.-Y., Hanson, A.L., Brown, N.R., Diamond, D.J., "Analysis of Loss-of-Flow Accidents for the NIST Researcher Reactor with Fuel Conversion from HEU to LEU," *Nucl. Technol.* **189**(1), 71 (2015).

- Baek, J.S., Cheng, L.-Y., Diamond, D., "Analysis of Loca Scenarios in the NIST Researcher Reactor Before and After Fuel Conversion," in "16th International Topical Meeting on Nuclear Research Thermal Hydraulics," in press.
- Bahadur, J., Melnichenko, Y.B., Mastalerz, M., Furmann, A., Clarkson, C.R., "Hierarchical Pore Morphology of Cretaceous Shale: A Small-Angle Neutron Scattering and Ultrasmall-Angle Neutron Scattering Study," *Energ. Fuel.* **28**(10), 6336 (2014). [CHNRNS]
- Bahadur, J., Radlinski, A.P., Melnichenko, Y.B., Mastalerz, M., Schimmelmann, A., "Small-Angle and Ultrasmall-Angle Neutron Scattering (SANS/USANS) Study of New Albany Shale: A Treatise on Microporosity," *Energ. Fuel.* **29**(2), 567 (2015). [CHNRNS]
- Bañuelos, J.L., Feng, G., Fulvio, P.F., Li, S., Rother, G., Arend, N., Faraone, A., Dai, S., Cummings, P.T., Wesolowski, D.J., "The Influence of a Hierarchical Porous Carbon Network on the Coherent Dynamics of a Nanoconfined Room Temperature Ionic Liquid: A Neutron Spin Echo and Atomistic Simulation Investigation," *Carbon* **78**, 415 (2014). [CHNRNS]
- Barker, J.G., Mildner, D.F.R., "Survey of Background Scattering from Materials found in Small-Angle Neutron Scattering," *J. Appl. Crystallogr.*, in press. [CHNRNS]
- Barnett, G.V., Razinkov, V.I., Kerwin, B.A., Laue, T.M., Woodka, A.H., Butler, P.D., Perevozchikova, T., Roberts, C.J., "Specific-Ion Effects on the Aggregation Mechanisms and Protein-Protein Interactions for Anti-Streptavidin Immunoglobulin Gamma-1," *J. Phys. Chem. B* **119**(18), 5793 (2015).
- Baroudi, K., Gaulin, B.D., Lapidus, S.H., Gaudet, J., Cava, R.J., "Symmetry and Light Scattering of $\text{Ho}_2\text{Ti}_2\text{O}_7$, $\text{Er}_2\text{Ti}_2\text{O}_7$, and $\text{Yb}_2\text{Ti}_2\text{O}_7$, Characterized by Synchrotron X-ray Diffraction," *Phys. Rev. B* **92**(2), 024110 (2015).
- Basavaraj, M.G., McFarlane, N.L., Lynch, M.L., Wagner, N.J., "Nanovesicle Formation and Microstructure in Aqueous Ditolowethylesterdimethylammonium Chloride (DEDMAC) Solutions," *J. Colloid Interf. Sci.* **429**, 17 (2014). [CHNRNS]
- Bazilevskaya, E., Rother, G., Mildner, D.F.R., Pavich, M., Cole, D., Bhatt, M.P., Jin, L., Steefel, C.I., Brantley, S.L., "How Oxidation and Dissolution in Diabase and Granite Control Porosity during Weathering," *Soil Sci. Soc. Am. J.* **79**(1), 55 (2015). [CHNRNS]
- Bellur, K., Medici, E., Allen, J., Choi, C.K., Hermanson, J., Tamilarasan, A., Hussey, D., Jacobson, D., Leao, J.B., McQuillen, J., "Neutron Radiography of Condensation and Evaporation of Hydrogen in a Cryogenic Condition," *J. Heat Transf.*, in press.
- Benedetto, A., Heinrich, F., Gonzalez, M.A., Fragneto, G., Watkins, E., Ballone, P., "Structure and Stability of Phospholipid Bilayers Hydrated by a Room-Temperature Ionic Liquid/Water Solution: A Neutron Reflectometry Study," *J. Phys. Chem. B* **118**(42), 12192 (2014).
- Bertrand, C.E., Liu, Y., "Molecular Dynamics of a Model Dimerizing Fluid," *J. Chem. Phys.* **142**(4), 044503 (2015).
- Bloch, E.D., Queen, W.L., Chavan, S., Wheatley, P.S., Zadrozny, J.M., Morris, R., Brown, C.M., Lamberti, C., Bordiga, S., Long, J.R., "Gradual Release of Strongly Bound Nitric Oxide from $\text{Fe}_2(\text{NO})_2(\text{dobdc})$," *J. Am. Chem. Soc.* **137**(10), 3466 (2015).
- Bradley-Shaw, J.L., Camp, P.J., Dowding, P.J., Lewtas, K., "Glycerol Monooleate Reverse Micelles in Nonpolar Solvents: Computer Simulations and Small-Angle Neutron Scattering," *J. Phys. Chem. B* **119**(11), 4321 (2015).
- Brodeck, M., Maccarrone, S., Saha, D., Willner, L., Allgaier, J., Mangiapia, G., Frielinghaus, H., Holderer, O., Faraone, A., Richter, D., "Asymmetric Polymers in Bicontinuous Microemulsions and their Accretion to the Bending of the Membrane," *Colloid Polym. Sci.* **293**(4), 1253 (2015). [CHNRNS]
- Brookes, E.H., Anjum, N., Curtis, J.E., Marru, S., Singh, R., Pierce, M., "GenApp Module Execution and Airavata Integration," in "2014 9th Gateway Computing Environments Workshop (GCE)," edited by Wilkins-Diehr, N., (2014 9th Gateway Computing Environments Workshop (GCE), November 2014, New Orleans, LA), **9** (2014).
- Brookes, E.H., Anjum, N., Curtis, J.E., Marru, S., Singh, R., Pierce, M., "The GenApp Framework Integrated with Airavata for Managed Compute Resource Submissions," *Concurr. Comp.-Pract. E.*, in press.
- Brown, N.R., Hanson, A.L., Diamond, D.J., "Impact of Local Burnup on Prediction of Power Density in the NIST Research Reactor," *Nucl. Technol.* **187**(1), 103 (2014).

- Buelt, A.A., Osti, N.C., Htet, Y., Conrad, C.A., Shehata, M.F., Potai, R., Tennyson, A.G., Perahia, D., Smith, R.C., "Conjugated Polymers with *m*-Pyridine Linkages: Synthesis, Photophysics, Solution Structure and Film Morphology," *J. Mater. Chem. C* **2**(38), 8113 (2014). [CHNRNS]
- Butch, N.P., Manley, M.E., Jeffries, J.R., Janoschek, M., Huang, K., Maple, M.B., Said, A.H., Leu, B.M., Lynn, J.W., "Symmetry and Correlations Underlying Hidden Order in URu_2Si_2 ," *Phys. Rev. B* **91**(3), 035128 (2015).
- Cai, L., Toulouse, J., Harriger, L., Downing, R.G., Boatner, L.A., "Origin of the Crossover between a Freezing and a Structural Transition at Low Concentration in the Relaxor Ferroelectric $\text{K}_{1-x}\text{Li}_x\text{TaO}_3$," *Phys. Rev. B* **91**(13), 134106 (2015).
- Cardiel, J.J., Zhao, Y., De La Iglesia, P., Pozzo, L.D., Shen, A.Q., "Turning up the Heat on Wormlike Micelles with a Hydrotropic Salt in Microfluidics," *Soft Matter* **10**(46), 9300 (2014). [CHNRNS]
- Chen, H., Hsiao, Y.-C., Hu, B., Dadmun, M., "Tuning the Morphology and Performance of Low Bandgap Polymer:Fullerene Heterojunctions via Solvent Annealing in Selective Solvents," *Adv. Funct. Mater.* **24**(32), 5129 (2014). [CHNRNS]
- Chen, J., Kondev, F.G., "Nuclear Data Sheets for $A = 209$," *Nucl. Data Sheets* **126**, 373 (2015).
- Chen, J., Kline, S.R., Liu, Y., "From the Depletion Attraction of the Bridging Attraction: The Effect of Solvent Molecules on the Effective Colloidal Interactions," *J. Chem. Phys.* **142**(8), 084904 (2015).
- Chen, J.J., Conron, S.M., Erwin, P., Dimitriou, M., McAlahney, K., Thompson, M.E., "High-Efficiency BODIPY-Based Organic Photovoltaics," *ACS Appl. Mater. Interfaces* **7**(1), 662 (2015).
- Chen, J., Chua, Y.S., Wu, H., Xiong, Z., He, T., Zhou, W., Ju, X., Yang, M., Wu, G., Chen, P., "Synthesis, Structures and Dehydrogenation of Magnesium Borohydride-Ethylenediamine Composites," *Int. J. Hydrogen Energ.* **40**(1), 412 (2015).
- Chen, J., Wu, G., Xiong, Z., Wu, H., Chua, Y.S., Zhou, W., Liu, B., Ju, X., Chen, P., "Synthesis, Thermal Behavior, and Dehydrogenation Kinetics Study of Lithiated Ethylenediamine," *Chem.-Eur. J.* **20**(42), 13636 (2014).
- Chen, K.S., Carnes, B., Wang, C.-Y., Borup, R., Harvey, D., Tabuchi, Y., "V.F.3 Development and Validation of a Two-Phase, Three-Dimensional Model for PEM Fuel Cells," 2012 Annual Progress Report DOE Hydrogen and Fuel Cells Program **DOE/GO-102012-3767**, V-217 (2012).
- Cheng, C.-Y., Oh, H., Wang, T.-Y., Raghavan, S.R., Tung, S.-H., "Mixtures of Lecithin and Bile Salt can Form Highly Viscous Wormlike Micellar Solutions in Water," *Langmuir* **30**(34), 10221 (2014).
- Chung, Y.G., Camp, J., Haranczyk, M., Sikora, B.J., Bury, W., Krungleviciute, V., Yildirim, T., Farha, O.K., Sholl, D.S., Snurr, R.Q., "Computation-Ready, Experimental Metal-Organic Frameworks: A Tool to Enable High-Throughput Screening of Nanoporous Crystals," *Chem. Mater.* **26**(21), 6185 (2014).
- Cicerone, M.T., Averett, D., de Pablo, J.J., "The Role of Hopping on Transport above T_c in Glycerol," *J. Non-Cryst. Solids* **407**(1), 118 (2015).
- Cicerone, M.T., Pikal, M.J., Qian, K.K., "Stabilization of Proteins in Solid Form," *Adv. Drug Delivery Rev.*, in press. [CHNRNS]
- Cicerone, M.T., Zhong, Q., Tyagi, M., "Picosecond Dynamic Heterogeneity, Hopping, and Johari-Goldstein Relaxation in Glass-Forming Liquids," *Phys. Rev. Lett.* **113**(11), 117801 (2014).
- Cleveland, IV, T.E., Kelman, Z., "Isotopic Labeling of Proteins in *Halobacterium Salinarum*," in "Methods in Enzymology," (Elsevier Inc., Atlanta, GA) in press.
- Cook, J.C., Barker, J.G., Rowe, J.M., Williams, R.E., Gagnon, C., Lindstrom, R.M., Ibberson, R.M., Neumann, D.A., "Experimental Characterization of the Advanced Liquid Hydrogen Cold Neutron Source Spectrum of the NBSR Reactor at the NIST Center for Neutron Research," *Nucl. Instrum. Meth. A*, in press.
- Couet, A., Motta, A.T., Comstock, R.J., "Hydrogen Pickup Measurements in Zirconium Alloys: Relation to Oxidation Kinetics," *J. Nucl. Mater.* **451**(1-3), 1 (2014).

- Crawford, B.E., Anderson, E., Barrón-Palos, L., Bass, C.D., Bass, T.D., Fry, J., Gan, K., Haddock, C., Heckel, B.R., Luo, D., Malone, R.C., Markoff, D.M., Micherdzinska, A.M., Mumm, H.P., Nico, J.S., Oppen, A.K., Penn, S., Santra, S., Sarsour, M., Sharapov, E.I., Snow, W.M., Swanson, H.E., Van Sciver, S., Walbridge, S.B., Yan, H., Zhumabekova, V., "Parity-Violating Neutron Spin-Rotation Measurements at NIST," in "21st International Seminar on Interaction of Neutrons with Nuclei," (21st International Seminar on Interaction of Neutrons with Nuclei, April 2013, Alushta, Ukraine) **ISINN-21**, 19 (2014).
- Creuziger, A., Gnäupel-Herold, T., "Uncertainty in Retained Austenite Measurements Applied to Individual Crystallographic Orientations," in "IOP Conference Series: Materials Science and Engineering," (17th International Conference on Textures of Materials (ICOTOM 17), July 2014, Dresden, Germany) **82**, 012066 (2015).
- Cunningham, N., Wu, Y., Klingensmith, D., Odette, G.R., "On the Remarkable Thermal Stability of Nanostructured Ferritic Alloys," *Mater. Sci. Eng. A-Struct.* **613**, 296 (2014).
- Cunningham, N.J., Etienne, A., Odette, G.R., Stergar, E., Wu, Y., Wirth, B.D., "Characterization of 14YWT As-Atomized, Milled, Milled and Annealed Powders and HIP Consolidated Alloys," *Mater. Res. Soc. Symp. P.* **1298**, 3 (2011).
- Curtis, J.E., Zhang, H., Nanda, H., "SLDMOL: A Tool for the Structural Characterization of Thermally Disordered Membrane Proteins," *Comput. Phys. Commun.* **185**(11), 3010 (2014).
- Dally, R., Hogan, T., Amato, A., Luetkens, H., Baines, C., Rodriguez-Rivera, J., Graf, M.J., Wilson, S.D., "Short-Range Correlations in the Magnetic Ground State of $\text{Na}_4\text{Ir}_3\text{O}_8$," *Phys. Rev. Lett.* **113**(24), 247601 (2014). [CHRNA]
- Das, P., Kanchanavatee, N., Helton, J.S., Huang, K., Baumbach, R.E., Bauer, E.D., White, B.D., Burnett, V.W., Maple, M.B., Lynn, J.W., Janoschek, M., "Chemical Pressure Tuning of URu_2Si_2 via Isoelectronic Substitution of Ru with Fe," *Phys. Rev. B* **91**(8), 085122 (2015).
- Davis, E.M., Kim, J., Oleshko, V.P., Page, K.A., Soles, C.L., "Uncovering the Structure of Nafion-SiO₂ Hybrid Ionomer Membranes for Prospective Large-Scale Energy Storage Devices," *Adv. Funct. Mater.* **25**(26), 4064 (2015).
- Davis, S., Borchers, J.A., Maranville, B.B., Adenwalla, S., "Fast Strain Wave Induced Magnetization Changes in Long Cobalt Bars: Domain Motion versus Coherent Rotation," *J. Appl. Phys.* **117**(6), 063904 (2015).
- De Kruif, C.G., "The Structure of Casein Micelles: a Review of Small-Angle Scattering Data," *J. Appl. Crystallogr.* **47**(5), 1479 (2014).
- DeCaluwe, S.C., Dhar, B.M., Huang, L., He, Y., Yang, K., Owejan, J.P., Zhao, Y., Talin, A.A., Dura, J.A., Wang, H., "Pore Collapse and Regrowth in Silicon Electrodes for Rechargeable Batteries," *Phys. Chem. Chem. Phys.* **17**(17), 11301 (2015).
- DeCaluwe, S.C., Kienzle, P.A., Bhargava, P., Baker, A.M., Dura, J.A., "Phase Segregation of Sulfonate Groups in Nafion Interface Lamellae, Quantified. via Neutron Reflectometry Fitting Techniques for Multi-Layered Structures," *Soft Matter* **10**(31), 5763 (2014).
- de la Iglesia, P., Jaeger, V., Xi, Y., Pfaendtner, J., Pozzo, L.D., "Structure Characterization and Properties of Metal-Surfactant Complexes Dispersed in Organic Solvents," *Langmuir*, in press. [CHRNA]
- Deng, S., Sun, Y., Wu, H., Huang, Q., Yan, J., Shi, K., Malik, M.I., Lu, H., Wang, L., Huang, R., Li, L., Wang, C., "Invar-like Behavior of Antiperovskite $\text{Mn}_{3+x}\text{Ni}_{1-x}\text{N}$ Compounds," *Chem. Mater.* **27**(7), 2495 (2015).
- Dennis, C.L., Krycka, K.L., Borchers, J.A., Desautels, R.D., van Lierop, J., Huls, N.F., Jackson, A.J., Gruettner, C., Ivkov, R., "Internal Magnetic Structure of Nanoparticles Dominates Time-Dependent Relaxation Processes in a Magnetic Field," *Adv. Funct. Mater.* **25**(27), 4300 (2015). [CHRNA]
- Devineni, D., Gonschorek, C., Cicerone, M.T., Xu, Y., Carpenter, J.F., Randolph, T.W., "Storage Stability of Keratinocyte Growth Factor-2 in Lyophilized Formulations: Effects of Formulation Physical Properties and Protein Fraction at the Solid-Air Interface," *Eur. J. Pharm. Biopharm.* **88**(2), 332 (2014). [CHRNA]
- Dhindsa, G.K., Tyagi, M., Chu, X.-Q., "Temperature-Dependent Dynamics of Dry and Hydrated β -Casein Studied by Quasielastic Neutron Scattering," *J. Phys. Chem. B* **118**(37), 10821 (2014). [CHRNA]

- Diallo, S.O., Azuah, R.T., Abernathy, D.L., Taniguchi, J., Suzuki, M., Bossy, J., Mulders, N., Glyde, H.R., "Evidence for a Common Physical Origin of the Landau and BEC Theories of Superfluidity," *Phys. Rev. Lett.* **113**(21), 215302 (2014).
- Diamond, D.J., Baek, J.S., Hanson, A.L., Cheng, L.-Y., Brown, N., Cuadra, A., "Conversion Preliminary Safety Analysis Report for the NIST Research Reactor," BNL-**107265-2015-IR**, 1 (2015).
- Dick, R.A., Datta, S.A.K., Nanda, H., Fang, X., Wen, Y., Barros, M., Wang, Y.-X., Rein, A., Vogt, V.M., "Hydrodynamic and Membrane Binding Properties of Purified Rous Sarcoma Virus Gag Protein," *J. Virol.*, in press.
- Disseler, S.M., Borchers, J.A., Brooks, C.M., Mundy, J.A., Moyer, J.A., Hillsberry, D.A., Thies, E.L., Tenne, D.A., Heron, J., Holtz, M.E., Clarkson, J.D., Stiehl, G.M., Schiffer, P., Muller, D.A., Schlom, D.G., Ratcliff, W.D., "Magnetic Structure and Ordering of Multiferroic Hexagonal LuFeO_3 ," *Phys. Rev. Lett.* **114**(21), 217602 (2015).
- Douglas, J.E., Chater, P.A., Brown, C.M., Pollock, T.M., Seshadri, R., "Nanoscale Structural Heterogeneity in Ni-Rich Half-Heusler TiNiSn ," *J. Appl. Phys.* **116**(16), 163514 (2014).
- Duan, X., Wu, C., Xiang, S., Zhou, W., Yildirim, T., Cui, Y., Yang, Y., Chen, B., Qian, G., "Novel Microporous Metal-Organic Framework Exhibiting High Acetylene and Methane Storage Capacities," *Inorg. Chem.* **54**(9), 4377 (2015).
- Dun, Z.L., Ma, J., Cao, H.B., Qiu, Y., Copley, J.R.D., Hong, T., Matsuda, M., Cheng, J.G., Lee, M., Choi, E.S., Johnston, S., Zhou, H.D., "Competition between the Inter- and Intra-Sublattice Interactions in $\text{Yb}_2\text{V}_2\text{O}_7$," *Phys. Rev. B* **91**(6), 064425 (2015). [CHRNA]
- El-Khatib, S., Phelan, D., Barker, J.G., Zheng, H., Mitchell, J.F., Leighton, C., "Neutron-Scattering-Based Evidence for Interacting Magnetic Excitons in LaCoO_3 ," *Phys. Rev. B*, in press. [CHRNA]
- Emmanuel, S., Anovitz, L.M., Day-Stirrat, R.J., "Effects of Coupled Chemo-Mechanical Processes on the Evolution of Pore-Size Distributions in Geological Media," *Rev. Mineral. Geochem.* **80**(1), 45 (2015).
- Etienne, A., Cunningham, N.J., Wu, Y., Odette, G.R., "Effects of Friction Stir Welding and Post-Weld Annealing on Nanostructured Ferritic Alloy," *Mater. Sci. Technol. Ser.* **27**(4), 724 (2011).
- Fairweather, J., Spornjak, D., Mukundan, R., Spendelow, J., Artyushkova, K., Atanassov, P., Hussey, D., Jacobson, D., Borup, R.L., "Interaction of Heat Generation, MPL, and Water Retention in Corroded PEMFCs," *ECS Transactions* **41**(1), 337 (2011).
- Fajalia, A.I., Antoniou, E., Alexandridis, P., Tsianou, M., "Self-Assembly of Sodium Bis(2-ethylhexyl) Sulfosuccinate in Aqueous Solutions: Modulation of Micelle Structure and Interactions by Cyclodextrins Investigated by Small-Angle Neutron Scattering," *J. Mol. Liq.*, in press. [CHRNA]
- Fajalia, A.I., Tsianou, M., "Charging and Uncharging a Neutral Polymer in Solution: A Small-Angle Neutron Scattering Investigation," *J. Phys. Chem. B* **118**(36), 10725 (2014). [CHRNA]
- Fajalia, A.I., Tsianou, M., "Self-Assembly Control via Molecular Recognition: Effect of Cyclodextrins on Surfactant Micelle Structure and Interactions Determined by SANS," *Colloid Surface. A*, in press. [CHRNA]
- Falk, S.J., Guo, L.Y., Sekulic, N., Smoak, E.M., Mani, T., Logsdon, G.A., Gupta, K., Jansen, L.E.T., Van Duyne, G.D., Vinogradov, S.A., Lampson, M.A., Black, B.E., "CENP-C Reshapes and Stabilizes CENP-A Nucleosomes at the Centromere," *Science* **348**(6235), 699 (2015). [CHRNA]
- Fatemi, V., Hunt, B., Steinberg, H., Eltinge, S.L., Mahmood, F., Butch, N.P., Watanabe, K., Taniguchi, T., Gedik, N., Ashoori, R.C., Jarillo-Herrero, P., "Electrostatic Coupling between Two Surfaces of a Topological Insulator Nanodevice," *Phys. Rev. Lett.* **113**(20), 206801 (2014).
- Fedchak, J.A., Scherschligt, J., Sefa, M., Phandinh, N., "Building a Spring-Transport Package for Spinning Rotor Gauges," *J. Vac. Sci. Technol. A* **33**(3), 033201 (2015).
- FitzGerald, P.A., Chatjaroenporn, K., Warr, G.G., "Structure and Composition of Mixed Micelles of Polymerized and Monomeric Surfactants," *J. Colloid Interf. Sci.* **449**, 377 (2015). [CHRNA]
- Galvin, C.J., Dimitriou, M.D., Satija, S.K., Genzer, J., "Swelling of Polyelectrolyte and Polyzwitterion Brushes by Humid Vapors," *J. Am. Chem. Soc.* **136**(36), 12737 (2014).
- Ganguly, S., Das, N.C., "A Comparison on Self-Seeding and Isothermal Crystallization of Polyethylene in Solution using Small Angle Neutron Scattering," *Polymer* **61**, 192 (2015).

- Gao, J., Ndong, R.S., Shiflett, M.B., Wagner, N.J., "Creating Nanoparticle Stability in Ionic Liquid [C₄mim][BF₄] by Inducing Solvation Layering," *ACS Nano* **9**(3), 3243 (2015). [CHNRNS]
- Garg, S., Castro-Roman, F., Porcar, L., Butler, P., Bautista, P.J., Krzyzanowski, N., Perez-Salas, U., "Cholesterol Solubility Limit in Lipid Membranes Probed by Small Angle Neutron Scattering and MD Simulations," *Soft Matter* **10**(46), 9313 (2014). [CHNRNS]
- Gavrin, V., Cleveland, B., Danshin, S., Elliott, S., Gorbachev, V., Ibragimova, T., Kalikhov, A., Knodel, T., Kozlova, Yu., Malyshkin, Yu., Matveev, V., Mirmov, I., Nico, J., Robertson, R.G.H., Shikhin, A., Sinclair, D., Veretenkin, E., Wilkerson, J., "Current Status of New SAGE Project with ⁵¹Cr Neutrino Source," *Phys. Part. Nuclei* **46**(2), 131 (2015).
- Gentile, T.R., Bales, M.J., Breuer, H., Chupp, T.E., Coakley, K.J., Cooper, R.L., Nico, J.S., O'Neill, B., "Nonproportionality in the Scintillation Light Yield of Bismuth Germanate," *Nucl. Instrum. Meth. A* **784**, 88 (2015).
- Gibson, Q.D., Wu, H., Liang, T., Ali, M.N., Ong, N.P., Huang, Q., Cava, R.J., "Magnetic and Electronic Properties of CaMn₂Bi₂: A Possible Hybridization Gap Semiconductor," *Phys. Rev. B* **91**(8), 085128 (2015).
- Gillard, T.M., Medapuram, P., Morse, D.C., Bates, F.S., "Fluctuations, Phase Transitions, and Latent Heat in Short Diblock Copolymers: Comparison of Experiment, Simulation and Theory," *Macromolecules* **48**(8), 2801 (2015).
- Gitgeatpong, G., Zhao, Y., Avdeev, M., Piltz, R.O., Sato, T.J., Matan, K., "Magnetic Structure and Dzyaloshinskii-Moriya Interaction in the S=1/2 Helical-Honeycomb Antiferromagnet α -Cu₂V₂O₇," *Phys. Rev. B* **92**(2), 024423 (2015).
- Glinka, C.J., Barker, J.G., Mildner, D.F.R., "Comparison of Pinhole Collimation and Focusing Optics for SANS," *Nucl. Instrum. Meth. A*, in press. [CHNRNS]
- Gomez-Gualdrón, D.A., Gutov, O.V., Krungleviciute, V., Borah, B., Mondloch, J.E., Hupp, J.T., Yildirim, T., Farha, O.K., Snurr, R.Q., "Computational Design of Metal-Organic Frameworks Based on Stable Zirconium Building Units for Storage and Delivery of Methane," *Chem. Mater.* **26**(19), 5632 (2014).
- Graf, M.J., Disseler, S.M., Dhital, C., Hogan, T., Bojko, M., Amato, A., Luetkens, H., Baines, C., Margineda, D., Giblin, S.R., Jura, M., Wilson, S.D., "Magnetism and Magnetic Order in the Pyrochlore Iridates in the Insulator-to-Metal Crossover Region," *J. Phys. Conf. Ser.* **551**(1), 012020 (2014).
- Gressier, V., Bonaldi, A.C., Dewey, M.S., Gilliam, D.M., Harano, H., Masuda, A., Matsumoto, T., Moiseev, N., Nico, J.S., Ntote, R., Oberstedt, S., Roberts, N.J., Röttger, S., Thomas, D.J., "International Key Comparison of Neutron Fluence Measurements in Monoenergetic Neutron Fields - CCRI(III)-K11," *Metrologia* **51**(06009), 431 (2014).
- Grutter, A.J., Kirby, B.J., Gray, M.T., Flint, C.L., Alaan, U.S., Suzuki, Y., Borchers, J.A., "Electric Field Control of Interfacial Ferromagnetism in CaMnO₃/CaRuO₃ Heterostructures," *Phys. Rev. Lett.* **115**(4), 047601 (2015).
- Gu, X., Cole, D.R., Rother, G., Mildner, D.F.R., Brantley, S.L., "Pores in Marcellus Shale: A Neutron Scattering and FIB-SEM Study," *Energ. Fuel* **29**(3), 1295 (2015). [CHNRNS]
- Gunasekera, J., Harriger, L., Heitmann, T., Dahal, A., Knoll, H., Singh, D.K., "Quasilocall Critical Nature of Cooperative Paramagnetic Fluctuations in CaRuO₃ Metal," *Phys. Rev. B* **91**(24), 241103 (2015).
- Gutov, O.V., Bury, W., Gomez-Gualdrón, D.A., Krungleviciute, V., Fairen-Jimenez, D., Mondloch, J.E., Sarjeant, A.A., Al-Juaid, S.S., Snurr, R.Q., Hupp, J.T., Yildirim, T., Farha, O.K., "Water-Stable Zirconium-Based Metal-Organic Framework Material with High-Surface Area and Gas-Storage Capacities," *Chem.-Eur. J.* **20**(39), 12389 (2014).
- Haddock, C., Snow, W.M., Anderson, E., Barrón-Palos, L., Bass, C.D., Crawford, B.E., Esposito, D., Fox, W., Fry, J.A., Gardner, H., Holley, A.T., Heckel, B.R., Lieffers, J., Magers, S., Maldonado-Velázquez, M., Malone, R., Markoff, D.M., Mumm, H.P., Nico, J.S., Olek, D., Paudel, C., Penn, S., Rout, P.C., Santra, S., Sarsour, M., Sprow, A., Swanson, H.E., Van Sciver, S., Vanderwerp, J., "Searches for Exotic Interactions using Neutron Spin Rotation," in "XXXIV Physics in Collision Symposium," (XXXIV Physics in Collision Symposium, August 2014, Bloomington, Indiana), **1** (2014).
- Hammouda, B., Jia, D., Cheng, H., "Single-Chain Conformation for Interacting Poly(N-Isopropylacrylamide) in Aqueous Solution," *The Open Access Journal of Science and Technology* **3**, 101152 (2015).

- Hasz, K., Ijiri, Y., Krycka, K.L., Borchers, J.A., Booth, R.A., Oberdick, S., Majetich, S.A., "Particle Moment Canting in CoFe_2O_4 Nanoparticles," *Phys. Rev. B* **90**(18), 180405 (2014). [CHRNA]
- Hayes, D.G., Gomez del Rio, J.A., Ye, R., Urban, V.S., Pingali, S.V., O'Neill, H.M., "Effect of Protein Incorporation on the Nanostructure of the Bicontinuous Microemulsion Phase of Winsor-III Systems: A Small-Angle Neutron Scattering Study," *Langmuir* **31**(6), 1901 (2015). [CHRNA]
- He, T., Wu, H., Wu, G., Li, Z., Zhou, W., Ju, X., Xie, D., Chen, P., "Lithium Amidoborane Hydrazinates: Synthesis, Structure and Hydrogen Storage Properties," *J. Mater. Chem. A* **3**(18), 10100 (2015).
- He, Y., Zhou, W., Qian, G., Chen, B., "Methane Storage in Metal-Organic Frameworks," *Chem. Soc. Rev.* **43**(16), 5657 (2014).
- He, Y., Downing, R.G., Wang, H., "3D Mapping of Lithium in Battery Electrodes using Neutron Activation," *J. Power Sources*, in press.
- Heinrich, F., "Deuteration in Biological Neutron Reflectometry," in "Methods in Enzymology," (Elsevier, Inc., Atlanta, GA), in press.
- Heinrich, F., Lösche, M., "Zooming in on Disordered Systems: Neutron Reflection Studies of Proteins Associated with Fluid Membranes," *BBA-Biomembranes* **1838**(9), 2341 (2014).
- Heller, W.T., Urban, V.S., Lynn, G.W., Weiss, K.L., O'Neill, H.M., Pingali, S.V., Qian, S., Littrell, K.C., Melnichenko, Y.B., Buchanan, M.V., Selby, D.L., Wignall, G.D., Butler, P.D., Myles, D.A., "The Bio-SANS Instrument at the High Flux Isotope Reactor of Oak Ridge National Laboratory," *J. Appl. Crystallogr.* **47**(4), 1238 (2014).
- Hellsing, M.S., Kwaambwa, H.M., Nermark, F.M., Nkoane, B.B.M., Jackson, A.J., Wasbrough, M.J., Berts, I., Porcar, L., Rennie, A.R., "Structure of Flocs of Latex Particles Formed by Addition of Protein from Moringa Seeds," *Colloid Surface. A* **460**, 460 (2014). [CHRNA]
- Helton, J.S., Pajerowski, D.M., Qiu, Y., Zhao, Y., Shulyatev, D.A., Mukovskii, Y.M., Bychkov, G.L., Barilo, S.N., Lynn, J.W., "Polaron-Mediated Spin Correlations in Metallic and Insulating $\text{La}_{1-x}\text{A}_x\text{MnO}_3$ ($\text{A}=\text{Ca}, \text{Sr}, \text{or Ba}$)," *Phys. Rev. B* **90**(21), 214411 (2014).
- Hu, L., Chen, J., Fan, L., Ren, Y., Huang, Q., Sanson, A., Jiang, Z., Zhou, M., Rong, Y., Wang, Y., Deng, J., Xing, X., "High-Curie-Temperature Ferromagnetism in $(\text{Sc}, \text{Fe})\text{F}_3$ Fluorides and its Dependence on Chemical Valence," *Adv. Mater.*, in press.
- Hu, T.-L., Wang, H., Li, B., Krishna, R., Wu, H., Zhou, W., Zhao, Y., Han, Y., Wang, X., Zhu, W., Yao, Z., Xiang, S., Chen, B., "Microporous Metal-Organic Framework with Dual Functionalities for Highly Efficient Removal of Acetylene from Ethylene/Acetylene Mixtures," *Nat. Commun.* **6**(7328), 1 (2015). [CHRNA]
- Huber, M.G., Arif, M., Chen, W.C., Gentile, T.R., Hussey, D.S., Black, T.C., Pushin, D.A., Shahi, C.B., Wietfeldt, F.E., Yang, L., "Neutron Interferometric Measurement of the Scattering Length Difference between the Triplet and Singlet States of $n\text{-}^3\text{He}$," *Phys. Rev. C* **90**(6), 064004 (2014).
- Huffman, P.R., Coakley, K.J., Doyle, J.M., Huffer, C.R., Mumm, H.P., O'Shaughnessy, C.M., Schelhammer, K.W., Seo, P.-N., Yang, L., "Design and Performance of a Cryogenic Apparatus for Magnetically Trapping Ultracold Neutrons," *Cryogenics* **64**, 40 (2014).
- Hulvey, Z., Vlaisavljevich, B., Mason, J.A., Tsivion, E., Dougherty, T.P., Bloch, E.D., Head-Gordon, M., Smit, B., Long, J.R., Brown, C.M., "Critical Factors Driving the High Volumetric Uptake of Methane in $\text{Cu}_3(\text{btc})_2$," *J. Am. Chem. Soc.*, in press.
- Hussey, D.S., Jacobson, D.L., "Applications of Neutron Imaging and Future Possibilities," *Neutron News* **26**(2), 19 (2015).
- Hyland, L.L., Taraban, M.B., Yu, Y.B., "Using Small-Angle Scattering Techniques to Understand Mechanical Properties of Biopolymer-Based Biomaterials," *Soft Matter* **9**(43), 10218 (2013).
- Jalarvo, N., Tyagi, M., Crawford, M.K., "Quasielastic Neutron Scattering Study of POSS Ligand Dynamics," *EPJ Web Conf.* **83**, 02007 (2015). [CHRNA]
- Jeffries, J.R., Butch, N.P., Lipp, M., Bradley, J., Kirshenbaum, K., Saha, S.R., Paglione, J., Kenny-Benson, C., Xiao, Y., Chow, P., Evans, W.J., "Persistent Fe Moments in the Normal-State Collapsed-Tetragonal Phase of the Pressure-Induced Superconductor $\text{Ca}_{0.067}\text{Sr}_{0.33}\text{Fe}_2\text{As}_2$," *Phys. Rev. B* **90**(14), 144506 (2014).

- Jeffries, J.R., Butch, N.P., Vohra, Y.K., Weir, S.T., "Pressure Evolution of Electrical Transport in the 3D Topological Insulator $(\text{Bi,Sb})_2(\text{Se,Te})_3$," J. Phys. Conf. Ser. **592**, 012124 (2015).
- Jeffries, J.R., Veiga, L.S.I., Fabbris, G., Haskel, D., Huang, P., Butch, N.P., McCall, S.K., Holliday, K., Jenei, Z., Xiao, Y., Chow, P., "Robust Ferromagnetism in the Compressed Permanent Magnet $\text{Sm}_2\text{Co}_{17}$," Phys. Rev. B **90**(10), 104408 (2014).
- Jeong, Y., Gnäupel-Herold, T., Barlat, F., Iadicola, M., Creuziger, A., Lee, M.-G., "Evaluation of Biaxial Flow Stress Based on Elasto-Viscoplastic Self-Consistent Analysis of X-ray Diffraction Measurements," Int. J. Plasticity **66**, 103 (2015).
- Jiang, N., Endoh, M.K., Koga, T., Masui, T., Kishimoto, H., Nagao, M., Satija, S.K., Taniguchi, T., "Nanostructures and Dynamics of Macromolecules Bound to Attractive Filler Surfaces," ACS Macro Lett., in press. [CHRRNS]
- Jiang, N., Sendogdular, L., Di, X., Sen, M., Gin, P., Endoh, M.K., Koga, T., Akgun, B., Dimitriou, M., Satija, S., "Effect of CO_2 on a Mobility Gradient of Polymer Chains near an Impenetrable Solid," Macromolecules **48**(6), 1795 (2015).
- Jiang, Z., Hess, S.K., Heinrich, F., Lee, J.C., "Molecular Details of α -Synuclein Membrane Association Revealed by Neutrons and Photons," J. Phys. Chem. B **119**(14), 4812 (2015).
- Jiao, Y., Akcora, P., "Understanding the Role of Grafted Polystyrene Chain Conformation in Assembly of Magnetic Nanoparticles," Phys. Rev. E **90**(4), 042601 (2014).
- Jin, S.F., Huang, Q., Lin, Z.P., Li, Z.L., Wu, X.Z., Ying, T.P., Wang, G., Chen, X.L., "Two-Dimensional Magnetic Correlations and Partial Long-Range Order in Geometrically Frustrated CaOFeS with Triangle Lattice of Fe Ions," Phys. Rev. B **91**(9), 094420 (2015).
- Johnston, T.P., "Reactor Health Physics Operations at the NIST Center for Neutron Research," Health Phys. **108**(1), S19 (2015).
- Jones, S.Z., Bentz, D.P., Snyder, K.A., Martys, N.S., Hussey, D.S., Jacobson, D.L., "Service Life Modeling of Reinforced High Volume Fly Ash (HVFA) Concrete Structures Containing Cracks," in "International Concrete Sustainability Conference," in press.
- Kabirian, F., Khan, A.S., "Anisotropic Yield Criteria in σ - τ Stress Space for Materials with Yield Asymmetry," Int. J. Solids Struct., in press.
- Kabirian, F., Khan, A.S., Gnäupel-Herold, T.H., "Visco-Plastic Modeling of Mechanical Responses and Texture Evolution of Extruded AZ31 Magnesium Alloy for Various Loading Conditions," Int. J. Plasticity **68**, 1 (2015).
- Kaizu, K., Alexandridis, P., "Glucose-Induced Sphere to Ellipsoid Transition of Polyoxyethylene-Polyoxypropylene Block Copolymer Micelles in Aqueous Solutions," Colloid Surface. A, in press. [CHRRNS]
- Kapelewski, M.T., Geier, S.J., Hudson, M.R., Stück, D., Mason, J.A., Nelson, J.N., Xiao, D.J., Hulvey, Z., Gilmour, E., FitzGerald, S.A., Head-Gordon, M., Brown, C.M., Long, J.R., " M_2 (m -dobdc) ($M = \text{Mg, Mn, Fe, Co, Ni}$) Metal-Organic Frameworks Exhibiting Increased Charge Density and Enhanced H_2 Binding at the Open Metal Sites," J. Am. Chem. Soc. **136**(34), 12119 (2014).
- Karabiyik, U., Mao, M., Satija, S.K., Esker, A.R., "Determination of Thicknesses and Refractive Indices of Polymer Thin Films by Multiple Incident Media Ellipsometry," Thin Solid Films **565**, 72 (2014).
- Karabiyik, U., Paul, R., Swift, M.C., Satija, S.K., Esker, A.R., "Effects of POSS Nanoparticles on Glass Transition Temperatures of Ultrathin Poly(*t*-Butyl Acrylate) Films and Bulk Blends," J. Polym. Sci. Pol. Phys. **53**(3), 175 (2015).
- Khodadadi, S., Sokolov, A.P., "Protein Dynamics: from Rattling in a Cage to Structural Relaxation," Soft Matter **11**(25), 4984 (2015). [CHRRNS]
- Kihm, K.D., Hight, B., Kirchoff, E., Yi, H., Rosenfeld, J., Rawal, S., Hussey, D., Jacobson, D., Bilheux, H., Walker, L., Voisin, S., Pratt, D., Swanson, A., "Neutron Tomography of Lithium (Li) Coolant inside a Niobium (Nb) Heat Pipe," J. Heat Transf. **136**(8), 080903 (2014).
- Kihm, K.D., Hussey, D.S., Pratt, D.M., Swanson, A.D., "Neutron Imaging of Progressive Mixing of H_2O and D_2O inside a Metal (Al) Container," J. Heat Transf. **134**(8), 080904 (2012).

- Kim, J.M., Eberle, A.P.R., Gurnon, A.K., Porcar, L., Wagner, N.J., "The Microstructure and Rheology of a Model, Thixotropic Nanoparticle Gel under Steady Shear and Large Amplitude Oscillatory Shear (LAOS)," *J. Rheol.* **58**(5), 1301 (2014).
- Kim, J., Merger, D., Wilhelm, M., Helgeson, M.E., "Microstructure and Nonlinear Signatures of Yielding in a Heterogeneous Colloidal Gel under Large Amplitude Oscillatory Shear," *J. Rheol.* **58**(5), 1359 (2014). [CHRS]
- Kim, M.G., Kreyssig, A., Thaler, A., Pratt, D.K., Tian, W., Zarestky, J.L., Green, M.A., Bud'ko, S.L., Canfield, P.C., McQueeney, R.J., Goldman, A.I., "Antiferromagnetic Ordering in the Absence of Structural Distortion in $\text{Ba}(\text{Fe}_{1-x}\text{Mn}_x)_2\text{As}_2$," *Phys. Rev. B* **82**(22), 220503 (2010).
- King, Jr., H.E., Eberle, A.P.R., Walters, C.C., Kliewer, C.E., Ertas, D., Huynh, C., "Pore Architecture and Connectivity in Gas Shale," *Energ. Fuel.* **29**(3), 1375 (2015). [CHRS]
- Kirby, B.J., Greene, P.K., Maranville, B.B., Davis, J.E., Liu, K., "Effective Anisotropy Gradient in Pressure Graded [Co/Pd] Multilayers," *J. Appl. Phys.* **117**(6), 063905 (2015).
- Kline, S.R., "2014 Accomplishments and Opportunities," *NIST SP* **1177**, (2014).
- Koh, M.L., Jolliffe, K.A., Perrier, S., "Hierarchical Assembly of Branched Supramolecular Polymers from (Cyclic Peptide)-Polymer Conjugates," *Biomacromolecules* **15**(11), 4002 (2014). [CHRS]
- Koshari, S.H.S., Wagner, N.J., Lenhoff, A.M., "Characterization of Lysozyme Adsorption in Cellulosic Chromatographic Materials using Small-Angle Neutron Scattering," *J. Chromatogr. A* **1399**, 45 (2015). [CHRS]
- Kotaka, T., Tabuchi, Y., Pasaogullari, U., Wang, C.-Y., "Impact of Interfacial Water Transport in PEMFCs on Cell Performance," *Electrochim. Acta* **146**, 618 (2014).
- Krakowiak, K.J., Thomas, J.J., Musso, S., James, S., Akono, A.-T., Ulm, F.-J., "Nano-Chemo-Mechanical Signature of Conventional Oil-Well Cement Systems: Effects of Elevated Temperature and Curing Time," *Cement Concrete Res.* **67**, 103 (2015).
- Krueger, S., Shin, J.-H., Curtis, J.E., Robinson, K.A., Kelman, Z., "The Solution Structure of Full-Length Dodecameric MCM by SANS and Molecular Modeling," *Proteins* **82**(10), 2364 (2014). [CHRS]
- Kruk, I.I., Zajdel, P., "Single Crystal Growth and Structural Characterization of Iron Telluride Doped with Chromium and Zinc," *J. Cryst. Growth* **401**, 608 (2014).
- Krycka, K.L., Borchers, J.A., Booth, R.A., Ijiri, Y., Hasz, K., Rhyne, J.J., Majetich, S.A., "Origin of Surface Canting within Fe_2O_4 Nanoparticles," *Phys. Rev. Lett.* **113**(14), 147203 (2014).
- Krycka, K.L., Borchers, J.A., Booth, R.A., Ijiri, Y., Hasz, K., Rhyne, J.J., Majetich, S.A., "Reply to 'Comment on 'Origin of Surface Canting within Fe_2O_4 Nanoparticles,'" *Phys. Rev. Lett.* **114**(14), 149702 (2015).
- Krzyzanowski, N., Porcar, L., Garg, S., Butler, P., Castro-Roman, F., Bautista, P.J., Perez-Salas, U., "Reply to the 'Comment on 'Cholesterol Solubility Limit in Lipid Membranes Probed by Small Angle Neutron Scattering and MD Simulations'" by R. Epand, *Soft Matter*, 2015, 11, DOI: 10.1039/C4SM02819H," *Soft Matter* **11**(27), 5582 (2015).
- Kučera, J., Bennett, J.W., Ofiaz, R., Paul, R.L., De Nadai Fernandes, E.A., Kubešová, M., Bacchi, M.A., Stopic, A.J., Sturgeon, R.E., Grinberg, P., "Elemental Characterization of Single-Wall Carbon Nanotube Certified Reference Material by Neutron and Prompt γ Activation Analysis," *Anal. Chem.* **87**(7), 3699 (2015).
- Kumari, H., Deakyne, C.A., Atwood, J.L., "Solution Structures of Nanoassemblies Based on Pyrogallol[4]arenes," *Accounts Chem. Res.* **47**(10), 3080 (2014). [CHRS]
- Kumi, B.C., Hammouda, B., Greer, S.C., "Self-Assembly of the Triblock Copolymer 17R4 Poly(Propylene Oxide)₁₄-Poly(Ethylene Oxide)₂₄-Poly(Propylene Oxide)₁₄ in D_2O ," *J. Colloid Interf. Sci.* **434**, 201 (2014). [CHRS]
- LaManna, J.M., Mench, M.M., "Engineering Net Water Balance in Polymer Electrolyte Fuel Cells," *ECS Transactions* **64**(3), 451 (2014).
- Langford, T.J., Bass, C.D., Beise, E.J., Breuer, H., Erwin, D.K., Heimbach, C.R., Nico, J.S., "Fast Neutron Detection with a Segmented Spectrometer," *Nucl. Instrum. Meth. A* **771**, 78 (2015).
- Larson, A.M., Moetakef, P., Gaskell, K., Brown, C.M., King, G., Rodriguez, E.E., "Inducing Ferrimagnetism in Insulating Hollandite $\text{Ba}_{1.2}\text{Mn}_8\text{O}_{16}$," *Chem. Mater.* **27**(2), 515 (2015).

- Lavelle, C.M., Coplan, M., Miller, E.C., Thompson, A.K., Kowler, A.L., Vest, R.E., Yue, A.T., Koeth, T., Al-Sheikhly, M., Clark, C.W., "Demonstration of Neutron Detection Utilizing Open Cell Foam and Noble Gas Scintillation," *Appl. Phys. Lett.* **106**(9), 094103 (2015).
- Lawler, K.V., Hulvey, Z., Forster, P.M., "On the Importance of a Precise Crystal Structure for Simulating Gas Adsorption in Nanoporous Materials," *Phys. Chem. Chem. Phys.*, in press.
- Lee, C.-H., Wu, C.-M., Hsu, D., Wang, C.-W., Wang, C.-J., Li, W.-H., Yang, C.-C., Sun, J., Lynn, J.W., "Neutron Diffraction Study of the Mn Spin Correlations in $\text{Bi}_{0.46}\text{Ca}_{0.54}\text{Mn}_{0.95}\text{Cr}_{0.05}\text{O}_3$," *J. Phys. Soc. Jpn.* **80**, SB013 (2011).
- Lee, H.-T., Kilburn, D., Behrouzi, R., Briber, R.M., Woodson, S.A., "Molecular Crowding Overcomes the Destabilizing Effects of Mutations in a Bacterial Ribozyme," *Nucleic Acids Res.* **43**(2), 1170 (2015).
- Lee, J.S., Lee, N.-H., Peri, S., Foster, M.D., Majkrzak, C.F., Hu, R., Wu, D.T., "Surface Segregation Driven by Molecular Architecture Asymmetry in Polymer Blends," *Phys. Rev. Lett.* **113**(22), 225702 (2014).
- Lee, J.S., Vlaisavljevich, B., Britt, D.K., Brown, C.M., Haranczyk, M., Neaton, J.B., Smit, B., Long, J.R., Queen, W.L., "Understanding Small-Molecule Interactions in Metal-Organic Frameworks: Coupling Experiment with Theory," *Adv. Mater.*, in press.
- Leiner, J., Thampy, V., Christianson, A.D., Abernathy, D.L., Stone, M.B., Lumsden, M.D., Sefat, A.S., Sales, B.C., Hu, J., Mao, Z., Bao, W., Broholm, C., "Modified Magnetism within the Coherence Volume of Superconducting $\text{Fe}_{1+\delta}\text{Se}_x\text{Te}_{1-x}$," *Phys. Rev. B* **90**(10), 100501 (2014). [CHRN]
- Leos, N.G., White, J.S., Lim, J.A., Gavilano, J.L., Delley, B., Lemberger, L., Holmes, A.T., Medarde, M., Loew, T., Hinkov, V., Lin, C., Laver, M., Dewhurst, C.D., Forgan, E.M., "Influence of the Fermi Surface Morphology on the Magnetic Field-Driven Vortex Lattice Structure Transitions in $\text{YBa}_2\text{Cu}_3\text{O}_{7-\delta}$: $\delta = 0, 0.15$," *J. Phys. Soc. Jpn.* **84**(4), 044709 (2015). [CHRN]
- Levine, Z.A., Venable, R.M., Watson, M.C., Lerner, M.G., Shea, J.-E., Pastor, R.W., Brown, F.L.H., "Determination of Biomembrane Bending Moduli in Fully Atomistic Simulations," *J. Am. Chem. Soc.* **136**(39), 13582 (2014).
- Li, B., Wen, H.-M., Wang, H., Wu, H., Yildirim, T., Zhou, W., Chen, B., "Porous Metal-Organic Frameworks with Lewis Basic Nitrogen Sites for High-Capacity Methane Storage," *Energ. Environ. Sci.*, in press.
- Li, B., Wen, H.-M., Zhou, W., Chen, B., "Porous Metal-Organic Frameworks for Gas Storage and Separation: What, How and Why?," *J. Phys. Chem. Lett.* **5**(20), 3468 (2014).
- Li, H., Zhang, L.-L., Yi, Z., Fratini, E., Baglioni, P., Chen, S.-H., "Translational and Rotational Dynamics of Water Contained in Aged Portland Cement Pastes Studied by Quasi-Elastic Neutron Scattering," *J. Colloid Interf. Sci.*, in press. [CHRN]
- Li, J., Smith, A.E., Jiang, P., Stalick, J.K., Sleight, A.W., Subramanian, M.A., "True Composition and Structure of Hexagonal YAlO_3 ," Actually $\text{Y}_3\text{Al}_3\text{O}_8\text{CO}_3$," *Inorg. Chem.* **54**(3), 837 (2015).
- Li, M.-R., Retuerto, M., Deng, Z., Stephens, P.W., Croft, M., Huang, Q., Wu, H., Deng, X., Kotliar, G., Sánchez-Benítez, J., Hadermann, J., Walker, D., Greenblatt, M., "Giant Magnetoresistance in the Half-Metallic Double-Perovskite Ferrimagnet $\text{Mn}_2\text{FeReO}_6$," *Angew. Chem. Int. Edit.*, in press.
- Li, P., He, Y., Zhao, Y., Weng, L., Wang, H., Krishna, R., Wu, H., Zhou, W., O'Keeffe, M., Han, Y., Chen, B., "A Rod-Packing Microporous Hydrogen-Bonded Organic Framework for Highly Selective Separation of $\text{C}_2\text{H}_2/\text{CO}_2$ at Room Temperature," *Angew. Chem. Int. Edit.* **54**(2), 574 (2015).
- Li, X., Do, C., Liu, Y., Sánchez-Díaz, L., Smith, G., Chen, W.-R., "A Scattering Function of Star Polymers including Excluded Volume Effects," *J. Appl. Crystallogr.* **47**(4), 1901 (2014).
- Li, X., Sánchez-Díaz, L.E., Wu, B., Hamilton, W.A., Falus, P., Porcar, L., Liu, Y., Do, C., Faraone, A., Smith, G.S., Egami, T., Chen, W.-R., "Dynamical Threshold of Diluteness of Soft Colloids," *ACS Macro Lett.* **3**(12), 1271 (2014). [CHRN]
- Lin, K., Rong, Y., Wu, H., Huang, Q., You, L., Ren, Y., Fan, L., Chen, J., Xing, X., "Ordered Structure and Thermal Expansion in Tungsten Bronze $\text{Pb}_2\text{K}_{0.5}\text{Li}_{0.5}\text{Nb}_5\text{O}_{15}$," *Inorg. Chem.* **53**(17), 9174 (2014).
- Lindstrom, R.M., Şahin, D., "Measuring the Half-Life of ^{111m}Pd , Invited," *T. Am. Nucl. Soc.* **109**, 538 (2013).

- Liu, C.K., Warr, G.G., "Self-Assembly of Didodecyldimethylammonium Surfactants Modulated by Multivalent, Hydrolyzable Counterions," *Langmuir* **31**(10), 2936 (2015). [CHRNA]
- Liu, D.M., Zhang, H., Wang, S.B., Xiao, W.Q., Zhang, Z.L., Tian, N., Liu, C.X., Yue, M., Huang, Q.Z., Zhang, J.X., Lynn, J.W., "The Effect of Al Doping on the Crystal Structure and Magnetocaloric Behavior of $Mn_{1.2}Fe_{0.8}P_{1-x}Ge_x$ Compounds," *J. Alloy Compd.* **633**, 120 (2015).
- Liu, D.X., Wang, J., Pan, K., Qiu, J., Canova, M., Cao, L.R., Co, A.C., "In Situ Quantification and Visualization of Lithium Transport with Neutrons," *Angew. Chem. Int. Edit.* **53**(36), 9498 (2014).
- López-Barrón, C.R., Brant, P., Eberle, A.P.R., Crowther, D.J., "Linear Rheology and Structure of Molecular Bottlebrushes with Short Side Chains," *J. Rheol.* **59**(3), 865 (2015).
- López-Barrón, C.R., Li, D., Wagner, N.J., Caplan, J.L., "Triblock Copolymer Self-Assembly in Ionic Liquids: Effect of PEO Block Length on the Self-Assembly of PEO-PPO-PEO in Ethylammonium Nitrate," *Macromolecules* **47**(21), 7484 (2014). [CHRNA]
- Lu, J., Bates, F.S., Lodge, T.P., "Remarkable Effect of Molecular Architecture on Chain Exchange in Triblock Copolymer Micelles," *Macromolecules* **48**(8), 2667 (2015). [CHRNA]
- Lu, X.F., Wang, N.Z., Wu, H., Wu, Y.P., Zhao, D., Zeng, X.Z., Luo, X.G., Wu, T., Bao, W., Zhang, G.H., Huang, F.Q., Huang, Q. Z., Chen, X.H., "Coexistence of Superconductivity and Antiferromagnetism in $(Li_{0.8}Fe_{0.2}) OHFeSe$," *Nat. Mater.* **14**(3), 325 (2015).
- Luo, J., Yuan, G., Zhao, C., Han, C.C., Chen, J., Liu, Y., "Gelation of Large Hard Particles with Short-Range Attraction Induced by Bridging of Small Soft Microgels," *Soft Matter* **11**(12), 2494 (2015). [CHRNA]
- Ma, J., Lee, J.H., Hahn, S.E., Hong, T., Cao, H.B., Aczel, A.A., Dun, Z.L., Stone, M.B., Tian, W., Qiu, Y., Copley, J.R.D., Zhou, H.D., Fishman, R.S., Matsuda, M., "Strong Competition between Orbital Ordering and Itinerancy in a Frustrated Spinel Vanadate," *Phys. Rev. B* **91**(2), 020407 (2015). [CHRNA]
- Malo de Molina, P., Lad, S., Helgeson, M.E., "Heterogeneity and its Influence on the Properties of Difunctional Poly(Ethylene Glycol) Hydrogels: Structure and Mechanics," *Macromolecules*, in press. [CHRNA]
- Mansour, A.N., Wong-Ng, W., Huang, Q., Tang, W., Thompson, A., Sharp, J., "Structural Characterization of Bi_2Te_3 and Sb_2Te_3 as a Function of Temperature using Neutron Powder Diffraction and Extended X-ray Absorption Fine Structure Techniques," *J. Appl. Phys.* **116**(8), 083513 (2014).
- Martin, T.B., Mongcopa, K.I.S., Ashkar, R., Butler, P., Krishnamoorti, R., Jayaraman, A., "Wetting-Dewetting and Dispersion-Aggregation Transitions are Distinct for Polymer Grafted Nanoparticles in Chemically Dissimilar Polymer Matrix," *J. Am. Chem. Soc.*, in press.
- Maruyama, S., Anbusathaiah, V., Fennell, A., Enderle, M., Takeuchi, I., Ratcliff, W.D., "Change in the Magnetic Structure of $(Bi,Sm)FeO_3$ Thin Films at the Morphotropic Phase Boundary Probed by Neutron Diffraction," *APL Materials* **2**(11), 116106 (2014).
- McCabe, E.E., Stock, C., Bettis, Jr., J.L., Whangbo, M.-H., Evans, J.S.O., "Magnetism of the Fe^{2+} and Ce^{3+} Sublattices in $Ce_2O_2FeSe_2$: A Combined Neutron Powder Diffraction, Inelastic Neutron Scattering, and Density Functional Study," *Phys. Rev. B* **90**(23), 235115 (2014).
- McNally, D.E., Simonson, J.W., Post, K.W., Yin, Z.P., Pezzoli, M., Smith, G.J., Leyva, V., Marques, C., DeBeer-Schmitt, L., Kolesnikov, A.I., Zhao, Y., Lynn, J.W., Basov, D.N., Kotliar, G., Aronson, M.C., "Origin of the Charge Gap in $LaMnPO_4$," *Phys. Rev. B* **90**(18), 180403 (2014).
- Micklitsch, C.M., Medina, S.H., Yucel, T., Nagy-Smith, K.J., Pochan, D.J., Schneider, J.P., "Influence of Hydrophobic Face Amino Acids on the Hydrogelation of β -Hairpin Peptide Amphiphiles," *Macromolecules* **48**(5), 1281 (2015). [CHRNA]
- Mihailescu, M., Krepiy, D., Milescu, M., Gawrisch, K., Swartz, K.J., White, S.H., "Structural Interactions of a Voltage Sensor Toxin with Lipid Membranes," *P. Natl. A. Sci. USA* **111**(50), E5463 (2014).
- Mildner, D.F.R., "Resolution of Small-Angle Neutron Scattering with a Reflective Focusing Optic," *J. Appl. Crystallogr.* **47**(4), 1247 (2014). [CHRNA]
- Miyatsu, S., Kofu, M., Nagoe, A., Yamada, T., Sadakiyo, M., Yamada, T., Kitagawa, H., Tyagi, M., García Sakai, V., Yamamuro, O., "Proton Dynamics of Two-Dimensional Oxalate-Bridged Coordination Polymers," *Phys. Chem. Chem. Phys.* **16**(32), 17295 (2014). [CHRNA]

- Mohammad, I., Romero-Talamas, C., Kostov, D., Wang, W., Liu, Z., Hussey, D.S., Baltic, E., Jacobson, D.L., Gu, J., Choa, F.-S., "Global Nuclear Radiation Monitoring using Plants," in "Proceedings of. SPIE," edited by Vo-Dinh, T., Lieberman, R.A., Gauglitz, G.G., (Advanced Environmental, Chemical, and Biological Sensing Technologies XII, May 2015, Baltimore, MD) **9486**, 94860S (2015).
- Mumm, H.P., Huber, M.G., Yue, A.T., Thompson, A.K., Dewey, M.S., Huffer, C.R., Huffman, P.R., Schelhammer, K.W., O'Shaughnessy, C., Coakley, K.J., "Measuring the Neutron Lifetime with Magnetically Trapped Ultracold Neutrons," in "Workshop on Next Generation Experiments to Measure the Neutron Lifetime," (Workshop on Next Generation Experiments to Measure the Neutron Lifetime, November 2012, Sante Fe, New Mexico) **14**, 121 (2013).
- Murphy, R.P., Kelley, E.G., Rogers, S.A., Sullivan, M.O., Epps, III., T.H., "Unlocking Chain Exchange in Highly Amphiphilic Block Polymer Micellar Systems: Influence of Agitation," ACS Macro Lett. **3**(11), 1106 (2014).
- Nagaraja, A.R., Stone, K.H., Toney, M.F., Peng, H., Lany, S., Mason, T.O., "Experimental Characterization of a Theoretically Designed Candidate p-Type Transparent Conducting Oxide: Li-Doped Cr_2MnO_4 ," Chem. Mater. **26**(15), 4598 (2014).
- Nakajima, Y., Hu, R., Kirshenbaum, K., Hughes, A., Syers, P., Wang, X., Wang, K., Wang, R., Saha, S.R., Pratt, D., Lynn, J.W., Paglione, J., "Topological RPdBi Half-Heusler Semimetals: A New Family of Noncentrosymmetric Magnetic Superconductors," Sci. Adv. **1**(5), 1500242 (2015).
- Nakanishi, M., Sokolov, A.P., "Protein Dynamics in a Broad Frequency Range: Dielectric Spectroscopy Studies," J. Non-Cryst. Solids **407**, 478 (2015). [CHRN]
- Nambu, Y., "Magnetic Structure Analysis by Neutron Diffraction Techniques," Hyomen Kagaku **33**(5), 302 (2012). [CHRN]
- Nanda, H., "Resolving Membrane-Bound Protein Orientation and Conformation by Neutron Reflectivity," in "Proteins in Solution and at Interfaces: Methods and Applications in Biotechnology and Materials Science, First Edition," edited by Ruso, J.M. and Piñeiro, A., (John Wiley & Sons, Inc., Hoboken, NJ) Chap. **5**, 99 (2013).
- Nanda, H., Heinrich, F., Lösche, M., "Membrane Association of the PTEN Tumor Suppressor: Neutron Scattering and MD Simulations Reveal the Structure of Protein-Membrane Complexes," Methods, in press.
- Newbloom, G.M., de la Iglesia, P., Pozzo, L.D., "Controlled Gelation of Poly(3-Alkylthiophene)s in Bulk and in Thin-Films using Low Volatility Solvent/Poor-Solvent Mixtures," Soft Matter **10**(44), 8945 (2014). [CHRN]
- Nowicka, U., Zhang, D., Walker, O., Krutauz, D., Castañeda, C.A., Chaturvedi, A., Chen, T.Y., Reis, N., Glickman, M.H., Fushman, D., "DNA-Damage-Inducible 1 Protein (Ddi1) Contains an Uncharacteristic Ubiquitin-Like Domain that Binds Ubiquitin," Structure **23**, 542 (2015).
- Omenya, F., Miller, J.K., Fang, J., Wen, B., Zhang, R., Wang, Q., Chernova, N.A., Whittingham, M.S., "Single-Phase Lithiation and Delithiation of Simferite Compounds $\text{Li}(\text{Mg}, \text{Mn}, \text{Fe})\text{PO}_4$," Chem. Mater. **26**(21), 6206 (2014).
- Page, K.A., Dura, J.A., Kim, S., Rowe, B.W., Faraone, A., "Neutron Techniques as a Probe of Structure, Dynamics, and Transport in Polyelectrolyte Membranes," in "Neutron Applications in Materials for Energy," edited by Kearley, G.J., Peterson, V.K., (Spring International Publishing, Switzerland) Chap. **10**, 273 (2015). [CHRN]
- Paglione, J., Butch, N.P., "Growth and Characterization of Topological Insulators," in "Topological Insulators: Fundamentals and Perspectives, First Edition," edited by Ortmann, F., Roche, S., Valenzuela, S.O., (Wiley-VCH Verlag GmbH & Co. KGaA, Weinham, Germany) Chap. **10**, 245 (2015).
- Pajerowski, D.M., Conklin, S.E., Leão, J., Harriger, L.W., Phelan, D., "High-Pressure Neutron Scattering of the Magnetoelastic Ni-Cr Prussian Blue Analog," Phys. Rev. B **91**(9), 094104 (2015).
- Pajerowski, D.M., Li, Q., Hyun, J., Dennis, C.L., Phelan, D., Yan, P., Chen, P., Li, G., "Chloride-Bridged, Defect-Dicubane $\{\text{Ln}_4\}$ Core Clusters: Syntheses, Crystal Structures and Magnetic Properties," Dalton T. **43**(31), 11973 (2014).
- Pan, L., Kim, S.K., Ghosh, A., Morris, C.M., Ross, K.A., Kermarrec, E., Gaulin, B.D., Koohpayeh, S.M., Tchernyshyov, O., Armitage, N.P., "Low-Energy Electrodynamics of Novel Spin Excitations in the Quantum Spin Ice $\text{Yb}_2\text{Ti}_2\text{O}_7$," Nat. Commun. **5**(4970), 1 (2014).

- Pandey, A., Kabirian, F., Hwang, J.-H., Choi, S.-H., Khan, A.S., "Mechanical Responses and Deformation Mechanisms of an AZ31 Mg Alloy Sheet under Dynamic and Simple Shear Deformations," *Int. J. Plasticity* **68**, 111 (2015).
- Pang, D., Nico, J.S., Karam, L., Timofeeva, O., Blakely, W.F., Dritschilo, A., Dizdaroglu, M., Jaruga, P., "Significant Disparity in Base and Sugar Damage in DNA Resulting from Neutron and Electron Irradiation," *J. Radiat. Res.* **55**(6), 1081 (2014).
- Parnell, S.R., Washington, A.L., Li, K., Yan, H., Stonaha, P., Li, F., Wang, T., Walsh, A., Chen, W.C., Parnell, A.J., Fairclough, J.P.A., Baxter, D.V., Snow, W.M., Pynn, R., "Spin Echo Small Angle Neutron Scattering using a Continuously Pumped ^3He Neutron Polarisation Analyser," *Rev. Sci. Instrum.* **86**(2), 023902 (2015).
- Parshall, D., Pintschovius, L., Niedziela, J.L., Castellan, J.-P., Lamago, D., Mittal, R., Wolf, Th., Reznik, D., "Close Correlation between Magnetic Properties and the Soft Phonon Mode of the Structural Transition in BaFe_2As_2 and SrFe_2As_2 ," *Phys. Rev. B* **91**(13), 134426 (2015).
- Paul, R.L., Şahin, D., Cook, J.C., Brocker, C., Lindstrom, R.M., O'Kelly, D.J., "NGD Cold-Neutron Prompt Gamma-Ray Activation Analysis Spectrometer at NIST," *J. Radioanal. Nucl. Ch.* **304**(1), 189 (2015).
- Pena-Francesch, A., Akgun, B., Miserez, A., Zhu, W., Gao, H., Demirel, M.C., "Pressure Sensitive Adhesion of an Elastomeric Protein Complex Extracted from Squid Ring Teeth," *Adv. Funct. Mater.* **24**(39), 6227 (2014).
- Peng, Y., Curtis, J.E., Fang, X., Woodson, S.A., "Structural Model of an mRNA in Complex with the Bacterial Chaperone Hfq," *P. Natl. A. Sci. USA* **111**(48), 17134 (2014).
- Perevozchikova, T., Nanda, H., Nesta, D.P., Roberts, C.J., "Protein Adsorption, Desorption, and Aggregation Mediated by Solid-Liquid Interfaces," *J. Pharm. Sci.* **104**(6), 1946 (2015). [CHRNIS]
- Pham, T.D., Hudson, M.R., Brown, C.M., Lobo, R.F., "Molecular Basis for the High CO_2 Adsorption Capacity of Chabazite Zeolites," *ChemSusChem* **7**(11), 3031 (2014).
- Phelan, D., Rodriguez, E.E., J. Gao, Bing, Y., Ye, Z.-G., Huang, Q., Wen, J., Xu, G., Stock, C., Matsuura, M., Gehring, P.M., "Phase Diagram of the Relaxor Ferroelectric $(1-x)\text{Pb}(\text{Mg}_{1/3}\text{Nb}_{2/3})\text{O}_3+x\text{PbTiO}_3$ Revisited: A Neutron Powder Diffraction Study of the Relaxor Skin Effect," *Phase Transit.* **88**(3), 283 (2015).
- Pintschovius, L., Reznik, D., Weber, F., Bourges, P., Parshall, D., Mittal, R., Chaplot, S.L., Heid, R., Wolf, T., Lamago, D., Lynn, J.W., "Spurious Peaks Arising from Multiple Scattering Events Involving the Sample Environment in Inelastic Neutron Scattering," *J. Appl. Crystallogr.* **47**(4), 1472 (2014).
- Pollock, R.A., Her, J.-H., Brown, C.M., Liu, Y., Dailly, A., "Kinetic Trapping of D_2 in MIL-53(Al) Observed using Neutron Scattering," *J. Phys. Chem. C* **118**(31), 18197 (2014).
- Pratt, D.K., Lynn, J.W., Mais, J., Chmaissem, O., Brown, D.E., Kolesnik, S., Dabrowski, B., "Neutron Scattering Studies of the Ferroelectric Distortion and Spin Dynamics in the Type-1 Multiferroic Perovskite $\text{Sr}_{0.56}\text{Ba}_{0.44}\text{MnO}_3$," *Phys. Rev. B* **90**(14), 140401 (2014).
- Preston, J.S., Pasaogullari, U., Hussey, D.S., Jacobson, D.L., "High Resolution Neutron Radiography Imaging of Microporous Layers in PEFCs," *ECS Transactions* **41**(1), 319 (2011).
- Pushin, D.A., Huber, M.G., Arif, M., Shahi, C.B., Nsofini, J., Wood, C.J., Sarenac, D., Cory, D.G., "Neutron Interferometry at the National Institute of Standards and Technology," *Adv. in High Energy Phys.* **2015**, 687480 (2015).
- Qian, K.K., Grobelny, P.J., Tyagi, M., Cicerone, M.T., "Using the Fluorescence Red Edge Effect to Assess the Long-Term Stability of Lyophilized Protein Formulations," *Mol. Pharmaceut.* **12**(4), 1141 (2015). [CHRNIS]
- Queen, W.L., Hudson, M.R., Bloch, E.D., Mason, J.A., Gonzalez, M.I., Lee, J.S., Gygi, D., Howe, J.D., Lee, K., Darwish, T.A., James, M., Peterson, V.K., Teat, S.J., Smit, B., Neaton, J.B., Long, J.R., Brown, C.M., "Comprehensive Study of Carbon Dioxide Adsorption in the Metal-Organic Frameworks M2(dobdc) ($\text{M} = \text{Mg}, \text{Mn}, \text{Fe}, \text{Co}, \text{Ni}, \text{Cu}, \text{Zn}$)," *Chem. Sci.* **5**(12), 4569 (2014).
- Quinn, G.D., Zilcha, O., Rowe, J.M., Pierce, D.J., "Failure Analysis of a 41-m Long Neutron Beam Line Guide," *J. Eur. Ceram. Soc.* **34**(14), 3263 (2014).
- Ramazanoglu, M., Laver, M., Yagmurcu, A., Choi, E.-M., Lee, S.-I., Knigavko, A., Gaulin, B.D., "Small-Angle Neutron Scattering and Magnetization Study of $\text{HoNi}_2\text{B}_2\text{C}$," *Low Temp. Phys.* **40**(2), 160 (2014). [CHRNIS]
- Rangasamy, E., Liu, Z., Gobet, M., Pilar, K., Sahu, G., Zhou, W., Wu, H., Greenbaum, S., Liang, C., "An Iodide-Based $\text{Li}_7\text{P}_2\text{S}_8\text{I}$ Superionic Conductor," *J. Am. Chem. Soc.* **137**(4), 1384 (2015).

- Rappaport, S.M., Teijido, O., Hoogerheide, D.P., Rostovtseva, T.K., Berezhevskii, A.M., Bezrukov, S.M., "Conductance Hysteresis in the Voltage-Dependent Anion Channel," *Eur. Biophys. J.*, in press.
- Robertson, A.E., Phan, D.H., Macaluso, J.E., Kuryakov, V.N., Jouravleva, E.V., Bertrand, C.E., Yudin, I.K., Anisimov, M.A., "Mesoscale Solubilization and Critical Phenomena in Binary and Quasi-Binary Solutions of Hydrotopes," *Fluid Phase Equilib.*, in press. [CHRS]
- Rogers, S.A., Calabrese, M.A., Wagner, N.J., "Rheology of Branched Wormlike Micelles," *Curr. Opin. Colloid In.* **19**(6), 530 (2014).
- Rømer, A.T., Ray, P.J., Jacobsen, H., Udby, L., Andersen, B.M., Bertelsen, M., Holm, S.L., Christensen, N.B., Toft-Petersen, R., Skoulatos, M., Laver, M., Schneidewind, A., Link, P., Oda, M., Ido, M., Momono, N., Lefmann, K., "Field-Induced Interplanar Magnetic Correlations in the High-Temperature Superconductor $\text{La}_{1.88}\text{Sr}_{0.12}\text{CuO}_4$," *Phys. Rev. B* **91**(17), 174507 (2015).
- Rostovtseva, T.K., Gurnev, P.A., Protchenko, O., Hoogerheide, D.P., Yap, T.L., Philpott, C.C., Lee, J.C., Bezrukov, S.M., " α -Synuclein Shows High-Affinity Interaction with Voltage-Dependent Anion Channel Suggesting Mechanisms of Mitochondrial Regulation and Toxicity in Parkinson Disease," *J. Biol. Chem.* **290**(30), 18467 (2015).
- Rumberger, B., Bennett, M., Zhang, J., Dura, J.A., Israeloff, N.E., "Communication: Nanoscale Ion Fluctuations in Nafion Polymer Electrolyte," *J. Chem. Phys.* **141**(7), 071102 (2014).
- Rush, J.J., "US Neutron Facility Development in the Last Half-Century: A Cautionary Tale," *Phys. Perspect.* **17**(2), 135 (2015).
- Sahoo, P., Kumar, D.K., Raghavan, S.R., Dastidar, P., "Supramolecular Synthons in Designing Low Molecular Mass Gelling Agents: L-Amino Acid Methyl Ester Cinnamate Salts and their Anti-Solvent-Induced Instant Gelation," *Chem. Asian J.* **6**(4), 1038 (2011).
- Santamaria, A.D., Becton, M.K., Cooper, N.J., Weber, A.Z., Park, J.W., "Effect of Cross-Flow on PEFC Liquid-Water Distribution: An In-Situ High-Resolution Neutron Radiography Study," *J. Power Sources*, in press.
- Sarangapani, P.S., Hudson, S.D., Jones, R.L., Douglas, J.F., Pathak, J.A., "Critical Examination of the Colloidal Particle Model of Globular Proteins," *Biophys. J.* **108**(3), 724 (2015).
- Schneeloch, J.A., Xu, Z., Wen, J., Gehring, P.M., Stock, C., Matsuda, M., Winn, B., Gu, G., Shapiro, S.M., Birgeneau, R.J., Ushiyama, T., Yanagisawa, Y., Tomioka, Y., Ito, T., Xu, G., "Neutron Inelastic Scattering Measurements of Low-Energy Phonons in the Multiferroic BiFeO_3 ," *Phys. Rev. B* **91**(6), 064301 (2015).
- Scott, D.R., Silin, V., Nanda, H., "Reconstitution of Functionalized Transmembrane Domains of Receptor Proteins into Bio-Mimetic Membranes," *Langmuir*, in press.
- Sears, J.A., Songvilay, M., Plumb, K.W., Clancy, J.P., Qiu, Y., Zhao, Y., Parshall, D., Kim, Y.-J., "Magnetic Order in $\alpha\text{-RuCl}_3$: A Honeycomb-Lattice Quantum Magnet with Strong Spin-Orbit Coupling," *Phys. Rev. B* **91**(14), 144420 (2015). [CHRS]
- Seibel, E.M., Roudebush, J.H., Ali, M.N., Ross, K.A., Cava, R.J., "Structure and Magnetic Properties of the Spin-1/2-Based Honeycomb $\text{NaNi}_2\text{BiO}_{6-\delta}$ and its Hydrate $\text{NaNi}_2\text{BiO}_{6-\delta} \cdot 1.7\text{H}_2\text{O}$," *Inorg. Chem.* **53**(20), 10989 (2014).
- Selamet, O.F., Pasaogullari, U., Spornjak, D., Hussey, D.S., Jacobson, D.L., Mat, M.D., "In-Situ Two-Phase Flow Investigation of Proton Exchange Membrane (PEM) Electrolyzer by Simultaneous Optical and Neutron Imaging," *ECS Transactions* **41**(1), 349 (2011).
- Shen, H., Valadez-Pérez, N.E., Guralnick, B., Liu, Y., Mackay, M.E., "Performance Enhancement of Polymer-Based Solar Cells by Induced Phase-Separation with Silica Particles," *J. Mater. Chem. C* **2**(47), 10087 (2014). [CHRS]
- Shen, S., Wang, G., Jin, S., Huang, Q., Ying, T., Li, D., Lai, X., Zhou, T., Zhang, H., Lin, Z., Wu, X., Chen, X., "Tunable Cobalt Vacancies and Related Properties in LaCo_xAs_2 ," *Chem. Mater.* **26**(21), 6221 (2014).
- Skoryunov, R.V., Babanova, O.A., Soloninin, A.V., Skripov, A.V., Verdal, N., Udovic, T.J., "Effects of Partial Halide Anion Substitution on Reorientational Motion in NaBH_4 : A Nuclear Magnetic Resonance Study," *J. Alloy Compd.* **636**, 293 (2015).

- Smaha, R.W., Roudebush, J.H., Herb, J.T., Seibel, E.M., Krizan, J.W., Fox, G.M., Huang, Q., Arnold, C.B., Cava, R.J., "Tuning Sodium Ion Conductivity in the Layered Honeycomb Oxide $\text{Na}_{3-x}\text{Sn}_{2-x}\text{Sb}_x\text{NaO}_6$," *Inorg. Chem.*, in press.
- Smeets, N.M.B., Bakaic, E., Yavitt, F.M., Yang, F.-C., Rheinstädter, M.C., Hoare, T., "Probing the Internal Morphology of Injectable Poly(Oligoethylene Glycol Methacrylate) Hydrogels by Light and Small-Angle Neutron Scattering," *Macromolecules* **47**(17), 6017 (2014). [CHRNA]
- Smeets, N.M.B., Patenaude, M., Kinio, D., Yavitt, F.M., Bakaic, E., Yang, F.-C., Rheinstädter, M., Hoare, T., "Injectable Hydrogels with *in situ*-forming Hydrophobic Domains: Oligo(D,L-Lactide) Modified Poly(Oligoethylene Glycol Methacrylate) Hydrogels," *Polym. Chem.* **5**(23), 6811 (2014). [CHRNA]
- Snow, W.M., Anderson, E., Barrón-Palos, L., Bass, C.D., Bass, T.D., Crawford, B.E., Crawford, C., Dawkins, J.M., Esposito, D., Fry, J., Gardiner, H., Gan, K., Haddock, C., Heckel, B.R., Holley, A.T., Horton, J.C., Huffer, C., Lieffers, J., Luo, D., Maldonado-Velázquez, M., Markoff, D.M., Micherdzinska, A.M., Mumm, H.P., Nico, J.S., Sarsour, M., Santra, S., Sharapov, E.I., Swanson, H.E., Walbridge, S.B., Zhumabekova, V., "A Slow Neutron Polarimeter for the Measurement of Parity-Odd Neutron Rotary Power," *Rev. Sci. Instrum.* **86**(5), 055101 (2015).
- Snow, W.M., Arif, M., Heacock, B., Huber, M., Li, K., Pushin, D., Skavysh, V., Young, A.R., "A Sensitive Search for Dark Energy through Chameleon Scalar Fields using Neutron Interferometry," *J. Phys. Conf. Ser.* **578**, 012009 (2015).
- Song, C., Ling, Y., Feng, Y., Zhou, W., Yildirim, T., He, Y., "A NbO-Type Metal-Organic Framework Exhibiting High Deliverable Capacity for Methane Storage," *Chem. Commun.* **51**(40), 8508 (2015).
- Stock, C., Gehring, P.M., Xu, G., Lamago, D., Reznik, D., Russina, M., Wen, J., Boatner, L.A., "Fluctuating Defects in the Incipient Relaxor $\text{K}_{1-x}\text{Li}_x\text{TaO}_3$ ($x=0.02$)," *Phys. Rev. B* **90**(22), 224302 (2014).
- Stock, C., Rodriguez, E.E., Sobolev, O., Rodriguez-Rivera, J.A., Ewings, R.A., Taylor, J.W., Christianson, A.D., Green, M.A., "Soft Striped Magnetic Fluctuations Competing with Superconductivity in Fe_{1+x}Te ," *Phys. Rev. B* **90**(12), 121113 (2014). [CHRNA]
- Stock, C., Rodriguez-Rivera, J.A., Schmalzl, K., Rodriguez, E.E., Stunault, A., Petrovic, C., "Single to Multiquasiparticle Excitations in the Itinerant Helical Magnet CeRhIn_5 ," *Phys. Rev. Lett.* **114**(24), 247005 (2015). [CHRNA]
- Stone, M.B., Chen, Y., Reich, D.H., Broholm, C., Xu, G., Copley, J.R.D., Cook, J.C., "Magnons and Continua in a Magnetized and Dimerized Spin-1/2 Chain," *Phys. Rev. B* **90**(9), 094419 (2014).
- Sunday, D.F., Ashley, E., Wan, L., Patel, K.C., Ruiz, R., Kline, R.J., "Template-Polymer Commensurability and Directed Self-Assembly Block Copolymer Lithography," *J. Polym. Sci. Pol. Phys.* **53**(8), 595 (2015).
- Svanidze, E., Wang, J.K., Besara, T., Liu, L., Huang, Q., Siegrist, T., Frandsen, B., Lynn, J.W., Nevidomskyy, A.H., Gamza, M.B., Aronson, M.C., Uemura, Y.J., Morosan, E., "An Itinerant Antiferromagnetic Metal without Magnetic Constituents," *Nat. Commun.* **6**, 7701 (2015).
- Swift, A., Sheets, J., Cole, D., Anovitz, L., Welch, S., Gu, X., Mildner, D., Chipera, S., Buchwalter, E., Cook, A., "Nano- to Microscale Pore Characterization of the Utica Shale," in "Unconventional Resources Technology Conference," edited by Society of Petroleum Engineers, (Unconventional Resources Technology Conference, August 2014, Denver, CO) 1923522 (2014). [CHRNA]
- Swift, A.M., Anovitz, L.M., Sheets, J.M., Cole, D.R., Welch, S.A., Rother, G., "Relationship between Mineralogy and Porosity in Seals Relevant to Geologic CO_2 Sequestration," *Environ. Geosci.* **21**(2), 39 (2014). [CHRNA]
- Tan, C., Leung, K.Y., Liu, D.X., Canova, M., Downing, R.G., Co, A.C., Cao, L.R., "Gamma Radiation Effects on Li-Ion Battery Electrolyte in Neutron Depth Profiling for Lithium Quantification," *J. Radioanal. Nucl. Ch.*, in press.
- Tang, W.S., Udovic, T.J., Stavila, V., "Altering the Structural Properties of $\text{A}_2\text{B}_{12}\text{H}_{12}$ Compounds via Cation and Anion Modifications," *J. Alloy Compd.*, in press.
- Tao, R., Du, E., Tang, H., Xu, X., "Neutron Scattering Studies of Crude Oil Viscosity Reduction with Electric Field," *Fuel* **134**, 493 (2014).
- Taraban, M.B., Yu, L., Feng, Y., Jouravleva, E.V., Anisimov, M.A., Jiang, Z.-X., Yu, Y.B., "Conformational Transition of a Non-Associative Fluorinated Amphiphile in Aqueous Solution," *RSC Adv.* **4**(97), 54565 (2014). [CHRNA]

- Tarasevich, B.J., Philo, J.S., Maluf, N.K., Krueger, S., Buchko, G.W., Lin, G., Shaw, W.J., "The Leucine-Rich Amelogenin Protein (LRAP) is Primarily Monomeric and Unstructured in Physiological Solution," *J. Struct. Biol.* **190**(1), 81 (2015).
- Tassel, C., Kuno, Y., Goto, Y., Yamamoto, T., Brown, C.M., Hester, J., Fujita, K., Higashi, M., Abe, R., Tanaka, K., Kobayashi, Y., Kageyama, H., "MnTaO₂N: Polar LiNbO₃-Type Oxyntiride with a Helical Spin Order," *Angew. Chem. Int. Edit.* **54**(2), 516 (2015).
- Tassel, C., Goto, Y., Kuno, Y., Hester, J., Green, M., Kobayashi, Y., Kageyama, H., "Direct Synthesis of Chromium Perovskite Oxyhydride with a High Magnetic-Transition Temperature," *Angew. Chem. Int. Edit.* **53**(39), 10377 (2014).
- Taylor, D.D., Schreiber, N.J., Brown, C.M., Arevalo-Lopez, A.M., Rodriguez, E.E., "Stabilization of Cubic Sr₂FeMoO₆ through Topochemical Reduction," *Chem. Commun.*, in press.
- Theis-Bröhl, K., Gutfreund, P., Vorobiev, A., Wolff, M., Toperverg, B.P., Dura, J.A., Borchers, J.A., "Self Assembly of Magnetic Nanoparticles at Silicon Surfaces," *Soft Matter* **11**(23), 4695 (2015).
- Trapote-Barreira, A., Porcar, L., Cama, J., Soler, J.M., Allen, A.J., "Structural Changes in C-S-H Gel during Dissolution: Small-Angle Neutron Scattering and Si-NMR Characterization," *Cement Concrete Res.* **72**, 76 (2015).
- Tsianou, M., Fajalia, A.I., "Cyclodextrins and Surfactants in Aqueous Solution above the Critical Micelle Concentration: Where are the Cyclodextrins Located?" *Langmuir* **30**(46), 13754 (2014).
- Udovic, T.J., Matsuo, M., Tang, W.S., Wu, H., Stavila, V., Soloninin, A.V., Skoryunov, R.V., Babanova, O.A., Skripov, A.V., Rush, J.J., Unemoto, A., Takamura, H., Orimo, S.-I., "Exceptional Superionic Conductivity in Disordered Sodium Decahydro-*Closo*-Decaborate," *Adv. Mater.* **26**(45), 7622 (2014). [CHRS]
- Ueland, B.G., Miclea, C.F., Gofryk, K., Qiu, Y., Ronning, F., Movshovich, R., Bauer, E.D., Gardner, J.S., Thompson, J.D., "Short-Range Magnetic Correlations in the Highly Correlated Electron Compound CeCu₄Ga," *Phys. Rev. B* **90**(12), 121109 (2014).
- Unemoto, A., Ikeshoji, T., Yasaku, S., Matsuo, M., Stavila, V., Udovic, T.J., Orimo, S.-I., "Stable Interface Formation between TiS₂ and LiBH₄ in Bulk-Type All-Solid-State Lithium Batteries," *Chem. Mater.*, in press.
- Vaish, A., Krueger, S., Dimitriou, M., Majkrzak, C., Vanderah, D.J., Chen, L., Gawrisch, K., "Enhancing the Platinum Atomic Layer Deposition Infiltration Depth inside Anodic Alumina Nanoporous Membrane," *J. Vac. Sci. Technol. A* **33**(1), 01A148 (2015).
- Vaish, A., Vanderah, D.J., Richter, L.J., Dimitriou, M., Steffens, K.L., Walker, M.L., "Dithiol-Based Modification of Poly(dopamine): Enabling Protein Resistance *via* Short-Chain Ethylene Oxide Oligomers," *Chem. Commun.* **51**(30), 6591 (2015).
- Vaish, A., Vanderah, D.J., Vierling, R., Crawshaw, F., Gallagher, D.T., Walker, M.L., "Membrane Protein Resistance of Oligo(Ethylene Oxide) Self-Assembled Monolayers," *Colloid Surface. B* **122**, 552 (2014).
- Valdivia, P.N., Kim, M.G., Forrest, T.R., Xu, Z., Wang, M., Wu, H., Harriger, L.W., Bourret-Courchesne, E.D., Birgeneau, R.J., "Copper-Substituted Iron Telluride: A Phase Diagram," *Phys. Rev. B* **91**(22), 224424 (2015).
- Van Dyk, A.K., Chatterjee, T., Ginzburg, V.V., Nakatani, A.I., "Shear-Dependent Interactions in Hydrophobically Modified Ethylene Oxide Urethane (HEUR) Based Coatings: Mesoscale Structure and Viscosity," *Macromolecules* **48**(6), 1866 (2015). [CHRS]
- Verdal, N., Udovic, T.J., Rush, J.J., Skripov, A.V., "Quasielastic Neutron Scattering Study of Tetrahydroborate Anion Dynamical Perturbations in Sodium Borohydride due to Partial Halide Anion Substitution," *J. Alloy Compd.*, in press. [CHRS]
- Verdal, N., Udovic, T.J., Stavila, V., Tang, W.S., Rush, J.J., Skripov, A.V., "Anion Reorientations in the Superionic Conducting Phase of Na₂B₁₂H₁₂," *J. Phys. Chem. C* **118**(31), 17483 (2014).
- Wagman, J.J., Parshall, D., Stone, M.B., Savici, A.T., Zhao, Y., Dabkowska, H.A., Gaulin, B.D., "Quasi-Two-Dimensional Spin and Phonon Excitations in La_{1.965}Ba_{0.035}CuO₄," *Phys. Rev. B* **91**(22), 224404 (2015).
- Wallace, D.C., Brown, C.M., McQueen, T.M., "Evolution of Magnetism in the Na_{3-δ} (Na_{1-x}Mg_x)Ir₂O₆ Series of Honeycomb Iridates," *J. Solid State Chem.* **224**, 28 (2015).

- Wang, C.H., Poudel, L., Taylor, A.E., Lawrence, J.M., Christianson, A.D., Chang, S., Rodriguez-Rivera, J.A., Lynn, J.W., Podlesnyak, A.A., Ehlers, G., Baumbach, R.E., Bauer, E.D., Gofryk, K., Ronning, F., McClellan, K.J., Thompson, J.D., "Quantum Critical Fluctuations in the Heavy Fermion Compound $\text{Ce}(\text{Ni}_{0.935}\text{Pd}_{0.065})_2\text{Ge}_2$," *J. Phys. Condens. Mat.* **27**(1), 015602 (2014). [CHRN]
- Wang, G., Persson, N., Chu, P.-H., Kleinhenz, N., Fu, B., Chang, M., Deb, N., Mao, Y., Wang, H., Grover, M.A., Reichmanis, E., "Microfluidic Crystal Engineering of π -Conjugated Polymers," *ACS Nano*, in press.
- Wang, H., Li, B., Wu, H., Hu, T.-L., Yao, Z., Zhou, W., Xiang, S., Chen, B., "A Flexible Microporous Hydrogen-Bonded Organic Frame-Work for Gas Sorption and Separation," *J. Am. Chem. Soc.*, in press.
- Wang, J., Zhong, R., Li, S., Gan, Y., Xu, Z., Zhang, C., Ozaki, T., Matsuda, M., Zhao, Y., Li, Q., Xu, G., Gu, G., Tranquada, J.M., Birgeneau, R.J., Wen, J., "Substitution of Ni for Fe in Superconducting $\text{Fe}_{0.98}\text{Te}_{0.5}\text{Se}_{0.5}$ Depresses the Normal-State Conductivity but not the Magnetic Spectral Weight," *Phys. Rev. B* **91**(1), 014501 (2015).
- Wang, M., Valdivia, P., Yi, M., Chen, J.X., Zhang, W.L., Ewings, R.A., Perring, T.G., Zhao, Y., Harriger, L.W., Lynn, J.W., Bourret-Courchesne, E., Dai, P., Lee, D.H., Yao, D.X., Birgeneau, R.J., "Spin Waves and Spatially Anisotropic Exchange Interactions in the $S = 2$ Stripe Antiferromagnet $\text{Rb}_{0.8}\text{Fe}_{1.5}\text{S}_2$," *Phys. Rev. B* **92**(4), 041109 (2015).
- Wang, Z., Ito, K., Leão, J.B., Harriger, L., Liu, Y., Chen, S.-H., "Liquid-Liquid Phase Transition and its Phase Diagram in Deeply-Cooled Heavy Water Confined in a Nanoporous Silica Matrix," *Phys. Chem. Lett.* **6**(11), 2009 (2015).
- Wen, J.-J., Tian, W., Garlea, V.O., Koohpayeh, S.M., McQueen, T.M., Li, H.-F., Yan, J.-Q., Rodriguez-Rivera, J.A., Vaknin, D., Broholm, C.L., "Disorder from Order Among Anisotropic Next-Nearest-Neighbor Ising Spin Chains in SrHo_2O_4 ," *Phys. Rev. B* **91**(5), 054424 (2015). [CHRN]
- White, C., Tan, K.T., Hunston, D., Steffens, K., Stanley, D.L., Satija, S.K., Akgun, B., Vogt, B.D., "Mechanisms of Criticality in Environmental Adhesion Loss," *Soft Matter* **11**(20), 3994 (2015).
- Wong-Ng, W., Kaduk, J.A., Luong, M., Huang, Q., "X-ray Diffraction Study and Powder Patterns of Double-Perovskites Sr_2RSbO_6 ($R=\text{Pr, Nd, Sm, Eu, Gd, Dy, Ho, Y, Er, Tm, Yb, and Lu}$)," *Powder Diff.* **29**(4), 371 (2014).
- Wong-Ng, W., Kaduk, J.A., Siderius, D.L., Allen, A.L., Espinal, L., Boyerinas, B.M., Levin, I., Suchomel, M.R., Ilavsky, J., Li, L., Williamson, I., Cockayne, E., Wu, H., "Reference Diffraction Patterns, Microstructure, and Pore-Size Distribution for the Copper (II) Benzene-1,3,5-Tricarboxylate Metal Organic Framework (Cu-BTC) Compounds," *Powder Diff.* **30**(1), 2 (2015). [CHRN]
- Wood, C.J., Abutaleb, M.O., Huber, M.G., Arif, M., Cory, D.G., Pushin, D.A., "Quantum Correlations in a Noisy Neutron Interferometer," *Phys. Rev. A* **90**(3), 032315 (2014).
- Wray, L.A., Denlinger, J., Huang, S.-W., He, H., Butch, N.P., Maple, M.B., Hussain, Z., Chuang, Y.-D., "Spectroscopic Determination of the Atomic f -Electron Symmetry Underlying Hidden Order in URu_2Si_2 ," *Phys. Rev. Lett.* **114**(23), 236401 (2015).
- Wu, H., Tang, W.S., Stavila, V., Zhou, W., Rush, J.J., Udovic, T.J., "Structural Behavior of $\text{Li}_2\text{B}_{10}\text{H}_{10}$," *J. Phys. Chem. C* **119**(12), 6481 (2015). [CHRN]
- Wu, H., Tang, W.S., Zhou, W., Stavila, V., Rush, J.J., Udovic, T.J., "The Structure of Monoclinic $\text{Na}_2\text{B}_{10}\text{H}_{10}$: A Combined Diffraction, Spectroscopy, and Theoretical Approach," *CrystEngComm* **17**(18), 3533 (2015).
- Wu, M., Liu, X., Chen, D., Huang, Q., Wu, H., Liu, Y., "Structure, Phase Transition, and Controllable Thermal Expansion Behaviors of $\text{Sc}_{2-x}\text{Fe}_x\text{Mo}_3\text{O}_{12}$," *Inorg. Chem.* **53**(17), 9206 (2014).
- Wu, Z.P., Li, P.G., Tang, W.H., Li, L.H., Huang, Q.Z., "Study of Structure and Magnetic Ordering in Multiferroics $\text{Tb}_{1-x}\text{Nd}_x\text{MnO}_3$ by Neutron Powder Diffraction," *J. Alloy Compd.*, in press.
- Wu, Z., Carlson, M., Williams, R.E., O'Kelly, S., Rowe, J.M., "A Novel Compact Core Design for Beam Tube Research Reactors," in "Transactions of the American Nuclear Society," edited by American Nuclear Society, (2015 ANS Annual Meeting, June 2015, San Antonio, TX) **112**, 795 (2015).
- Wu, Z., Williams, R.E., "A Fast and Self-Consistent Approach for Multi-Cycle Equilibrium Core Studies using Monte Carlo Models," in "ANS MC2015 Proceedings," edited by American Nuclear Society, (Joint International Conference Mathematics and Computation (M&C), Supercomputing in Nuclear Applications (SNA) and the Monte Carlo (MC) Method, April 2015, Nashville, TN), **2** (2015).

- Wu, Z., Williams, R.E., O'Kelly, S., "Preliminary Studies on A New Research Reactor and Cold Neutron Source at NIST," in "Proceedings of the 16th International Group on Research Reactors (IGORR) Conference," (16th IGORR 2014/IAEA Technical Meeting, November 2014, Bariloche, Argentina), **1** (2014).
- Xu, G., Xu, Z., Tranquada, J.M., "Absolute Cross-Section Normalization of Magnetic Neutron Scattering Data," *Rev. Sci. Instrum.* **84**(8), 083906 (2013).
- Xu, J., Hammouda, B., Cao, F., Yang, B., "Experimental Study of Phase-Changeable Water/Polyalphaolefin Nanoemulsion Fluids," in "Proceedings of the ASME: Heat Transfer and Thermal Engineering," (ASME 2014 International Mechanical Engineering Congress and Exposition, November 2014, Montreal, Quebec) **8B**, V08BT10A086 (2014).
- Xu, J., Hammouda, B., Cao, F., Yang, B., "Experimental Study of Thermophysical Properties and Nanostructure of Self-Assembled Water/Polyalphaolefin Nanoemulsion Fluids," *Adv. Mech. Eng.* **7**(4), 1 (2015). [CHRS]
- Xu, J., Li, X., Lu, F., Fu, H., Brown, C.M., Kuang, X., "Oxygen Interstitials and Vacancies in LaSrGa₃O₇-Based Melilites," *J. Solid State Chem.*, in press.
- Xu, Z., Schneeloch, J.A., Zhong, R.D., Rodriguez-Rivera, J.A., Harriger, L.W., Birgeneau, R.J., Gu, G.D., Tranquada, J.M., Xu, G., "Low-Energy Phonons and Superconductivity in Sn_{0.8}In_{0.2}Te," *Phys. Rev. B* **91**(5), 054522 (2015). [CHRS]
- Xu, Z., Stock, C., Chi, S., Kolesnikov, A.I., Xu, G., Gu, G., Tranquada, J.M., "Neutron-Scattering Evidence for a Periodically Modulated Superconducting Phase in the Underdoped Cuprate La_{1.905}Ba_{0.095}CuO₄," *Phys. Rev. Lett.* **113**(17), 177002 (2014).
- Yager, K.G., Forrey, C., Singh, G., Satija, S.K., Page, K.A., Patton, D.L., Douglas, J.F., Jones, R.L., Karim, A., "Thermally-Induced Transition of Lamellae Orientation in Block-Copolymer Films on 'Neutral' Nanoparticle-Coated Substrates," *Soft Matter* **11**(25), 5154 (2015).
- Yamani, Z., Buyers, W.J.L., Wang, F., Kim, Y.-J., Chung, J.-H., Chang, S., Gehring, P.M., Gasparovic, G., Stock, C., Broholm, C.L., Baglo, J.C., Liang, R., Bonn, D.A., Hardy, W.N., "Separation of Magnetic and Superconducting Behavior in YBa₂Cu₃O_{6.33} ($T_c = 8.4$ K)," *Phys. Rev. B* **91**(13), 134427 (2015).
- Yan, J., Sun, Y., Wu, H., Huang, Q., Wang, C., Shi, Z., Deng, S., Shi, K., Lu, H., Chu, L., "Phase Transitions and Magnetocaloric Effect in Mn₃Cu_{0.89}Ni_{0.96}," *Acta Mater.* **74**, 58 (2014).
- Yap, T.L., Jiang, Z., Heinrich, F., Gruschus, J.M., Pfefferkorn, C.M., Barros, M., Curtis, J.E., Sidransky, E., Lee, J.C., "Structural Features of Membrane-Bound Glucocerebrosidase and α -Synuclein Probed by Neutron Reflectometry and Fluorescence Spectroscopy," *J. Biol. Chem.* **290**(2), 744 (2015).
- Ye, C., Wiener, C.G., Tyagi, M., Uhrig, D., Orski, S.V., Soles, C.L., Vogt, B.D., Simmons, D.S., "Understanding the Decreased Segmental Dynamics of Supported Thin Polymer Films Reported by Incoherent Neutron Scattering," *Macromolecules* **48**(3), 801 (2015). [CHRS]
- Yehuda-Zada, Y., Orion, I., Dongwon, L., Hen, O., Beck, A., Kadmon, Y., Cohen, Y., Zigler, J., Maliszewskyj, N., Osovizky, A., "Monte Carlo Simulation for Optimizing ⁶LiF:ZnS(Ag) based Neutron Detector Configuration," in "Conference of the Nuclear Societies in Israel," (Conference of the Nuclear Societies in Israel, February 2014, Dead Sea, Israel), **268** (2014).
- Yoonessi, M., Bai, Z., Wheeler, R., Dang, T.D., "In-Situ Vapor Small Angle Neutron Scattering of Sulfonated Polyarylenethioethersulfone Random Copolymer (SPTES 70) Fuel Cells Membrane," *Mater. Res. Express* **1**(3), 035047 (2014).
- Young, N.P., Inceoglu, S., Stone, G.M., Jackson, A.J., Kline, S.R., Costeux, S., Balsara, N.P., "Thermodynamic Interactions and Phase Behavior of Multicomponent Blends Containing Supercritical Carbon Dioxide, Styrene-Acrylonitrile Random Copolymer, and Deuterated Poly(Methyl Methacrylate)," *Macromolecules* **47**(22), 8089 (2014). [CHRS]
- Yu, L.L., Wei, C., Zeisler, R., Tong, J., Ofiaz, R., Bao, H., Wang, J., "An Approach for Identification and Determination of Arsenic Species in the Extract of Kelp," *Anal. Bioanal. Chem.* **407**(12), 3517 (2015).
- Yuan, S., Kuhns, P.L., Reyes, A.P., Brooks, J.S., Hoch, M.J.R., Srivastava, V., James, R.D., El-Khatib, S., Leighton, C., "Magnetically Nanostructured State in a Ni-Mn-Sn Shape-Memory Alloy," *Phys. Rev. B* **91**(21), 214421 (2015).

- Yue, A.T., Dewey, M.S., Gilliam, D.M., Nico, J.S., Fomin, N., Greene, G.L., Snow, W.M., Wietfeldt, F.E., "A Technique for Determining Neutron Beam Fluence to 0.01% Uncertainty," in "2012 Next Generation Experiments to Measure the Neutron Lifetime Workshop," edited by Seestrom, S.J., (Generation Experiments to Measure the Neutron Lifetime, November 2012, Santa Fe, New Mexico), **103** (2014).
- Zaccai, N.R., Sandlin, C.W., Hoopes, J.T., Curtis, J.E., Fleming, P.J., Fleming, K.G., Krueger, S., "Deuterium Labeling Together with Contrast Variation Small-Angle Neutron Scattering Suggests How Skp Captures and Releases Unfolded Outer Membrane Proteins," in "Methods in Enzymology," (Elsevier Inc., Atlanta, GA), in press.
- Zhang, C., Park, J.T., Lu, X., Yu, R., Li, Y., Zhang, W., Zhao, Y., Lynn, J.W., Si, Q., Dai, P., "Neutron Spin Resonance as a Probe of Superconducting Gap Anisotropy in Partially Detwinned Electron Underdoped $\text{NaFe}_{0.985}\text{Co}_{0.015}\text{As}$," *Phys. Rev. B* **91**(10), 104520 (2015).
- Zhang, Q., Fernandes, R.M., Lamsal, J., Yan, J., Chi, S., Tucker, G.S., Pratt, D.K., Lynn, J.W., McCallum, R.W., Canfield, P.C., Lograsso, T.A., Goldman, A.I., Vaknin, D., McQueeney, R.J., "Neutron-Scattering Measurements of Spin Excitations in LaFeAsO and $\text{Ba}(\text{Fe}_{0.953}\text{Co}_{0.047})_2\text{As}_2$: Evidence for a Sharp Enhancement of Spin Fluctuations by Nematic Order," *Phys. Rev. Lett.* **114**(5), 057001 (2015).
- Zhang, X., Douglas, J.F., Satija, S., Karim, A., "Enhanced Vertical Ordering of Block Copolymer Films by Tuning Molecular Mass," *RSC Adv.* **5**(41), 32307 (2015).
- Zhang, Z.-J., Jin, T.-T., Xu, M.-M., Huang, Q.-Z., Li, M.-R., Zhao, J.-T., "Low-Temperature Vaterite-Type LuBO_3 , a Vacancy-Stabilized Phase Synthesized at High Temperature," *Inorg. Chem.* **54**(3), 969 (2015).
- Zhao, Y.-Y., Hu, F.-X., Bao, L.-F., Wang, J., Wu, H., Huang, Q.-Z., Wu, R.-R., Liu, Y., Shen, F.-R., Kuang, H., Zhang, M., Zuo, W.-L., Zheng, X.-Q., Sun, J.-R., Shen, B.-G., "Giant Negative Thermal Expansion in Bonded MnCoGe -Based Compounds with Ni_2In -Type Hexagonal Structure," *J. Am. Chem. Soc.* **137**(5), 1746 (2015).
- Zhernenkov, M., Ashkar, R., Feng, H., Akintewe, O.O., Gallant, N.D., Toomey, R., Ankner, J.F., Pynn, R., "Thermoresponsive PNIPAM Coatings on Nanostructured Gratings for Cell Alignment and Release," *ACS Appl. Mater. Interfaces* **7**(22), 11857 (2015).
- Zhou, C., Toombes, G.E.S., Wasbrough, M.J., Hillmyer, M.A., Lodge, T.P., "Structure of Two-Compartment Hydrogels from Thermoresponsive ABC Triblock Terpolymers," *Macromolecules*, in press.
- Zhou, Y., Zhang, L.-L., Li, H., "Spectral Analysis of Water Dynamics in Cement Paste by Quasi-Elastic Neutron Scattering," *Acta Phys. Sin.-Ch Ed.* **64**(5), 056101 (2015). [CHNRNS]
- Zhou, Z., Hollingsworth, J.V., Hong, S., Wei, G., Shi, Y., Lu, X., Cheng, H., Han, C.C., "Effects of Particle Softness on Shear Thickening of Microgel Suspensions," *Soft Matter* **10**(33), 6286 (2014). [CHNRNS]

Instruments and Contacts *(name, tel. 301-975-xxxx, email)*

High resolution powder diffractometer (BT-1):

- J. K. Stalick, 6223, judith.stalick@nist.gov
- H. Wu, 2387, hui.wu@nist.gov
- Q. Z. Huang, 6164, qing.huang@nist.gov
- C. M. Brown, 5134, craig.brown@nist.gov

Residual stress diffractometer (BT-8):

- T. Gnäuepel-Herold, 5380, thomas.gnaeupel-herold@nist.gov

30-m SANS instrument (NG-7):

- Y. Liu, 6235, yun.liu@nist.gov
- Y. Mao, 5250, yimin.mao@nist.gov
- J. R. Krzywon, 6650, jkrzywon@nist.gov

30-m SANS instrument (NG-B 30m) (CHRS):

- B. Hammouda, 3961, hammouda@nist.gov
- P. D. Butler, 2028, paul.butler@nist.gov
- S. Krueger, 6734, susan.krueger@nist.gov
- C. Gagnon, 2020, cedric.gagnon@nist.gov

10-m SANS instrument (NG-B) (nSoft):

- R. Jones, 4624, ronald.jones@nist.gov
- K. Weigandt, 8396, kathleen.weigandt@nist.gov

USANS, Perfect Crystal SANS (BT-5) (CHRS):

- M. Bleuel, 5165, markus.bleuel@nist.gov
- P. D. Butler, 2028, paul.butler@nist.gov

Polarized Beam Reflectometer/Diffractometer (NG-D):

- B. J. Kirby, 8395, brian.kirby@nist.gov
- J. A. Borchers, 6597, julie.borchers@nist.gov
- C. F. Majkrzak, 5251, cmajkrzak@nist.gov

MAGIK, Off-Specular Reflectometer (NG-D):

- B. B. Maranville, 6034, brian.maranville@nist.gov
- J. A. Dura, 6251, joseph.dura@nist.gov

Neutron reflectometer-horizontal sample (NG-7):

- S. K. Satija, 5250, satija@nist.gov

Double-focusing triple-axis Spectrometer (BT-7):

- Y. Zhao, 2164, yang.zhao@nist.gov
- D. Parshall, 8097, daniel.parshall@nist.gov
- J. W. Lynn, 6246, jeff.lynn@nist.gov

SPINS, Spin-polarized triple-axis spectrometer (NG-5):

- L. Harriger, 8360, leland.harriger@nist.gov

Triple-axis spectrometer (BT-4):

- W. Ratcliff, 4316, william.ratcliff@nist.gov

FANS, Filter-analyzer neutron spectrometer (BT-4):

- T. J. Udovic, 6241, udovic@nist.gov

DCS, Disk-chopper time-of-flight spectrometer (NG-4):

- J. R. D. Copley, 5133, jcopley@nist.gov
- N. Butch, 4863, nicholas.butch@nist.gov

HFBS, High-flux backscattering spectrometer (NG-2) (CHRS):

- M. Tyagi, 2046, madhusudan.tyagi@nist.gov
- W. Zhou, 8169, wei.zhou@nist.gov

NSE, Neutron spin echo spectrometer (NG-A) (CHRS):

- A. Faraone, 5254, antonio.faraone@nist.gov
- M. Nagao, 5505, michihiro.nagao@nist.gov

MACS, Multi-angle crystal spectrometer (BT-9) (CHRS):

- J. A. Rodriguez-Rivera, 6019, jose.rodriguez@nist.gov
- Y. Qiu, 3274, yiming.qiu@nist.gov

Cold-neutron prompt-gamma neutron activation analysis (NG-D):

- R. L. Paul, 6287, rpaul@nist.gov

Thermal-neutron prompt-gamma activation analysis (VT-5):

- R. G. Downing, 3782, gregory.downing@nist.gov

Other activation analysis facilities:

- P. Chu, 2988, pamela.chu@nist.gov

Cold neutron depth profiling (NG-1):

- R. G. Downing, 3782, gregory.downing@nist.gov

Thermal Neutron Imaging Station (BT-2):

- D. Jacobson, 6207, david.jacobson@nist.gov
- D. Hussey, 6465, daniel.hussey@nist.gov
- E. Baltic, 4842, eli.baltic@nist.gov
- M. Arif, 6303, muhammad.arif@nist.gov

Cold Neutron Imaging Station (NG-6):

- D. Jacobson, 6207, david.jacobson@nist.gov
- D. Hussey, 6465, daniel.hussey@nist.gov
- E. Baltic, 4842, eli.baltic@nist.gov
- M. Arif, 6303, muhammad.arif@nist.gov

Neutron interferometer (NG-7):

- M. Arif, 6303, muhammad.arif@nist.gov
- D. Jacobson, 6207, david.jacobson@nist.gov
- D. Hussey, 6465, daniel.hussey@nist.gov

Fundamental neutron physics station (NG-C):

- J. Nico, 4663, nico@nist.gov

Fundamental neutron physics station (NG-6):

- NG-6M: M. S. Dewey, 4843, mdewey@nist.gov
- MDM: M. Huber, 5641, michael.huber@nist.gov

Neutron test station (NG-7):

- R. Erwin, 6245, ross.erwin@nist.gov
- K. Krycka, 8685, kathryn.krycka@nist.gov

Theory and modeling:

- J. E. Curtis, 3959, joseph.curtis@nist.gov
- T. Yildirim, 6228, taner@nist.gov

Instruments under development:

vSANS instrument:

- J. G. Barker, 6732, john.barker@nist.gov
- C. J. Glinka, 6242, charles.glinka@nist.gov

CANDOR, White-beam reflectometer/diffractometer:

- F. Heinrich, 4507, frank.heinrich@nist.gov
- C. F. Majkrzak, 5251, charles.majkrzak@nist.gov

Copies of annual reports, facility information, user information, and research proposal guidelines are available electronically.

Please visit our website: <http://www.ncnr.nist.gov>

For a paper copy of this report:

Steve Kline
301-975-6243
steven.kline@nist.gov

For general information on the facility:

Rob Dimeo
301-975-6210
robert.dimeo@nist.gov

Dan Neumann
301-975-5252
dan.neumann@nist.gov

For information on visiting the facility and/or user access questions:

Julie Keyser
301-975-8200
julie.keyser@nist.gov

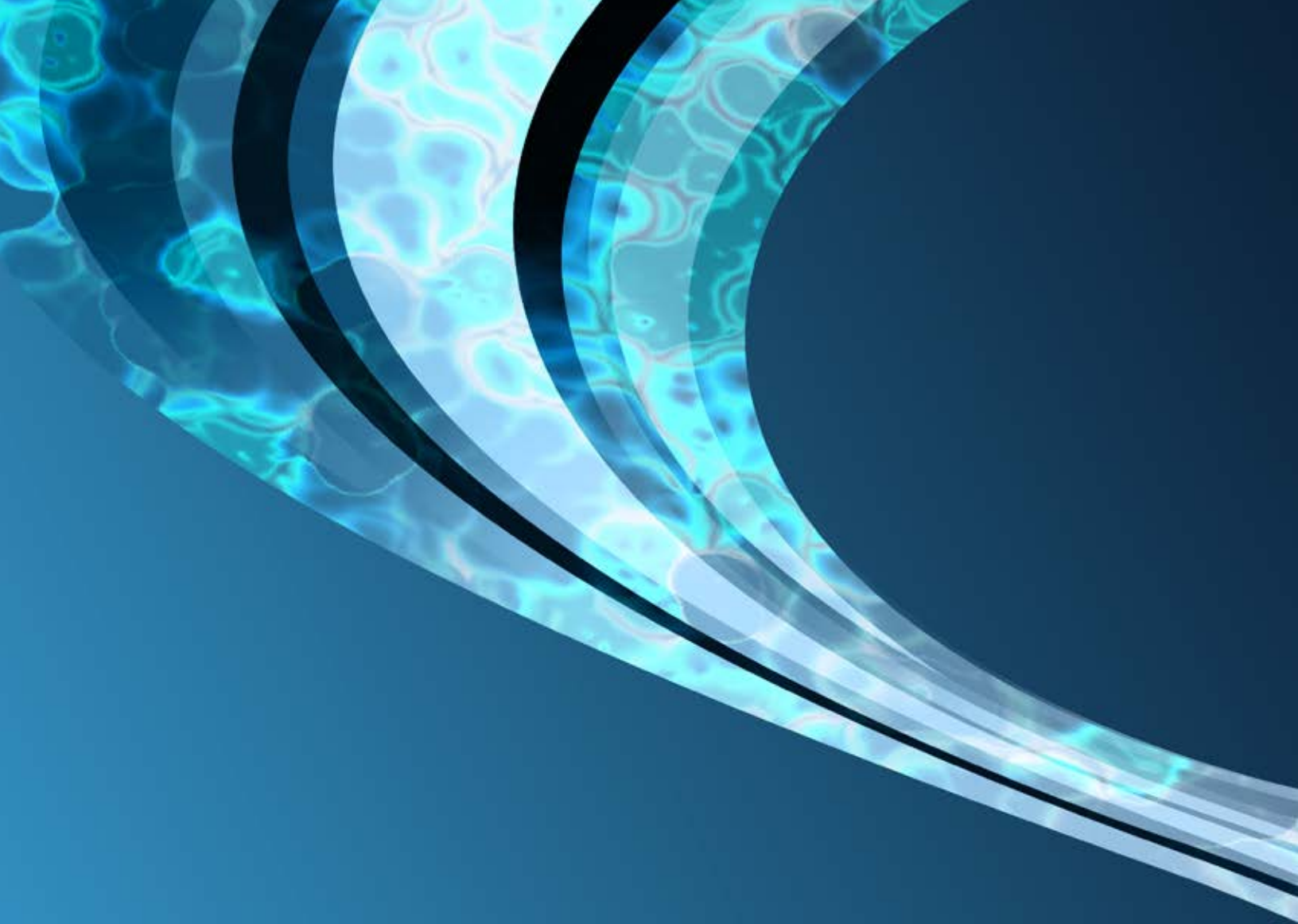
Mary Ann FitzGerald
301-975-8200
maryann.fitzgerald@nist.gov

For information on performing research at the facility:

Yamali Hernandez
301-975-5295
yamali.hernandez@nist.gov

Facility address:

NIST Center for Neutron Research
National Institute of Standards and Technology
100 Bureau Drive, Mail Stop 6100
Gaithersburg, MD 20899-6100 USA



NIST CENTER FOR NEUTRON RESEARCH
National Institute of Standards and Technology
100 Bureau Drive, MS 6100
Gaithersburg, MD 20899-6100

www.ncnr.nist.gov